ARSENIC TRISULFIDE ON LITHIUM NIOBATE WAVEGUIDES FOR NONLINEAR INFRARED OPTICS

A Dissertation

by

QI CHEN

Submitted to the Office of Graduate and Professional Studies of
Texas A&M University
in partial fulfillment of the requirements for the degree of

DOCTOR OF PHILOSOPHY

Chair of Committee,	Christi K. Madsen
Committee Members,	Ohannes Eknoyan
	Jim Xiuquan Ji
	Alexey Belyanin
Head of Department,	Chanan Singh

August 2014

Major Subject: Electrical Engineering

ABSTRACT

Arsenic trisulfide (As_2S_3) waveguides on lithium niobate ($LiNbO_3$) substrate have a wide variety of applications in both near-infrared (near-IR) and mid-infrared (mid-IR). As an amorphous material, As_2S_3 has large transmission range (0.2-11μm) and high nonlinear refractive index ($n_2=3\times10^{-18}$ m^2/W), which can be utilized to nonlinear infrared optics. Meanwhile, as a birefringence material, $LiNbO_3$ is an attractive substrate to integrate with As_2S_3 waveguides by semiconductor fabrication techniques, due to its lower refractive index and large transmission range (0.42-5.2 μm).

Since low loss As_2S_3-on-$LiNbO_3$ waveguides have been developed, it is a good time to exploit its applications in mid-IR wavelength. We illustrate the application of As_2S_3-on-$LiNbO_3$ waveguides in four-wave-mixing (FWM), which can generate 3.03 μm mid-IR light by a 1.55 μm near-IR signal source and a strong 2.05 μm pump source. When pump power intensity is 0.1 GW/cm^2, the largest parametric conversion efficiency at 3.03 μm is -8 dB. On the other hand, since mid-IR detectors are limited in terms of noise performance, we also provide an excellent solution with our As_2S_3-on-$LiNbO_3$ waveguides, which largely improve the electrical signal-to-noise ratio (eSNR) by converting mid-IR signals to near-IR wavelengths. Therefore, state-of-the-art near-IR commercial detectors can be used to detector mid-IR signals indirectly.

In order to characterize our different types of optical devices in near-IR and mid-IR, we build a measurement system using optical low-coherence interferometry (OLCI) and Fourier transform spectroscopy techniques. The group delay of the device-under-test (DUT) can be achieved.

DEDICATION

To my family

ACKNOWLEDGEMENTS

I would like to express the deepest appreciation to my committee chair and advisor, Dr. Christi. K. Madsen, for the continuous support of my Ph.D study and research with patience, enthusiasm and immense knowledge. I would never have been able to finish my dissertation without her expert guidance. I would also like to thank my other committee members, Dr. Ohannes Eknoyan, Dr. Jim Xiuquan Ji, and Dr. Alexey Belyanin, for their time and efforts in guiding me throughout the courses of this research.

I am grateful for colleagues and friends for their help and discussion. They are Mehmet Solmaz, Donnie Adams, Xin Xia, Weechong Tan, Xiaomin Song, William Snider, Jacob Webb, Yifeng Zhou, Jae Hyun Kim, Xin Wang, Ran Huang and Dwayne Macik, Yuxiao Liu and Chen Zhang. Moreover, I appreciate the incredible support from the ISSE staff, Robert Atkins, Jim Gardner, Travis James and Dennie Spears.

I would like to thank my friends in MIRTHE as well. Thanks to Elaine Lalanne, Hong Cai, Victor Torres and Dr. Anthony M. Johnson from UMBC for their support and discussion on experiments of four-wave mixing.

Finally, special thanks to my mother Lili Guo, my father Jingliang Chen and my wife Sha Yu for their love and encouragement.

TABLE OF CONTENTS

Page

LIST OF FIGURES

Page

LIST OF TABLES

Page

CHAPTER I

INTRODUCTION

1.1 Semiconductor industry

The semiconductor industry was born in the 1970s for two main business drivers. The first consisted in providing more cost effective memory devices to computer industry. The second consisted in production of application specific integrated circuits (ASICs) to companies that required specific functionalities to realize novel products [1]. As shown in Figure 1.1, semiconductor industry is guided by Moore's law, which is the number of transistors on integrated circuits doubles approximately every two years.

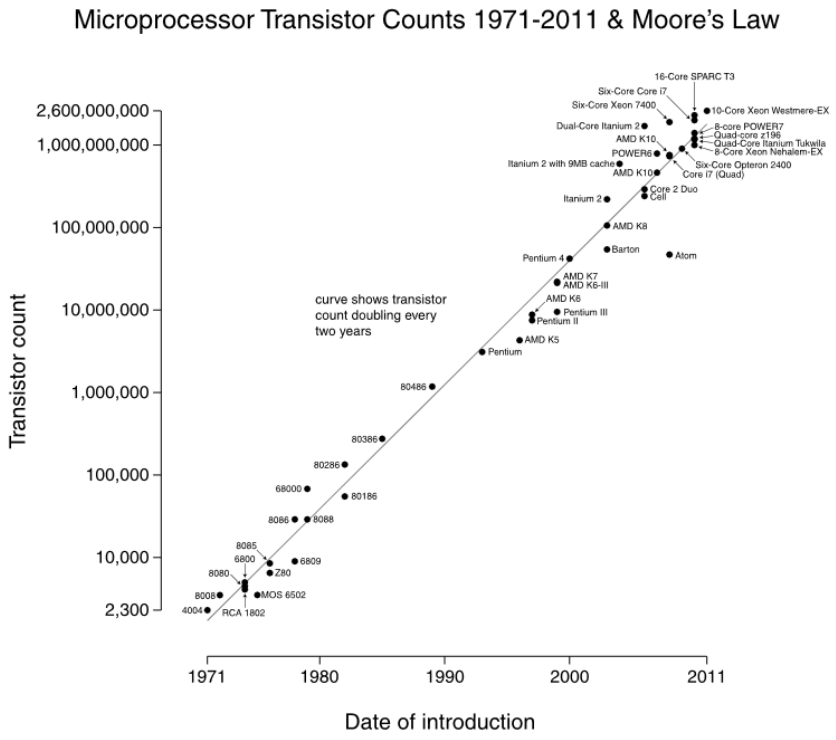

Figure 1.1 CPU transistor counts vs. dates of introduction

In the past decade, a new ecosystem of semiconductor industry has emerged. In the first place, the fast development of manufacturing techniques largely reduced minimum feature sizes and allowed integrated circuits (ICs), comprised of thousands of millions of transistors, to be produced cost effectively, which made it achievable to integrate extremely large numbers of components on a single chip at affordable costs. This type of devices is defined as system on chip (SOC). In the second place, since ICs manufacturers can offer foundry services at attractive prices, division emerged in semiconductor industry. Some fabless companies (e.g. Qualcomm and Broadcom), which only produced the designs and testing but do not manufacture ICs themselves showed up. At the same time, some companies (e.g. TSMC and UMC) without doing designs only offered foundry services for fabless companies. In the third place, with the high speed development of sophisticated equipment and advanced techniques, semiconductor industry not only focused on ASICs, companies but also went through adjacent fields. For instance, more and more companies expanded to micro-electro-mechanical systems (MEMS) market due to its huge potential in mobile market. Figure 1.2 illustrates the market forecast value for MEMS chips from 2012 to 2018 [2]. Last but not least, the rapid rise of Internet and mobile market, including smartphones and tablets, resulted in the extensive demand of global communication network, especially for optical fiber cables, which was rejuvenating from the broken fiber-optic bubble.

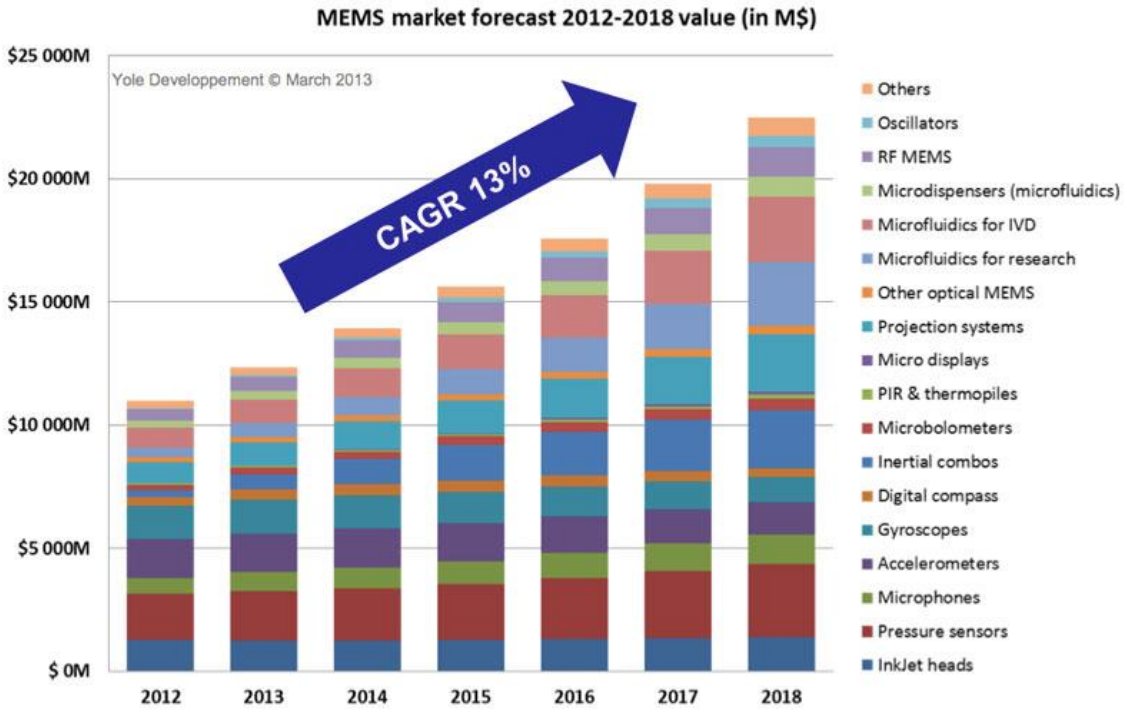

Figure 1.2 MEMS market forecast value

Recently, with the fast growing on mobile market, it is more and more demanding on semiconductor devices. First of all, obviously, it is required that all the components should be small enough to be integrated into a smartphone, which is very challenging to semiconductor manufacturer. Compared to laptops or desktops, not only do smartphones have microprocessor, memory, power management IC, audio and video modules, but they also have communication system, cameras, gyroscope, accelerometer and compass. And it is very challenging to IC packaging, which provides interconnection and protection for different chips, as shown in Figure 1.3 [3].

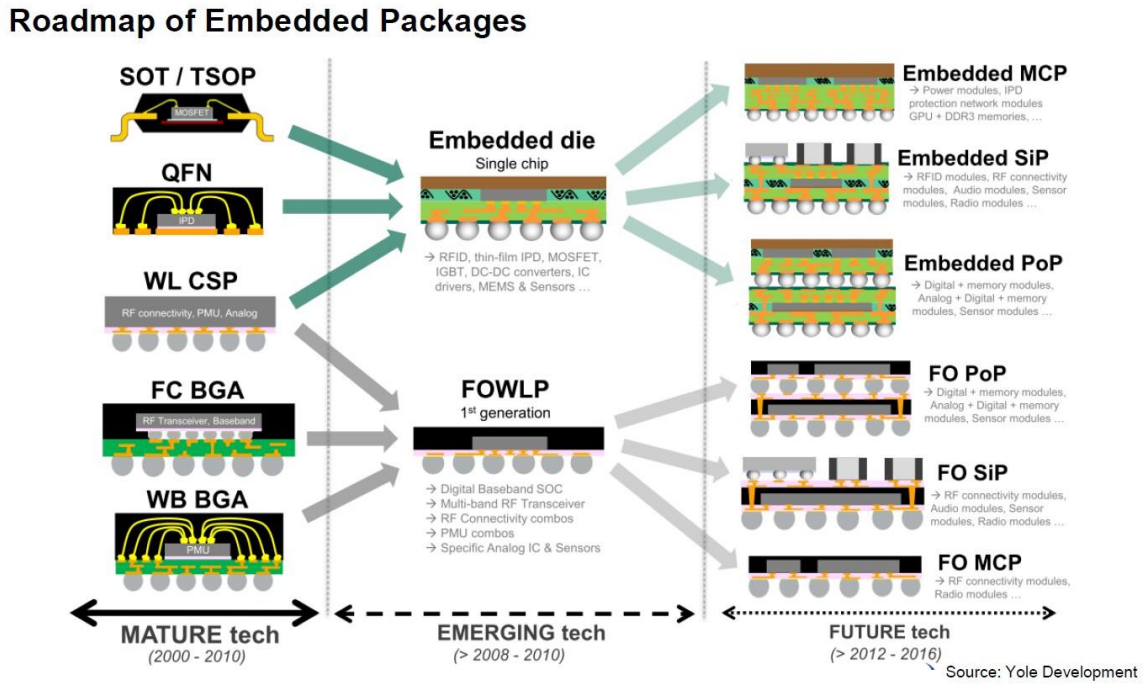

Figure 1.3 Roadmap of embedded packages for smartphones

In addition, the power consumption is supposed to be limited. It is not a big problem for computer manufacturers. However, customers won't buy smartphone that need to be charged every two hours. It is sophisticated to make a balance between device performance and power consumption, which, I think, is the biggest challenge to smartphone manufacturers. Finally, since mobile market is highly competitive, cost control is very important. In details, companies need to optimize their throughput and yield.

International Technology Roadmap for Semiconductors (ITRS), a collaborative effort that assesses the technical challenges and opportunities for the semiconductor industry through 2028 [2], plays a significant role in assessing and improving the future of semiconductor techniques by identifying the future technical obstacles. Therefore, the

industry can collaborate effectively to solve them. Using the ITRS as a guide, our industry will continue to develop next-generation semiconductor techniques that lead to smaller, faster, and more efficient and less costly end-use devices. These technology advances will have profound impacts on people across the globe [2].

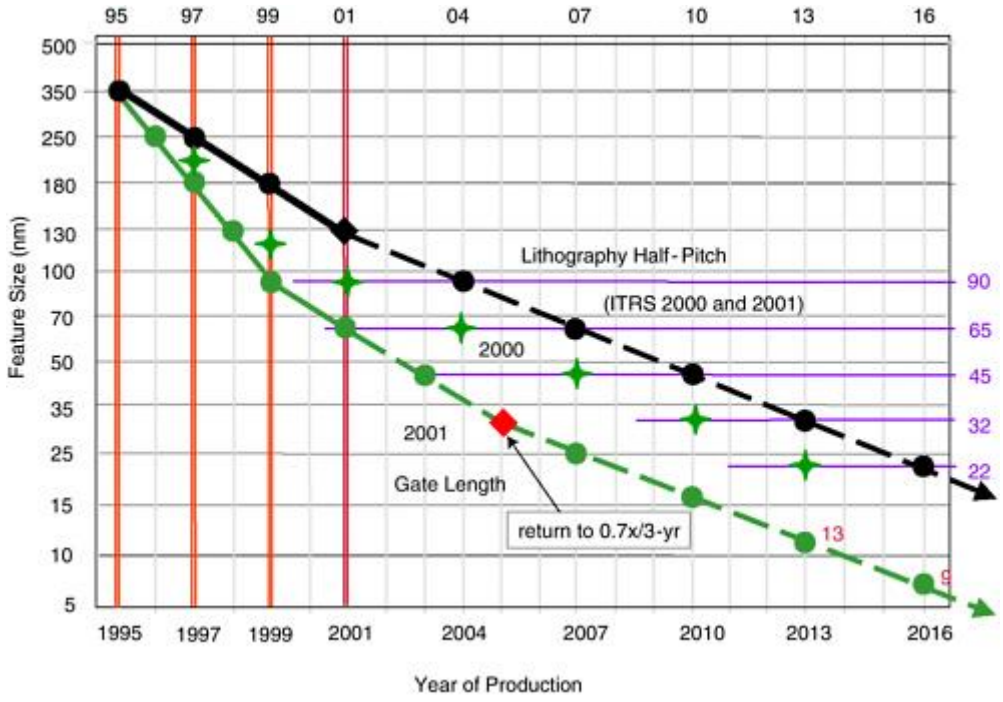

Figure 1.4 Integrated circuit growths

1.2 Mid-IR applications

Mid-IR refers to the wavelengths ranging from 3 μm to 30 μm, which is longer than those of visible light (390 nm to 750 nm) but shorter than those of microwave (1 mm to 1 m). It has plenty of applications: New types of lasers for military use, wide-spread sensing applications, monitoring to hazardous chemical gases and new medical

diagnostics. Among all of them, one of the most significant applications for mid-IR is trace gas detection.

Trace gas detection technique is based upon the transmission spectroscopy. In mid-IR region, the vast majority of gaseous chemical substances exhibit fundamental vibrational absorption bands, and the absorption of light provides a nearly universal means for their detection [4]. The high sensitivity and capability of non-intrusive in-situ detection make it ideal for trace gas detection. As demonstrated in Figure 1.5, light emitted from a broadband mid-IR source passes through the gas under test, and then is incident onto a spectrometer. Due to the absorption by gas molecules at certain wavelengths, the concentration of the gas under test will be obtained based on the comparison between the gas transmission spectrum and reference spectrum.

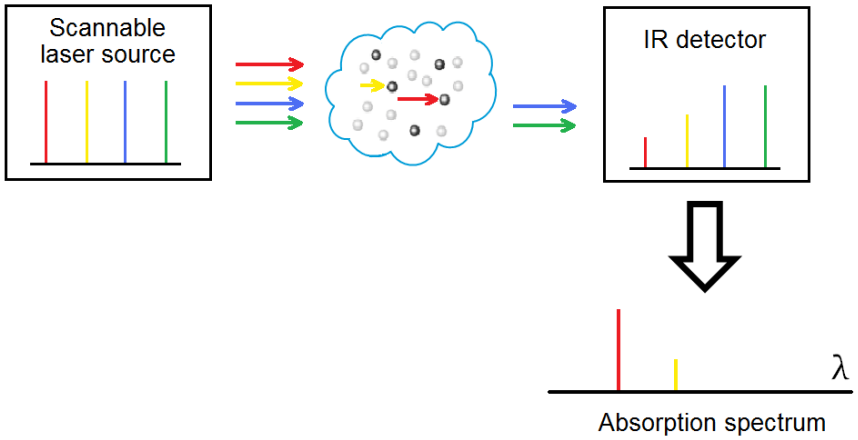

Figure 1.5 Configuration of transmission spectroscopy

There are three major advantages to trace gas detection technique compared to other spectroscopy approaches. In the first place, it is able to provide the unique information of gas molecules directly. In details, every gas molecule has its own

particular “fingerprint”, which is shown in its absorption spectrum, because the mid-IR light is absorbed by the fundamental vibrational bands that the gas molecules are consisted of. The simulated absorption spectra of some common trace gases are shown Figure 1.6 [5], the wavelength range is from 3.1 μm to 5.5 μm. In the second place, trace gas detection technique has very high sensitivity. The strength of the absorption peak is so large that it makes particle-per-billion and even single-molecule-detection possible [5]. Last but not least, it is neither destructive nor invasive, which is important to medicine particularly. Once the technique is realized, it will have a huge number of applications in non-intrusive medical diagnostics, monitoring atmosphere, industrial process control and even for military use.

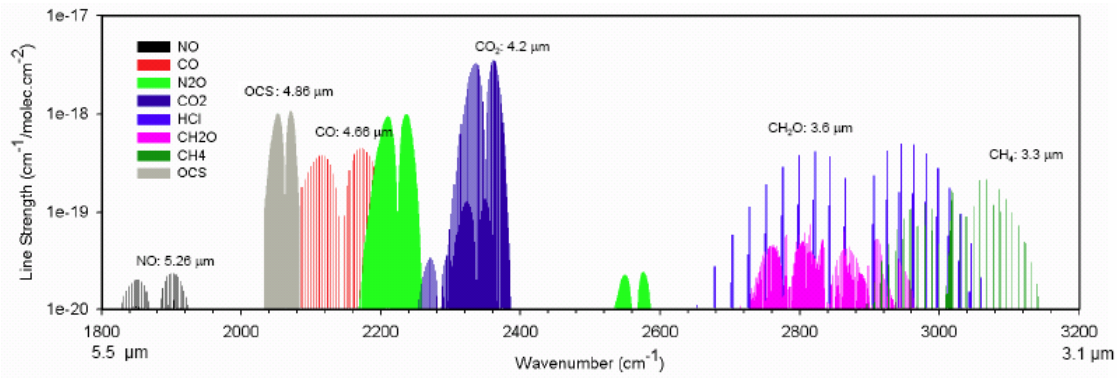

Figure 1.6 Absorption spectra of trace gases

Since the idea of trace gas detection has been well-demonstrated by simulation, the next step is to achieve it experimentally. Basically, the system consists of optical components such as mid-IR light sources, beam splitters, focus lenses, wave plates and detectors, as shown in Figure 1.7 [5]. Also, a mini system can be built on a vehicle as a mobile sensor, which is illustrated in Figure 1.8 [5].

In order to use it for different environment appropriately, it is necessary to make it compact and stable. Our solution is integrated optical circuits, which are a thin-film-type optical circuit designed to have a certain function by integrating a laser diode as the source, functional components, such as switches or modulators, and interconnection waveguides and photodiodes as detectors, on a single substrate [6]. Through integration, a more compact, stable and functional optical system can be expected [6]. The advanced integrated circuit (IC) fabrication technology from semiconductor industry can provide powerful support to the integration. Therefore, the high volume manufacturing of integrated optical circuits with stable functions, small size and low cost can be expected. But first of all, we need to integrated mid-IR light sources with optical waveguides for interconnection of trace gas detection system with low loss. Our As_2S_3-on-$LiNbO_3$ waveguide is an ideal candidate for it with its large transmission range, low propagation loss and high refractive index. It is also suitable to standard semiconductor manufacturing techniques, which provides a good method to fabricate it.

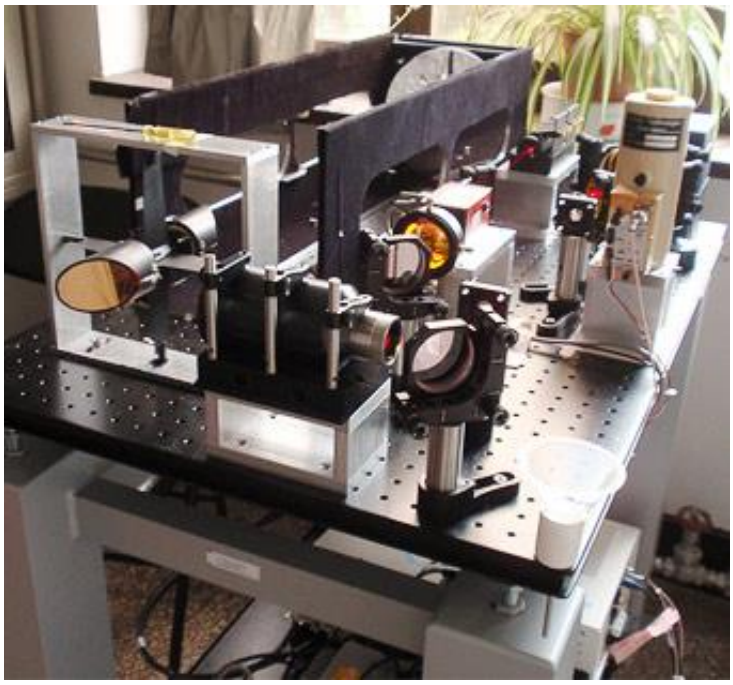

Figure 1.7 Trace gas detection system

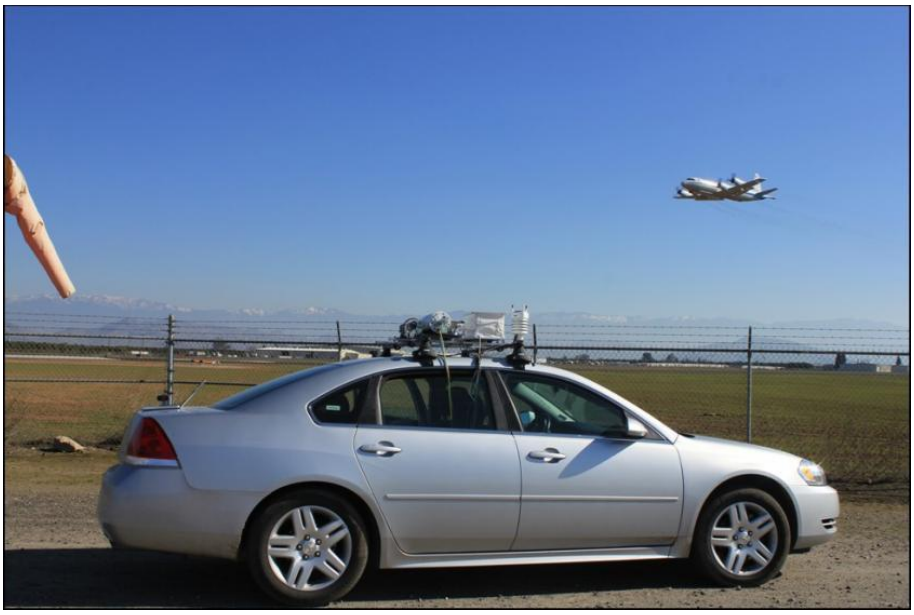

Figure 1.8 Mobile Sensor Systems

1.3 As_2S_3 waveguides on $LiNbO_3$ substrate

Chalcogenide glasses have been investigated as a good platform for telecommunication utilization. They are a set of amorphous materials consisted of chalcogen elements (sulphur, selenium and tellurium) covalently bonded with one or two structural elements such as Ge, As, Sb, Ga, etc [7]. Among several of them, As_2S_3, which has a very wide transmission range (0.2 μm to 11 μm), is a good candidate for mid-IR applications.

$LiNbO_3$, a widely-used optical material, exhibits excellent electro-optic, nonlinear and piezoelectric properties, and has broad transmission over the wavelength range from 0.42 μm to 5.2 μm, which is a big advantage compared to silicon dioxide (SiO_2), a popular substrate material for near-IR use. The SiO_2 transmittance spectrum is shown Figure 1.9 [8], where the strong absorption peak starts around 2.5 μm. Therefore, $LiNbO_3$ is more applicable than SiO_2 for mid-IR applications.

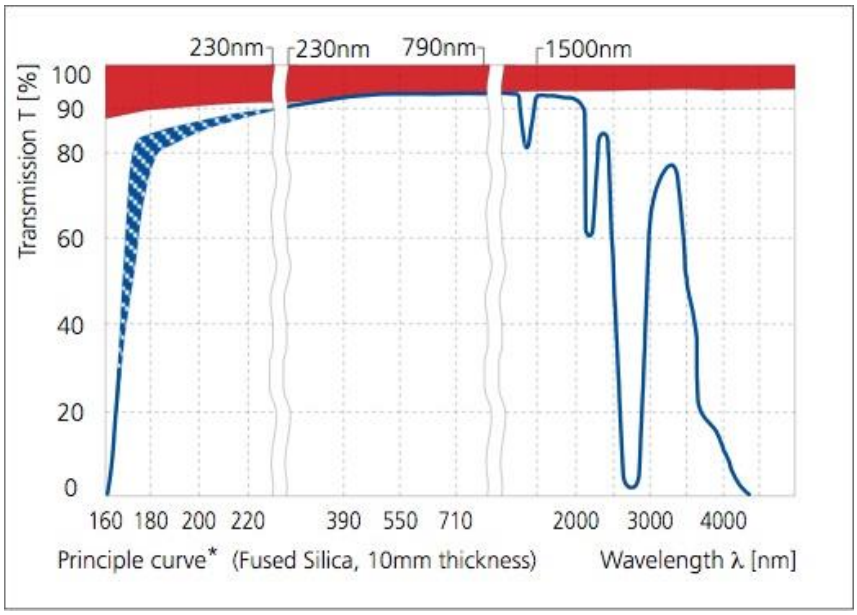

Figure 1.9 SiO_2 transmission spectrum

In addition, As_2S_3 has high refractive index and low processing temperatures, which allow very compact optical interconnects to be fabricated on different substrate materials [9]. For our purpose, its large refractive index and high nonlinearity make it ideal for all optical signal processing [10]. However, as a coin has two sides, As_2S_3 has its disadvantages. It is a very fragile material, which requires careful protection and storing during fabrication and testing processes. It is also an active material which will react with oxygen when exposed in the air at room temperature. Moreover, As_2S_3 is a photosensitive material. Its refractive index can be changed as exposure to above-band-gap wavelength light, which results in the instability of the optical properties of the material. But this issue can be solved by annealing it after fabrication [11].

CHAPTER II

THEORETICAL REVIEW

2.1 Electromagnetic theory and Maxwell's equations

Classical electromagnetism (classical electrodynamics) describes the interactions between electric charges by classical Newtonian model. The theory provides an excellent description of electromagnetic phenomena whenever the relevant length scales and field strengths are large enough that quantum mechanical effects are negligible [12]. The relationship between electric and magnetic fields, including excitation, propagation and interaction are given by Maxwell's equations, which were published by James Clerk Maxwell, a Scottish physicist and mathematician, in "On Physical Lines of Force" between 1861 and 1862 [13]. Assuming an isotropic, source-free and lossless dielectric material, Maxwell's equations written in differential form are shown in equations (2.1) to (2.4)

$$\nabla \times E = -\mu \frac{\partial H}{\partial t} \tag{2.1}$$

$$\nabla \times H = \varepsilon \frac{\partial E}{\partial t} + J \tag{2.2}$$

$$\nabla \cdot D = \rho \tag{2.3}$$

$$\nabla \cdot B = 0 \tag{2.4}$$

where E is the electric field. H is the magnetic field. J is the electric current density and ρ is the free charge density. J=0 and ρ=0 represents that the material is free of sources. μ and ε are permeability and permittivity of the material, which are also called the magnetic and electric constant respectively.

$$\mu = \mu_0 \tag{2.5}$$

$$\varepsilon = \varepsilon_r \varepsilon_0 = \varepsilon_0 n^2 \tag{2.6}$$

where $\mu_{0=}4\pi\times10^{-7}$ H/m and $\varepsilon_{0=}8.854\times10^{-12}$ F/m are their respective values in vacuum. n is the refractive index.

Two new auxiliary variables are introduced to denote the interactions of magnetic and electric fields in the material: The electric displacement field D and the magnetizing field H, which are related to the electric field E and magnetic field B respectively. As shown in equations (2.7) and (2.8),

$$D = \varepsilon_0 E + P \tag{2.7}$$

$$B = \mu_0 H + M \tag{2.8}$$

where P is the polarization and M is the magnetization. In order to define the wave phenomena, a relationship between electric and magnetic fields can be derived from equations (2.1) and (2.2)

$$\begin{aligned} &\nabla \times (\nabla \times E) \\ &= -\mu_0 \frac{\partial}{\partial t}(\nabla \times H) \\ &= -\mu_0 \varepsilon_0 n^2 \frac{\partial^2 E}{\partial t^2} \end{aligned} \tag{2.9}$$

using vector identity $\nabla \times (\nabla \times E) = \nabla(\nabla \bullet E) - \nabla^2 E$, Ohm's law $J = \varepsilon E$, $c = 1/\sqrt{\mu_0 \varepsilon_0}$ and equation (2.3), equation (2.9) becomes

$$\nabla^2 E = \frac{n^2}{c^2} \frac{\partial^2 E}{\partial t^2} \tag{2.10}$$

Similarly, we can arrive equation (2.2) can be described by taking the curl

$$\nabla^2 H = \frac{n^2}{c^2}\frac{\partial^2 H}{\partial t^2} \tag{2.11}$$

Equations (2.10) and (2.11) are also called Helmholtz equations. The solution can be described by standard wave equation

$$E = E_0 e^{j[\omega t - k \bullet r + \varphi_0]} \tag{2.12}$$

where E_0 is the amplitude. ω is the angular frequency. $k=2\pi n/\lambda$ is the wave vector. r is the position vector. φ_0 is the initial phase.

2.2 Optical waveguides

Optical waveguides are physical structures that guide electromagnetic waves by refractive index difference. In other words, electromagnetic waves are confined in optical waveguides based upon the principle of total internal reflection. According to the waveguide geometry, optical waveguides can be classified as four types: slab waveguides, rectangular waveguides, rib waveguides or diffused waveguides. Based upon refractive index distribution, optical waveguides can be categorized into step-index waveguides or graded-index waveguides.

2.2.1 Step-index slab waveguides

As shown in Figure 2.1, step-index slab waveguide (planar waveguide) is the simplest optical waveguide model, which consists of three layers of materials with different refractive indices n_1, n_2 and n_3. If n_2 is larger than n_1 and n_3, electromagnetic waves can be confined in the middle layer by total internal reflection.

Transverse electric (TE) mode represents that the direction of electric field is transverse to the direction of wave propagation. Transverse magnetic (TM) mode

represents that the direction of magnetic field is transverse to the direction of wave propagation.

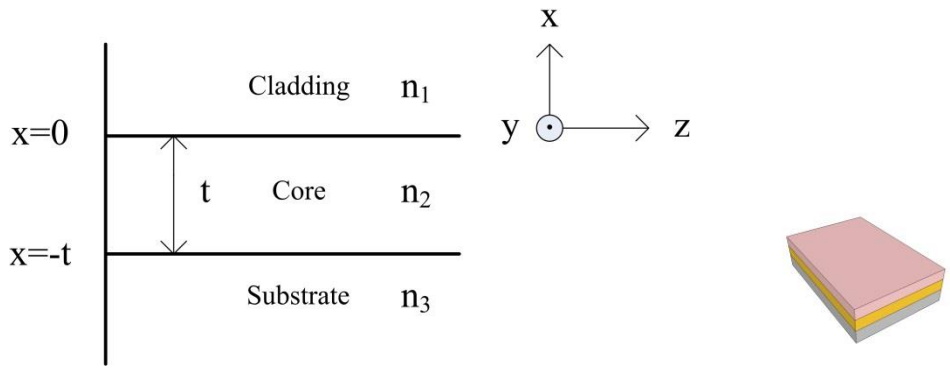

Figure 2.1 Step-index slab waveguide

Assuming φ_0 =0 and harmonic time variation is $e^{j\omega t}$, only spatial part in equation (2.13) is reserved, shown as follows

$$\nabla^2\tilde{E}(\tilde{r})+k_0{}^2n_0{}^2\tilde{E}(\tilde{r})=0 \tag{2.13}$$

Assuming light is propagating along z-axis with propagation constant β, the complex amplitude becomes $\tilde{E}(\tilde{r})=\tilde{E}(x,y,z)=\tilde{E}(x,y)e^{-j\beta z}$. Equation (2.14) can be written as

$$\frac{d^2\tilde{E}(x)}{dx^2}+(k_0{}^2n_0{}^2-\beta^2)\tilde{E}(x)=0 \tag{2.14}$$

Assume the light is in TE polarization. Since there is no restriction in y direction for slab waveguide,

$$\frac{d^2E_y(x)}{dx^2}+(k_0{}^2n_0{}^2-\beta^2)E_y(x)=0 \tag{2.15}$$

We solve the equation for each region (n_1, n_2 and n_3). Depending on $k_0{}^2n_0{}^2$-β^2, the solution is

$$E_y(x) = \begin{cases} C'e^{-qx}, & x > 0 \\ C'[\cos(hx) - \frac{q}{h}\sin(hx)], & -t \le x \le 0 \\ C'[\cos(ht) + \frac{q}{h}\sin(ht)]e^{p(x+t)}, & x < -t \end{cases} \tag{2.16}$$

where

$$\begin{aligned} q &= \sqrt{\beta^2 - k_0{}^2 n_1{}^2} \\ h &= \sqrt{k_0{}^2 n_2{}^2 - \beta^2} \\ p &= \sqrt{\beta^2 - k_0{}^2 n_3{}^2} \end{aligned} \tag{2.17}$$

$$C' = 2h \sqrt{\frac{\omega\mu p}{|\beta|(q^2 + h^2)(t + \frac{1}{q} + \frac{1}{h})}} \tag{2.18}$$

Eigenvalue equation (characteristic equation) represents the relationship between q, h and p:

$$\tan(ht) = \frac{q + p}{h - \frac{q \cdot p}{h}} \tag{2.19}$$

For guided wave propagation,

$$k_0 n_3 < \beta < k_0 n_2 \tag{2.20}$$

Therefore, the propagation constant β for guided wave can defined as

$$\beta = k_0 n_{eff} \tag{2.21}$$

where n_{eff} is the effective index for guided wave.

Equation (2.19) can be solved by numerical computation method or graphical method. Therefore, h, q and p can be found. Depending on n_1, n_2 and n_3, there could be

more than one h value, corresponding to different modes. As shown in Figure 2.2, both sides of the eigenvalue equation are plotted and discrete h values are determined by the crossing points.

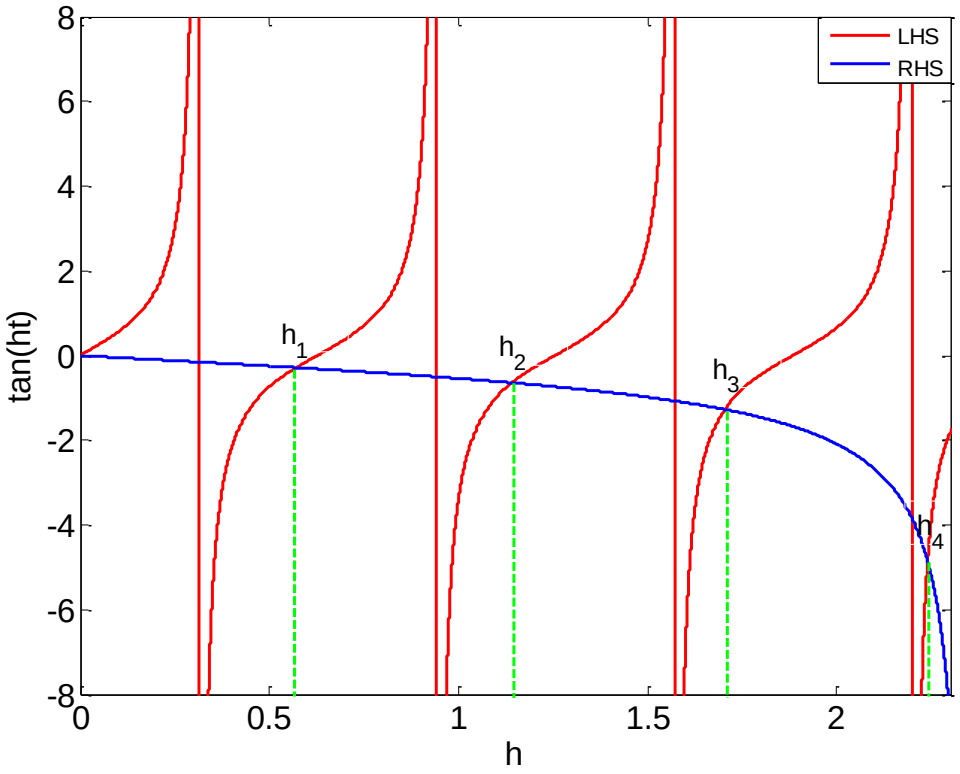

Figure 2.2 Both sides of eigenvalue equation for TE mode

For TM polarization, the solution to equation (2.15) is

$$H_y(x) = \begin{cases} -A'e^{-qx}, & x > 0 \\ A'[-\frac{h}{q}\cos(hx) + \sin(hx)], & -t \le x \le 0 \\ -A'[\frac{h}{q}\cos(ht) + \sin(ht)]e^{p(x+t)}, & x < -t \end{cases} \tag{2.22}$$

where

$$A' = 2\sqrt{\frac{\omega\varepsilon_0 P}{\beta t'}} \tag{2.23}$$

$$t' = \frac{\left(\frac{n_2^{\,2}}{n_1^{\,2}}q\right)^2 + h^2}{\left(\frac{n_2^{\,2}}{n_1^{\,2}}q\right)^2}\left[\frac{t}{n_2^{\,2}} + \frac{q^2+h^2}{\left(\frac{n_2^{\,2}}{n_1^{\,2}}q\right)^2 + h^2}\cdot\frac{1}{n_1^{\,2}q} + \frac{p^2+h^2}{\left(\frac{n_2^{\,2}}{n_3^{\,2}}p\right)^2 + h^2}\cdot\frac{1}{n_3^{\,2}p}\right] \tag{2.24}$$

The eigenvalue equation is

$$\tan(ht) = \frac{\frac{n_2^{\,2}}{n_3^{\,2}}p + \frac{n_2^{\,2}}{n_1^{\,2}}q}{h - (\frac{n_2^{\,2}}{n_1 n_3})^2(\frac{q\cdot p}{h})} \tag{2.25}$$

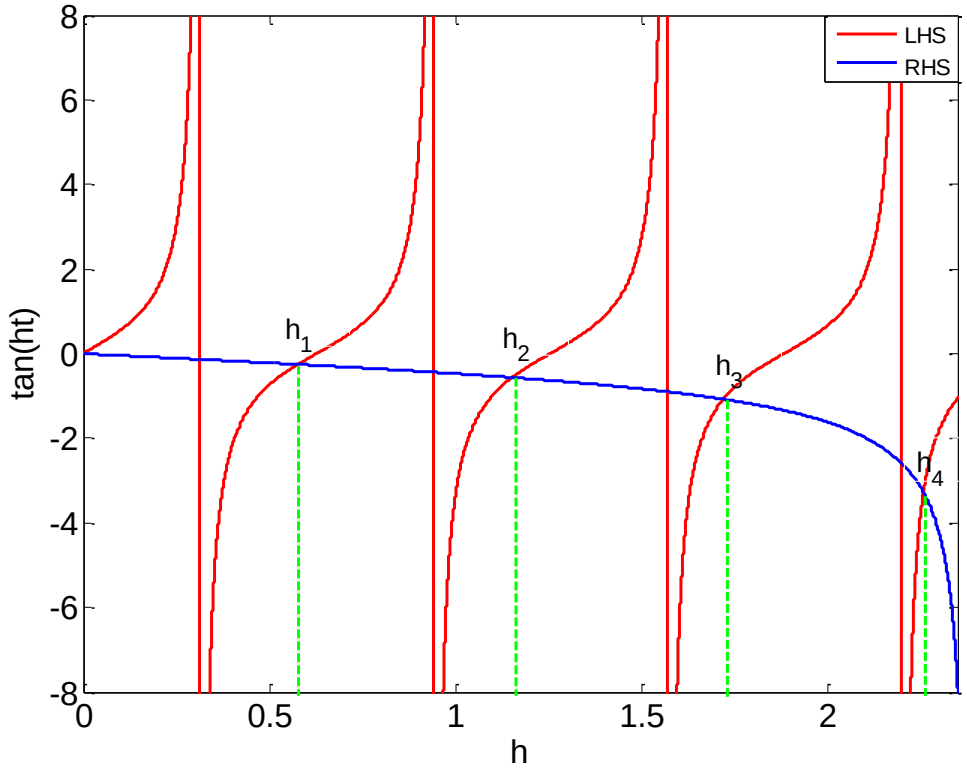

Figure 2.3 Both sides of eigenvalue equation for TM mode

The solutions above in equations (2.19) and (2.25) are for asymmetric slab waveguides. For simplicity, the symmetric slab waveguides are also considered. Because of n_3=n_1, we have simplified equations for both TE and TM polarizations

$$\tan(h\frac{t}{2}) = \begin{cases} \frac{q}{h}, & \text{even modes} \\ -\frac{h}{q}, & \text{odd modes} \end{cases} \tag{2.26}$$

$$\tan(h\frac{t}{2}) = \begin{cases} \left(\frac{n_2}{n_1}\right)^2 \frac{q}{h}, & \text{even modes} \\ -\left(\frac{n_1}{n_2}\right)^2 \frac{h}{q}, & \text{odd modes} \end{cases} \tag{2.27}$$

After finding the solution by numerical computation method or graphical method, the corresponding n_{eff} values for each mode are known. We can plot the electric field distributions for guided modes. For example, the electric field distributions for TE0, TE1 and TE2 modes are displayed in Figure 2.4 below.

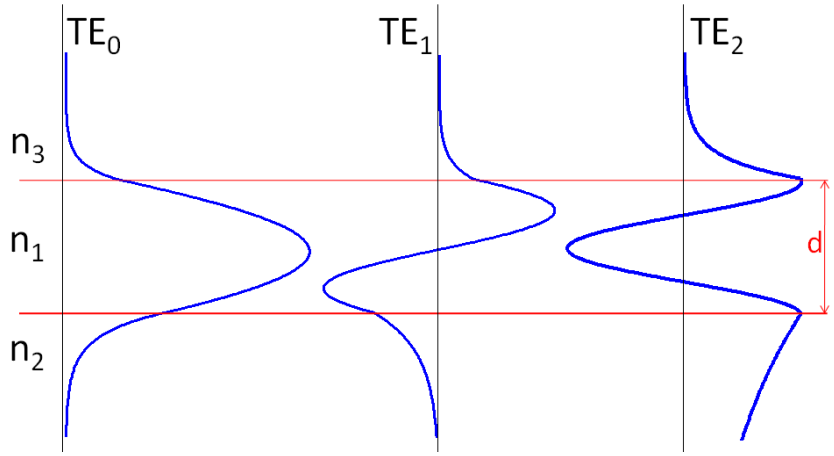

Figure 2.4 Electric field distributions for first three TE modes in an asymmetric slab waveguide

2.2.2 Step-index rectangular waveguides

As shown in Figure 2.5, step-index rectangular waveguides with finite length along z-axis is more practical than slab waveguides. Marcatilis' method, which treats optical modes in x and y directions separately, and then combines them together to obtain an approximate overall solution of the waveguide. The effective index method

improves Marcatilis's method by doing more accurate approximation. Assuming the rectangular in Figure 2.5 is in TE polarization, it can be treated as two different models, the electric fields of which are in vertical direction (TE-like) and horizontal direction (TM-like) respectively. Firstly, the effective index of the electric field in y direction is calculated. And then it is used as core index to obtain the overall effective index by solving the problem as a TM-like model. In other words, the principle of effective index method is to convert a 3D rectangular waveguide into two 2D slab waveguides.

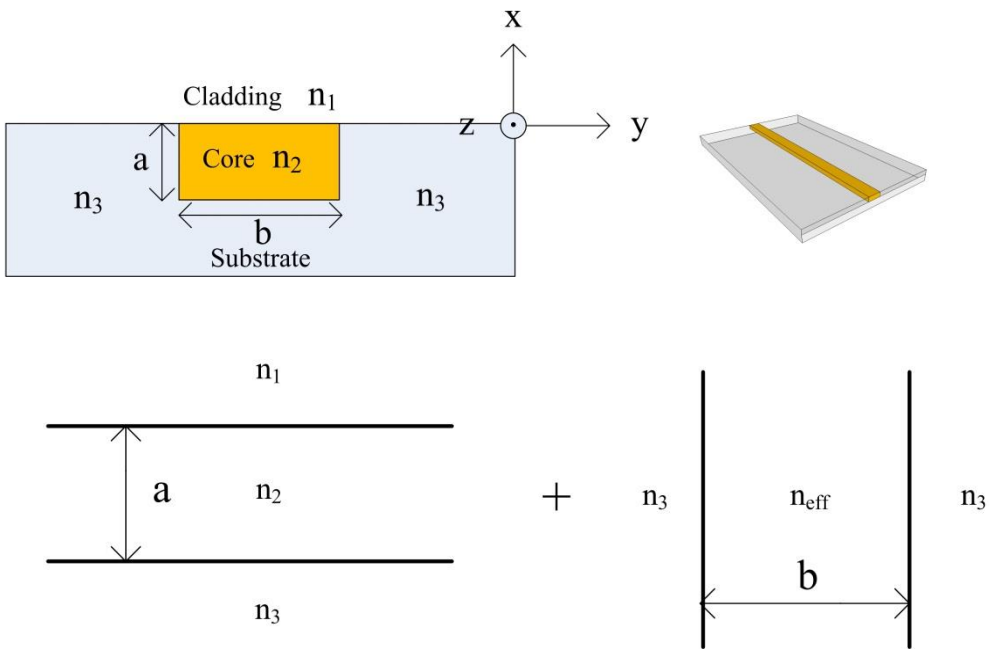

Figure 2.5 (a) 3D step-index rectangular waveguide; (b) 2D slab waveguide in vertical direction; (c) 2D slab waveguide in horizontal direction with core effective index n_{eff} from first 2D waveguide

Although effective index method is fast for analysis of rectangular waveguides, the use is limited by lack of accuracy. It is essential to have commercial softwares with high accuracy for complicated waveguide structures. Commercial softwares, such as

Fimmwave and OptiBPM, can satisfy the strict requirement on accuracy and speed for simulations. They are also capable of calculating kinds of parameters and plotting mode profiles. In this dissertation, Fimmwave from Photon Design Inc. is used for waveguide simulations.

Chalcogenide glasses, containing at least one element (S, Se, or Te), such as arsenic trisulfide (As_2S_3), are amorphous materials with wide infrared transparency (0.2-11μm) and high refractive index ($n=2.43$ at 1550nm), which can be utilized to make low-loss tight bend-radii optical devices with wide operational wavelength, ranging from near infrared to mid infrared. Meanwhile, lithium niobate ($LiNbO_3$), a birefringence material with $n_e=2.13$ and $n_o=2.21$ for extraordinary (TE polarization) and ordinary (TM polarization) indices at 1550nm respectively, is an attractive substrate to integrate with chalcogenide glasses for compact and tunable devices, due to its lower refractive index and fast electro-optic tuning capability. Since the index differences between As_2S_3 and $LiNbO_3$ are 0.3 and 0.23 for TE and TM polarizations, the light can be confined in As_2S_3-on-$LiNbO_3$ waveguides with small dimensions.

Figure 2.6 shows cross section of As_2S_3-on-$LiNbO_3$ in Fimmwave simulation. The refractive index of As_2S_3 is from [11]. Assuming As_2S_3-on-$LiNbO_3$ without cladding layer on top, it is essential to obtain confinement factors with the change of thickness and width for both TE and TM polarizations.

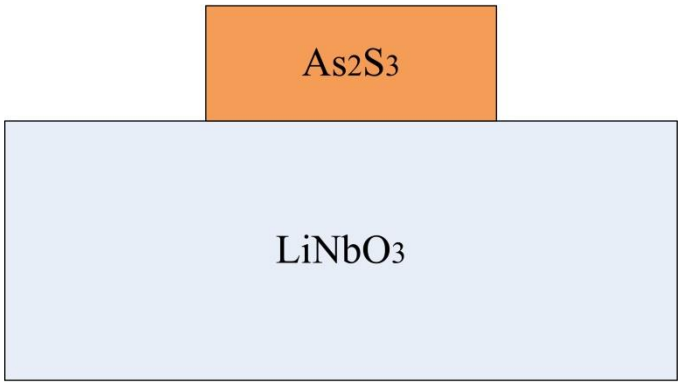

Figure 2.6 Cross-section view of As_2S_3-on-$LiNbO_3$ waveguide

From Figure 2.7, it is obvious that waveguide thickness has a significant impact on mode confinement factor while increasing waveguide width does not affect it after it saturates at a certain width. Under the same width, confinement factor increases with increasing waveguide thickness. When the waveguide width and thickness are the same, the confinement factor of TE polarization is larger, due to the larger index difference compared to TM polarization.

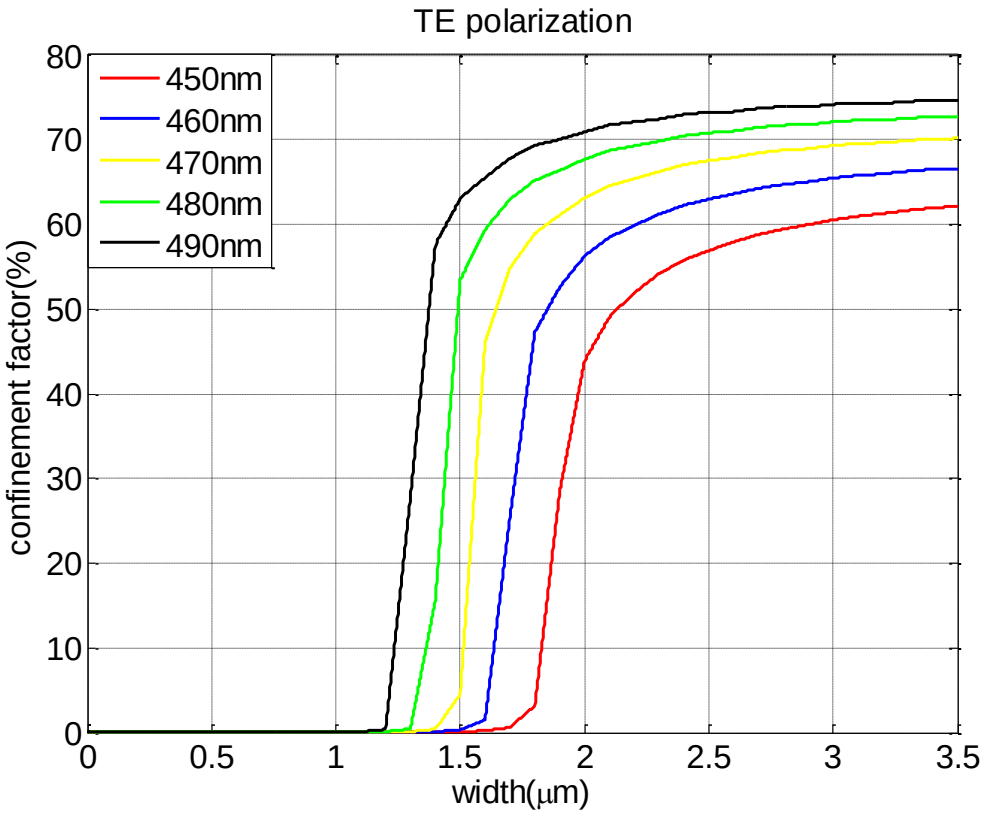

Figure 2.7 Mode confinements for different waveguide heights: (a) TE; (b) TM

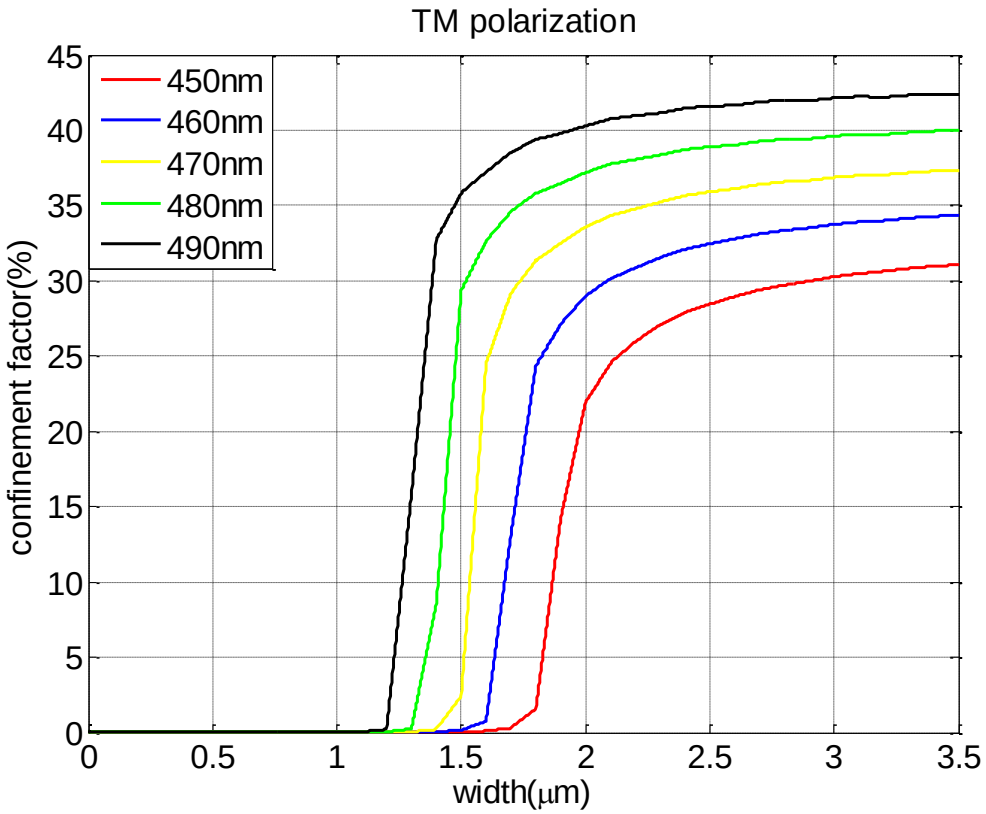

Figure 2.7 Continued

2.2.3 Graded-index waveguides

Graded-index (gradient-index) is from fiber optics, which means that the refractive index of an optical fiber decreases gradually with increasing radial distance from optical axis. Diffused waveguides are typical graded-index waveguides with their low confinement factor and therefore very large mode size. Due to the low mode mismatch loss, they are appropriate to alignment with single mode fiber. Moreover, since the waveguide is diffused into the substrate, which indicates that the mode is propagating below the surface, they are resistant to surface contamination and abrasion.

As shown in Figure 2.8, Titanium diffused lithium niobate waveguides (Ti: LiNbO3) are a classic example of graded-index waveguides.

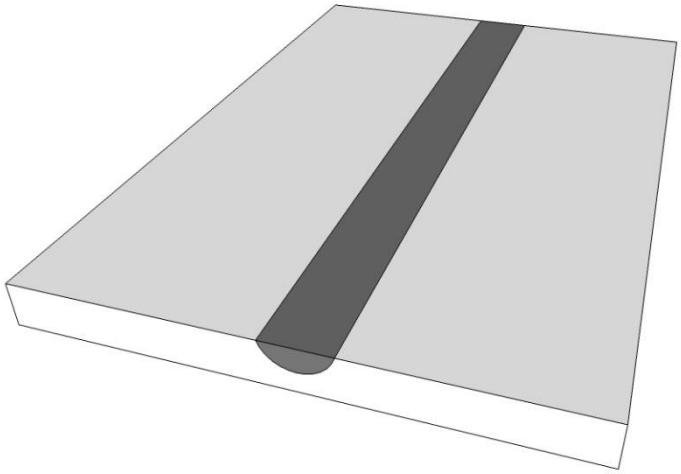

Figure 2.8 Ti: $LiNbO_3$ waveguide

Assuming the substrate is x-cut y-propagating $LiNbO_3$, anisotropic diffusion happens along both x and z axis. The concentration profile of an x-cut y-propagating waveguide can be described as

$$n(x,z) = n_s + \Delta n \cdot f(\frac{x}{D}) \cdot g(\frac{z}{w/2}) \tag{2.28}$$

where D is diffusion depth

$$f(\frac{x}{D}) = e^{-\frac{x^2}{D^2}} \tag{2.29}$$

$$g(\frac{z}{w/2}) = \frac{1}{2}\{erf[\frac{w/2}{D}(1+\frac{z}{w/2})] + erf[\frac{w/2}{D}(1-\frac{z}{w/2})]\} \tag{2.30}$$

Fimmwave is used to do the simulation and plot the mode profiles (Figure 2.9). The effective indices for fundamental TE and TM modes at 1550nm are 2.1386 and 2.2113 respectively. The mode size of TM polarization is slightly larger than that of TE polarization.

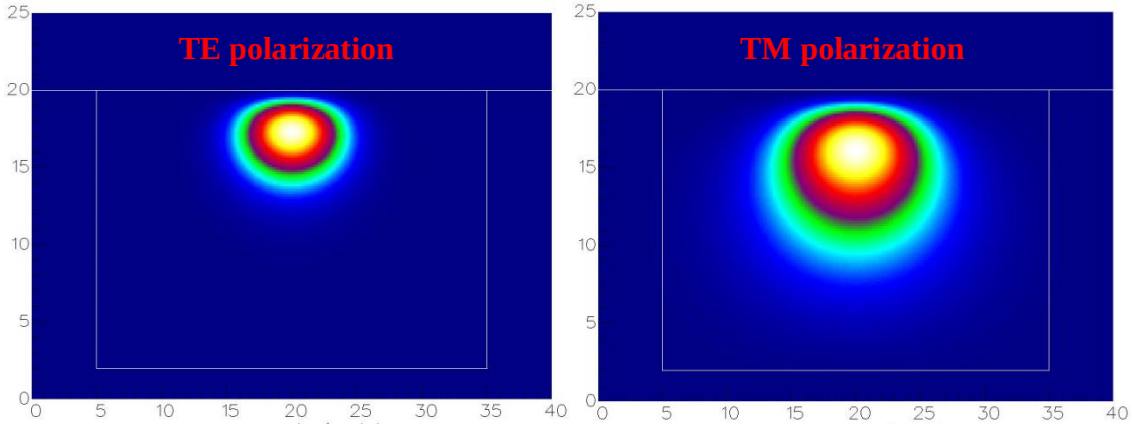

Figure 2.9 Mode profiles of fundamental TE and TM modes

2.3 Four-wave mixing

FWM is a third-order nonlinear process, which is a nonlinear interaction among four photons. Although FWM is detrimental for optical communication systems, it is very useful for a large number of applications. Since FWM requires dispersion engineering and then phase-matching, this chapter discusses them in detail.

2.3.1 Four-wave mixing theory

Nonlinear effects can be categorized into second- or third-order parametric processes, due to if the second-order susceptibility $\chi^{(2)}$ or the third-order susceptibility $\chi^{(3)}$ is responsible. Four-wave mixing (FWM) is a third-order nonlinear process, which only

happens on isotropic medium. Since FWM is polarization dependent, it can be described by

$$P_{NL} = \varepsilon_0 \chi^{(3)} \vdots EEE \tag{2.31}$$

where P_{NL} is the nonlinear polarization. E is the electric field. Assuming four waves at frequencies ω_1, ω_2, ω_3 and ω_4 with linear polarization along x axis, the total electric field is written as

$$E = \frac{1}{2}\hat{x}\sum_{j=1}^{4} E_j e^{i(\beta_j z - \omega_j t)} \tag{2.32}$$

where $\beta = n_j\omega_j/c$ is the propagation constant. n_j is the effective index. If equation (2.32) is substituted in equation (2.31), the nonlinear polarization can be expressed as

$$P_{NL} = \frac{1}{2}\hat{x}\sum_{j=1}^{4} P_j e^{i(\beta_j z - \omega_j t)} \tag{2.33}$$

where P_j consists of terms involving three electric fields. For example, P_4 can be written as

$$P_4 = \frac{3\varepsilon_0}{4}\chi^{(3)}[|E_4|^2 E_4 + 2(|E_1|^2 + |E_2|^2 + |E_3|^2)E_4 + 2E_1E_2E_3e^{(i\theta_+)} + 2E_1E_2E_3{}^* e^{(i\theta_-)} + \cdots] \tag{2.34}$$

where θ_+ and θ_- are

$$\theta_+ = (\beta_1 + \beta_2 + \beta_3 - \beta_4)z - (\omega_1 + \omega_2 + \omega_3 - \omega_4)t \tag{2.35}$$

$$\theta_- = (\beta_1 + \beta_2 - \beta_3 - \beta_4)z - (\omega_1 + \omega_2 - \omega_3 - \omega_4)t \tag{2.36}$$

The first four terms in equation (2.34) denote self-phase modulation and cross-phase modulation, which are not discussed in this dissertation. θ_+ and θ_- are responsible for

FWM, which photons are annihilated and new photons are generated at different frequencies in an isotropic medium.

Based upon equations (2.35) and (2.36), there are two kinds of FWM. Equation (2.35) corresponds to the situation that a new photon at frequency ω_4 is created by three photons at frequencies ω_1, ω_2 and ω_3. Generally speaking, it is difficult to meet the phase-matching condition in this case. In contrast, the FWM process denoted by equation (2.36) is achievable. The two photons at frequencies ω_1 and ω_2 are annihilated and two photons at frequencies ω_3 and ω_4 are created at the same time.

$$\omega_3 + \omega_4 = \omega_1 + \omega_2 \tag{2.37}$$

The phase-matching condition for this case is

$$\Delta\kappa = \beta_3 + \beta_4 - \beta_1 - \beta_2 = (n_3\omega_3 + n_4\omega_4 - n_1\omega_1 - n_2\omega_2)/c \tag{2.38}$$

In order to achieve high efficiency FWM, $\Delta\kappa$ is supposed to be zero.

If $\omega_1 = \omega_2$, it is called degenerate FWM, in which the input is at single frequency. Assuming $\omega_4 > \omega_3$, equation (2.37) can be written as

$$\omega_1 - \omega_3 = \omega_4 - \omega_1 \tag{2.39}$$

In this case, an intense pump wave at frequency ω_1 creates two waves at frequencies ω_3 and ω_4 located symmetrically as two sidebands (Figure 2.10). ω_3 and ω_4 are often called signal and idler waves respectively.

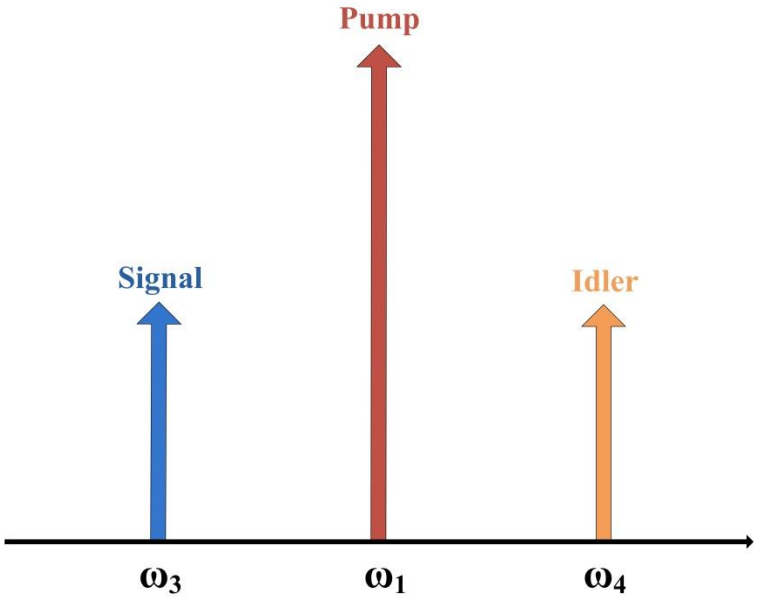

Figure 2.10 Degenerate FWM

2.3.2 Coupled differential equations

FWM can be described by the following coupled differential equations

$$\frac{dA_1}{dz} = \frac{in_2\omega_1}{c}[(f_{11}|A_1|^2 + 2\sum_{k\neq 1} f_{1k}|A_k|^2)A_1 + 2f_{1234}A_2^* A_3 A_4 e^{i\Delta\kappa z}] \quad (2.40)$$

$$\frac{dA_2}{dz} = \frac{in_2\omega_2}{c}[(f_{22}|A_2|^2 + 2\sum_{k\neq 2} f_{2k}|A_k|^2)A_2 + 2f_{2134}A_1^* A_3 A_4 e^{i\Delta\kappa z}] \quad (2.41)$$

$$\frac{dA_3}{dz} = \frac{in_2\omega_3}{c}[(f_{33}|A_3|^2 + 2\sum_{k\neq 3} f_{3k}|A_k|^2)A_3 + 2f_{3412}A_1 A_2 A_4^* e^{-i\Delta\kappa z}] \quad (2.42)$$

$$\frac{dA_4}{dz} = \frac{in_2\omega_4}{c}[(f_{44}|A_4|^2 + 2\sum_{k\neq 4} f_{4k}|A_k|^2)A_4 + 2f_{4312}A_1 A_2 A_3^* e^{-i\Delta\kappa z}] \quad (2.43)$$

where A_j is the complex electric field amplitude at frequency ω_j. $\Delta\kappa$ is the phase mismatch. n_2 is the nonlinear refractive index. f_{ijkl} is the overlap integral.

$$f_{ijkl} = \frac{\left\langle F_i^* F_j^* F_k F_l \right\rangle}{\left[\left\langle |F_i|^2 \right\rangle \left\langle |F_j|^2 \right\rangle \left\langle |F_k|^2 \right\rangle \left\langle |F_l|^2 \right\rangle \right]^{1/2}} \tag{2.44}$$

where angle brackets denote the integration over the transverse distribution in x and y. F_j is the transverse distribution of the guided mode.

Since equations (2.40) to (2.43) are a general description of FMW process, it is necessary to obtain a numerical approach to solve them exactly. Considerable understanding can be obtained by assuming the pump waves to be much stronger than other waves such that the pump remains undepleted during FWM process. As a further simplification, we assume that all overlap integrals are nearly the same, that is [12],

$$f_{ijkl} \approx f_{ij} \approx 1/A_{eff} \quad (i, j, k, l = 1, 2, 3, 4) \tag{2.45}$$

where A_{eff} is the effective mode area. The nonlinear coefficient γ is introduced,

$$\gamma_j = n_2 \omega_j / \left(c A_{eff} \right) \approx \gamma \tag{2.46}$$

where the differences in frequencies of four waves are ignored. Therefore, the solutions to equation (2.40) and (2.41) are

$$A_1(z) = \sqrt{P_1} e^{i\gamma(P_1 + 2P_2)z} \tag{2.47}$$

$$A_2(z) = \sqrt{P_2} e^{i\gamma(P_2 + 2P_1)z} \tag{2.48}$$

where P_1 and P_2 are pump powers at $z=0$. The solutions indicate that pump waves are only phase shifted in FWM process when they keep undepleted.

Substituting equations (2.47) and (2.48) in equations (2.42) and (2.43), the coupled equations for signal and idler waves can be simplified

$$\frac{dA_3}{dz} = 2i\gamma[(P_1 + P_2)A_3 + \sqrt{P_1P_2}e^{-i\theta}A_4^*] \tag{2.49}$$

$$\frac{dA_4^*}{dz} = -2i\gamma[(P_1 + P_2)A_4^* + \sqrt{P_1P_2}e^{i\theta}A_3] \tag{2.50}$$

where $\theta=[\Delta\kappa-3\gamma(P_1+P_2)]z$. In order to solve these equations, we define

$$B_j = A_j e^{-2i\gamma(P_1+P_2)z},\ (j = 3, 4) \tag{2.51}$$

Substituting equation (2.51) in equations (2.49) and (2.50), we obtain

$$\frac{dB_3}{dz} = 2i\gamma\sqrt{P_1P_2}e^{-i\kappa z}B_4^* \tag{2.52}$$

$$\frac{dB_4^*}{dz} = -2i\gamma\sqrt{P_1P_2}e^{i\kappa z}B_3 \tag{2.53}$$

where $\kappa=\Delta\kappa+\gamma(P_1+P_2)$ is the phase mismatch. Therefore, B_3 and B_4^* can be solved easily

$$B_3(z) = (a_3e^{gz} + b_3e^{-gz})e^{-ikz/2} \tag{2.54}$$

$$B_4^*(z) = (a_4e^{gz} + b_4e^{-gz})e^{ikz/2} \tag{2.55}$$

where a_3, b_3, a_4 and b_4 are determined by boundary conditions. The parametric gain g is defined as

$$g = \sqrt{(\gamma P_0)^2 - (\kappa/2)^2} \tag{2.56}$$

where $P_0=P_1+P_2$ is the total pump power. This solution is only valid when the pump waves are much more intense than other waves and remain undepleted during the FWM process. From equation (2.56), it is obvious that the maximum parametric gain occurs at $\kappa=0$ is

$$g_{\max} = \gamma P_0 \tag{2.57}$$

2.3.3 Parametric amplification

One the most important properties of FWM is parametric amplification to input waves. Assuming both signal and idler waves with undepleted pump waves are launched at z=0, equations (2.53) and (2.54) can be written as

$$a_3 + b_3 = B_3(0) \tag{2.58}$$

$$g(a_3 - b_3) = (i\kappa/2)(a_3 + b_3) + 2i\gamma\sqrt{P_1P_2}B_4^*(0) \tag{2.59}$$

We can obtain a3 and b3 by solving these equations.

$$a_3 = \frac{1}{2}(1 + i\kappa/2g)B_3(0) + iC_0B_4^*(0) \tag{2.60}$$

$$b_3 = \frac{1}{2}(1 - ik/2g)B_3(0) - iC_0B_4^*(0) \tag{2.61}$$

where $C_0 = (\gamma/g)\sqrt{P_1P_2}$. Similarly, the constants a_4 and b_4 can also be determined. Therefore, equations (2.54) and (2.55) can be solved and we can acquire the signal and idler amplitudes at distance z.

$$B_3(z) = \{B_3(0)[\cosh(gz) + (i\kappa/2g)\sinh(gz)] + iC_0B_4^*(0)\sinh(gz)\}e^{-i\kappa z/2} \tag{2.62}$$

$$B_4^*(z) = \{B_4^*(0)[\cosh(gz) - (i\kappa/2g)\sinh(gz)] - iC_0B_3(0)\sinh(gz)\}e^{i\kappa z/2} \tag{2.63}$$

We can obtain the solution easily by assuming signal wave B_3 is only launched at $z=0$ and $B_4^*=0$. The signal power P_3 is

$$P_3(z) = |B_3(z)|^2 = P_3(0)[1 + (1 + \kappa^2/4g^2)\sinh^2(gz)] \tag{2.64}$$

Similarly, the idler power P_4 can be found,

$$P_4(z) = |B_4(z)|^2 = P_3(0)(1 + \kappa^2/4g^2)\sinh^2(gz) \tag{2.65}$$

Equation (2.65) indicates that the idler power is created immediately after the pump and signal waves are launched. Its power increases as z^2 initially, but both the signal and idler grow exponentially after a distance such that $gz>1$ [12]. Eventually, the idler power can build up to almost the same level as the signal power. It has all features of the signal except its phase is conjugated.

In general, FWM is a nonlinear process that can create an idler wave and amplify a weak input signal wave simultaneously. The amplification factor is derived from equation (2.64) and can be described as

$$G = \frac{P_3(L)}{P_3(0)} = 1 + (\gamma P_0 / g)^2 \sinh^2(gL) \tag{2.66}$$

where P_0 is the total pump power. g is the parametric gain showing in equation (2.56) , which varies with P_0 and the phase mismatch κ. In practice, $\kappa=\Delta\kappa+\gamma(P_1+P_2)$ in which $\Delta\kappa$ in equation (2.38) is the linear phase mismatch.

Since the amplification factor is strongly dependent on κ, it is small if the phase matching condition is not satisfied. On the other hand, it increases exponentially with input pump power P_0 if $\kappa=0$.

$$G \approx \frac{1}{4} e^{2\gamma P_0 L} \tag{2.67}$$

The amplification bandwidth $\Delta\Omega$ is another important parameter of the FWM process, which is defined as the FWHM of $G(\omega_3)$. It depends on total pump power P_0, medium length L and the phase mismatch κ. Assuming $\Delta\Omega \ll |\omega_1 - \omega_3|$, we have

$$\Delta\Omega = \frac{\pi}{L} (2\gamma P_0 |\beta_2|)^{-1/2} \tag{2.68}$$

where $\beta_2 = -\frac{\lambda^2 D}{2\pi c}$ is the group-velocity dispersion (GVD) parameter. D is the dispersion. Since β_2 is usually a negative number, the absolute value denoted by bars is used in this equation. For relatively short nonlinear medium, the amplification bandwidth is approximated written as

$$\Delta\Omega \approx \sqrt{\frac{\gamma P_0}{2|\beta_2|}} \tag{2.69}$$

CHAPTER III

DEVICE DESIGN AND SIMULATION*

After proving loss propagation loss of As_2S_3-on-$LiNbO_3$ waveguides in previous work, it is a good time to exploit its applications in mid-IR wavelength. FWM occurs only if the phase-matching condition is satisfied. Unlike Raman or Brillouin scattering, the phase-matching condition of FWM is not met automatically. In particular, high efficiency FWM requires specific waveguide designs and choice of input wavelengths to achieve it.

In this chapter, on one hand, two As_2S_3-on-$LiNbO_3$ waveguide designs are demonstrated, which have near zero dispersion at a pump wavelength of 2.05 μm and satisfy the phase-matching condition at a signal wavelength of 1.55 μm. The corresponding idler wavelength is 3.03 μm which is an operation wavelength for trace gas detection systems [13]. Through simulations, we verify that the parametric conversion efficiency is -8 dB for pump power intensity of 0.1 GW/cm^2. Under the same intensities, our results are 20 dB better than the results of silicon waveguides in [14]. The fabrication tolerance of the designs is also discussed.

*Part of this chapter is reprinted with permission from "Q. Chen, X. Wang and C. Madsen, "Phase-Matching and Parametric Conversion for the Mid-Infrared in As_2S_3 Waveguides," Optics and Photonics Journal in SRP, Vol.2 No.4, December 2012, DOI: 10.4236/opj.2012.24031.

On the other hand, since the signal and the idler can be interchangeable in FWM, it provides us a solution to convert mid-IR wavelength to near-IR wavelength for indirect detection for high speed processing of mid-IR signal with good noise performance. Therefore, another As_2S_3-on-$LiNbO_3$ waveguide design is proposed, which is able to up-convert mid-IR signals at 4.6 μm to near-IR idlers at 1.32 μm with high parametric conversion efficiency. We investigate the improvement in electrical signal-to-noise ratio (eSNR) by analyzing different types of noise principles for state of the art commercial detectors. Our calculation indicates that the indirect detection by FWM can increase the eSNR up to 67 dB compared to direct detection by PbSe and HgCdTe (MCT) detectors, especially for weak mid-IR signals. Again, our result is 17 dB higher than the result for silicon waveguides in [15].

3.1 Dispersion engineering

To satisfy the phase-matching condition, dispersion engineering is required. In the first place, it is essential to maintain the very low dispersion at the pump wavelength by varying the waveguide width because dispersion is sensitive to it. At the same time, in order to achieve high efficient FWM, it is required to tune the 100 % phase-matching efficiency to signal wavelength by changing waveguide or cladding thickness. Figure 3.1 (a) and (b) exhibit that the structures of As_2S_3 waveguide with and without MgF_2 top cladding. The reason to simulate different designs is to evaluate the influence of MgF_2 on FWM conversion bandwidth.

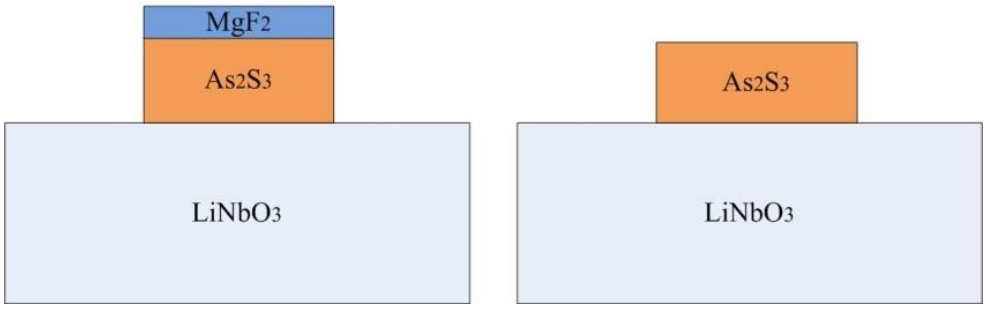

Figure 3.1 (a) As_2S_3 waveguide with MgF_2 cladding; (b) without cladding

Since 2.05 μm laser and 1.55 μm laser are available as the pump and signal sources in our lab, it is necessary to make designs suitable for these specific wavelengths. All simulations are from Fimmwave, a commercial software by Photo Design Inc. Python is also used to automatically control the simulation process, because it is essential to collect a large quantity of data at different wavelengths. For instance, in order to find the wavelength with 100% phase-matching efficiency, we should simulate

designs from 1.3 μm to 3.3 μm. Furthermore, due to the birefringence of $LiNbO_3$, both TE and TM polarizations are supposed to be taken into consideration.

The resulting dispersion curves for the fundamental TE mode are demonstrated in Figure 3.2. When the waveguide width is 1.4 μm and the height is 1.7 μm with 0.18 μm MgF_2 cladding on top, the dispersion at 2.05 μm is 1.2 ps/nm/km which is very close to zero; when the waveguide width is 1.5 μm and the height is 1.685 μm without a cladding material, the zero dispersion wavelength is exactly 0 ps/nm/km at 2.05 μm. The waveguide designs for TM polarization cannot achieve 100% phase-matching efficiency at signal wavelength.

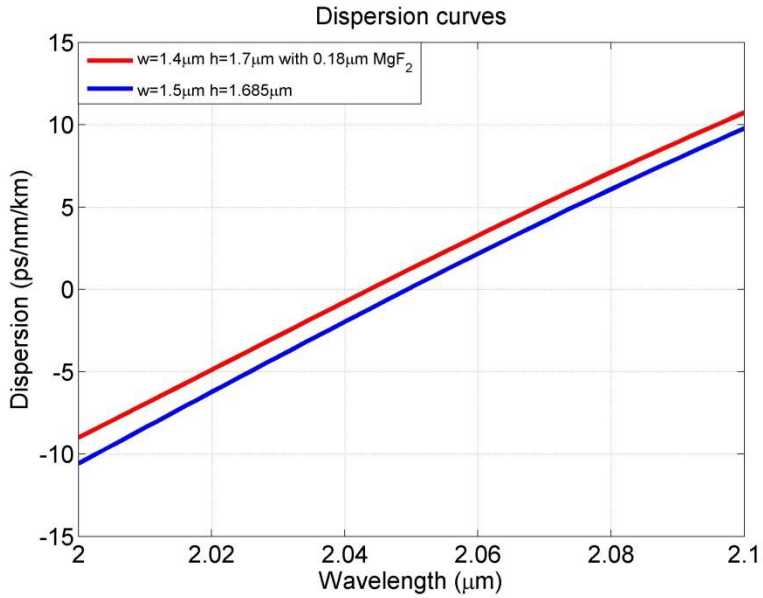

Figure 3.2 Dispersion curves for two As_2S_3 waveguide designs

3.2 FWM phase-matching efficiency

For degenerate FWM, the relationship of the three wavelengths can be described by equation (3.1):

$$\frac{1}{\lambda_i} = \frac{2}{\lambda_p} - \frac{1}{\lambda_s} \tag{3.1}$$

where λ_p, λ_s and λ_i are pump, signal and idler wavelengths. The FWM phase-matching efficiency depends on how well the phase-matching condition is satisfied:

$$\Delta\kappa = 2\pi\left(\frac{n_s}{\lambda_s} + \frac{n_i}{\lambda_i} - 2\frac{n_p}{\lambda_p}\right) + 2\gamma P_p \tag{3.2}$$

$$\gamma = \frac{2\pi n_2}{\lambda_p A_{eff}} \tag{3.3}$$

where n_p, n_s and n_i are effective indices of pump, signal and idler wavelengths; P_p is pump power. γ is nonlinearity coefficient. n_2 is the nonlinear refractive index of As_2S_3 [16]. A_{eff} is effective mode area at pump wavelength, which are 1.84 μm^2 and 1.99 μm^2 for the structures with and without MgF_2 cladding on top, respectively.

If the phase-matching condition is achieved, the FWM phase-matching efficiency can be very high. It is described by the following formula in [16]:

$$\eta^2 = \frac{{\alpha_0}^2}{{\alpha_0}^2 + \Delta\kappa^2}\left[1 + 4e^{-\alpha_0 L}\frac{\sin^2(L\Delta\kappa/2)}{(1-e^{-\alpha_0 L})^2}\right] \tag{3.4}$$

where α_0 is the waveguide propagation loss at 2.05 μm. We use a value of 0.33 dB/cm from our previous work in [17]. Since two-photon absorption (TPA) coefficient of As_2S_3 is very low, the nonlinear loss due to it can be neglected. L is the length of As2S3 waveguide which is 4 cm in the simulation. From equation (3.4), it is obvious that FWM phase-matching efficiency is dominant by phase-matching condition, which is described by equation (3.2).

Figure 3.3 shows the phase-matching curves for the two As_2S_3 waveguide structures. The phase-matching condition is met at 1.55 μm, 3.03 μm and the region around the pump wavelength, which means that the FWM phase-matching efficiency, depicted in Figure 3.4, can be as high as 100 % at these wavelengths for both designs. In wavelength regions near 1.55 and 3.03 μm, the full width at half maximum (FWHM) of the structure without cladding is 25 nm, which is 9 nm wider than that of structure with MgF_2 cladding on top.

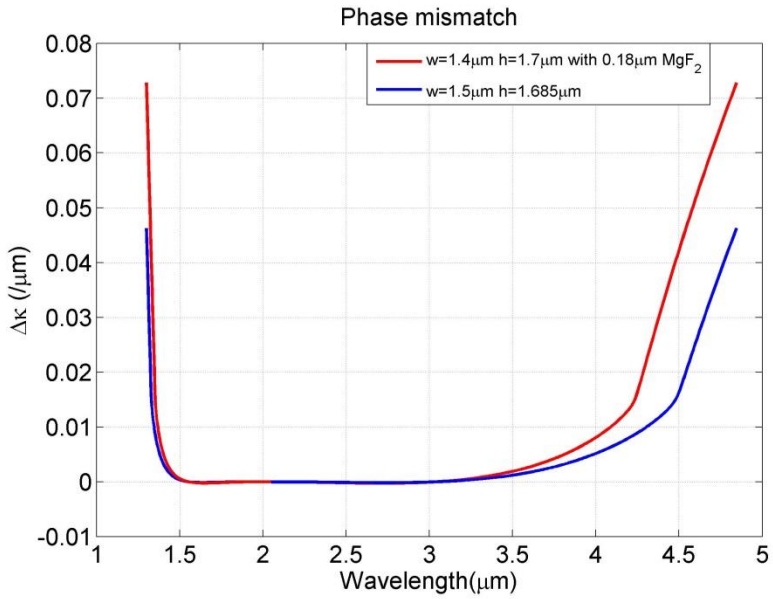

Figure 3.3 Phase mismatch as a function of signal wavelength

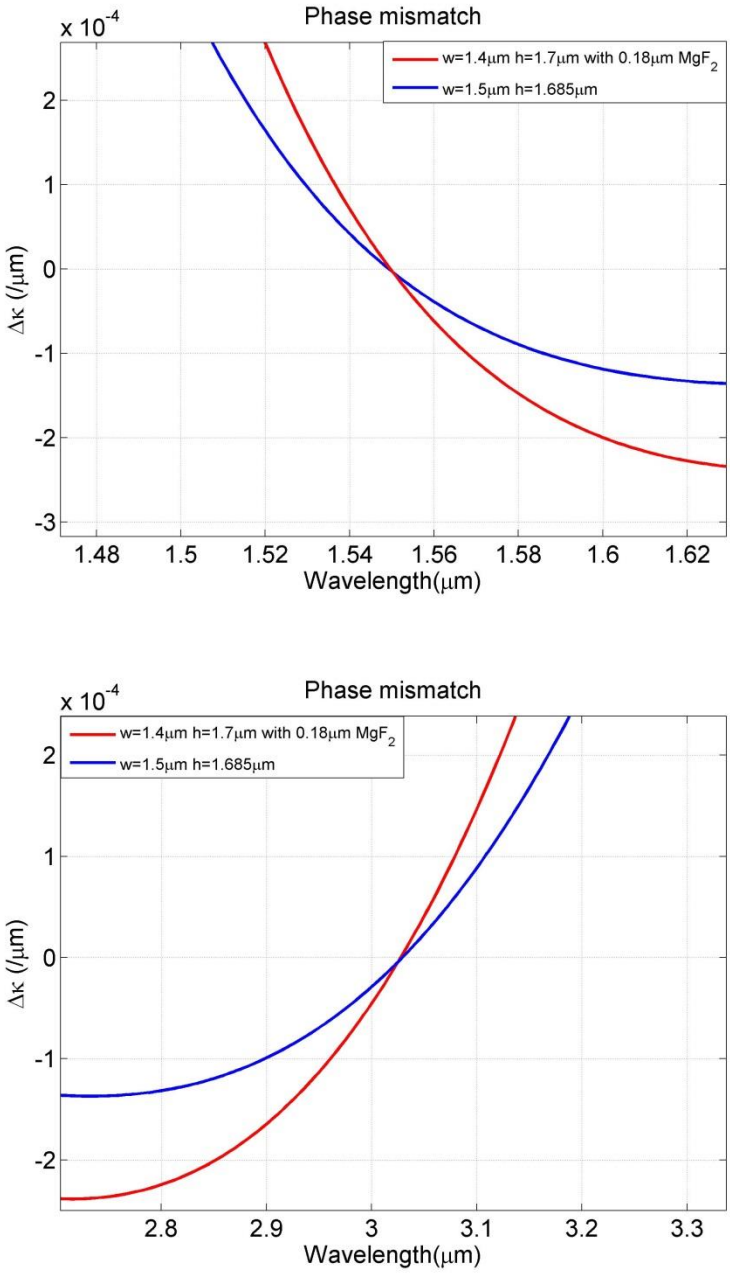

Figure 3.3 Continued

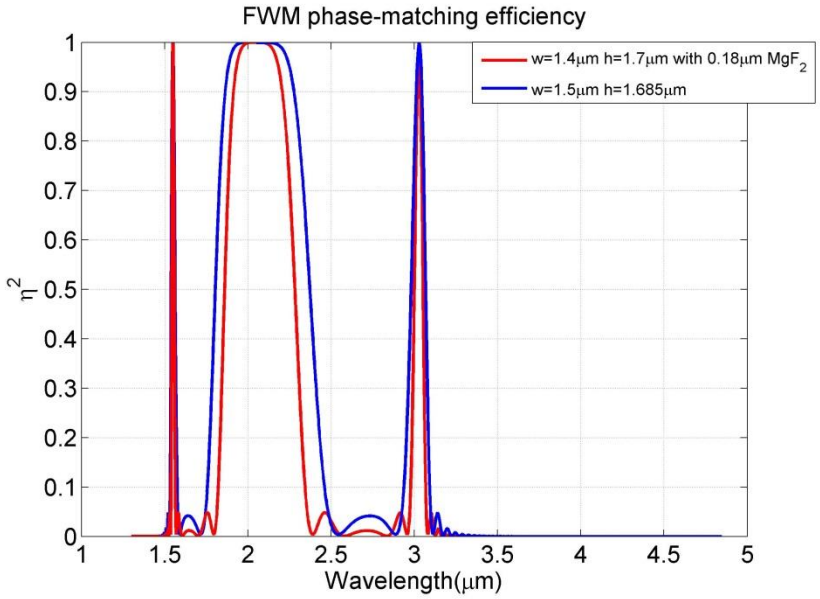

Figure 3.4 FWM phase-matching efficiency as a function of signal wavelength

3.3 Parametric conversion efficiency

FWM can be described by the following coupled differential equations for pump, signal and idler waves [18].

$$\frac{\partial A_p}{\partial z} = i\gamma(|A_p|^2 + 2|A_i|^2 + 2|A_s|^2)A_p + 2\gamma A_i A_s A_p^* \exp(i\Delta\kappa z) \tag{3.5}$$

$$\frac{\partial A_i}{\partial z} = i\gamma(|A_i|^2 + 2|A_s|^2 + 2|A_p|^2)A_i + \gamma A_p^2 A_s^* \exp(-i\Delta\kappa z) \tag{3.6}$$

$$\frac{\partial A_s}{\partial z} = i\gamma(|A_s|^2 + 2|A_i|^2 + 2|A_p|^2)A_s + \gamma A_p^2 A_i^* \exp(-i\Delta\kappa z) \tag{3.7}$$

where A_p, A_s and A_i denote the complex electric field amplitude of pump, signal and idler wavelengths, respectively. An improved understanding can be obtained by considering a strong pump and a weak signal incident such that the pump remains undepleted during

the FWM process [18]. Therefore, the coupled differential equations can be solved by an analytic method. The parametric conversion efficiency is described by equation (3.8).

$$G_i = [\frac{\gamma P_p}{g} \sinh(gL_{eff})]^2 \tag{3.8}$$

where g is parametric gain and L_{eff} is the effective As_2S_3 waveguide length for nonlinear process. They can be expressed by equation (3.9) and (3.10).

$$g = \sqrt{(\gamma P_p)^2 - (\Delta\kappa/2)^2} \tag{3.9}$$

$$L_{eff} = \frac{1 - \exp(-\alpha_0 L)}{\alpha_0} \tag{3.10}$$

For simulation purposes, the pump power intensity coupled into the As_2S_3 waveguide are chosen to be 0.1 GW/cm^2 and 0.01 GW/cm^2, respectively. The parametric conversion efficiency G_i is shown in Figure 3.5. When L is 4 cm, G_i is -8 dB and -28 dB for each pump power intensity. Under the same intensities, our results are 20 dB larger than the parametric conversion efficiency of silicon waveguides in [19]. The remarkable improvement is mainly attributed to the 100 % FWM phase-matching efficiency η^2.

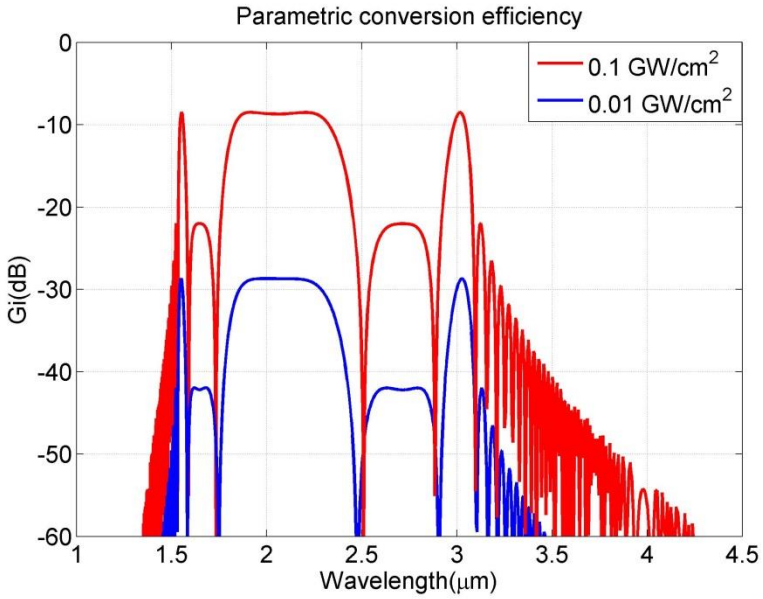

Figure 3.5 Parametric conversion efficiency

3.4 Fabrication tolerances

In addition to the high nonlinearity, chalcogenide glass exhibits photosensitivity, too [20]. We have studied the photodarkening effect of As_2S_3 in a hybrid Mach-Zehnder interferometer [21]. A uniform exposure to intensive green light can increase As_2S_3 refractive index by 1% [22], which can change the phase-matching condition of the As_2S_3 waveguides and provide the tuning ability after traditional photolithography. Figure 3.6 displays that the FWM phase-matching efficiency curves for the design with MgF_2 cladding on top when the refractive index, waveguide width or waveguide height is changed. These cases may happen during fabrication. The changes shift the 100 % phase-matching efficiency wavelength, which is summarized in Table 1.

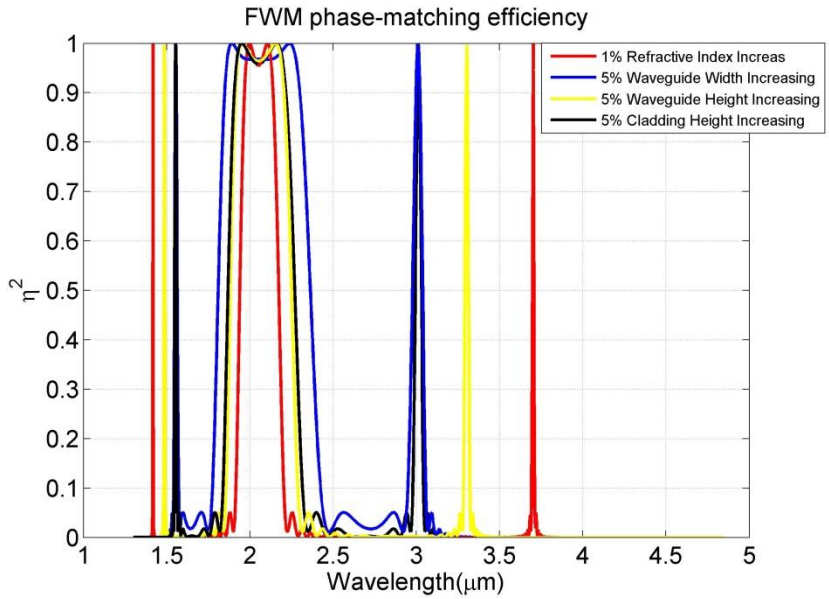

Figure 3.6 FWM phase-matching efficiency

Table 1. 100 % phase-matching efficiency wavelengths for fabrication tolerances

	100 % FWM phase-matching efficiency wavelength (μm)	Idler wavelength (μm)
1% refractive index increasing of As_2S_3	1.418	3.698
5% waveguide width increasing	1.555	3.007
5% waveguide height increasing	1.486	3.304
5% cladding height increasing	1.554	3.013

Figure 3.6 demonstrates the parametric conversion efficiency curves corresponding to the different As_2S_3 waveguide lengths for 0.1 GW/cm^2 pump power intensity. Due to the length dependence of phase-matching ($L\Delta\kappa$), the conversion bandwidth increases with the decreasing waveguide length. It is noticeable that When L

is 1 cm (L_{eff} = 0.96 cm), the conversion bandwidth is 1525 nm with -21 dB parametric conversion efficiency, which indicates that we can achieve continuously tunable FWM between the near-IR and mid-IR.

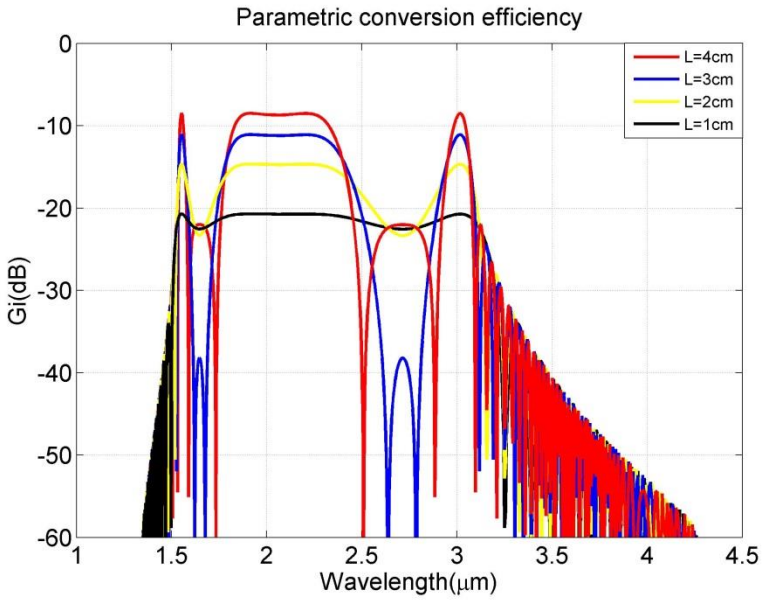

Figure 3.7 Parametric conversion efficiency as a function of waveguide length

3.5 FWM measurement

3.5.1 FWM measurement setup

Since the As_2S_3-on-$LiNbO_3$ designs for FWM are verified by simulation, the next step is to achieve it experimentally. The schematic diagram of FWM measurement setup is demonstrated in Figure 3.8. The pump source is a 2.05 μm thulium doped CW fiber laser. The maximum power is 1W. A 1.55 μm fiber laser is our signal source with maximum power of 14 mW, which can be further increased by EDFA. Collimators make the beams propagate via free space. We use a longpass dichroic mirror as a beam combiner to make pump and signal beams from different lasers collinear. A black

diamond (BD) lens with small focal length can focus the collimated beams and minimize the beam-to-waveguide coupling loss, because the focused beam sizes are proportional to the focal length. Then, another BD lens is able to collect the pump, signal and idler light and collimate them. Fourier transform infrared spectroscopy (FTIR) is used as a detector to show the output spectrum by which we can make a comparison on parametric conversion efficiency between simulation and measurement.

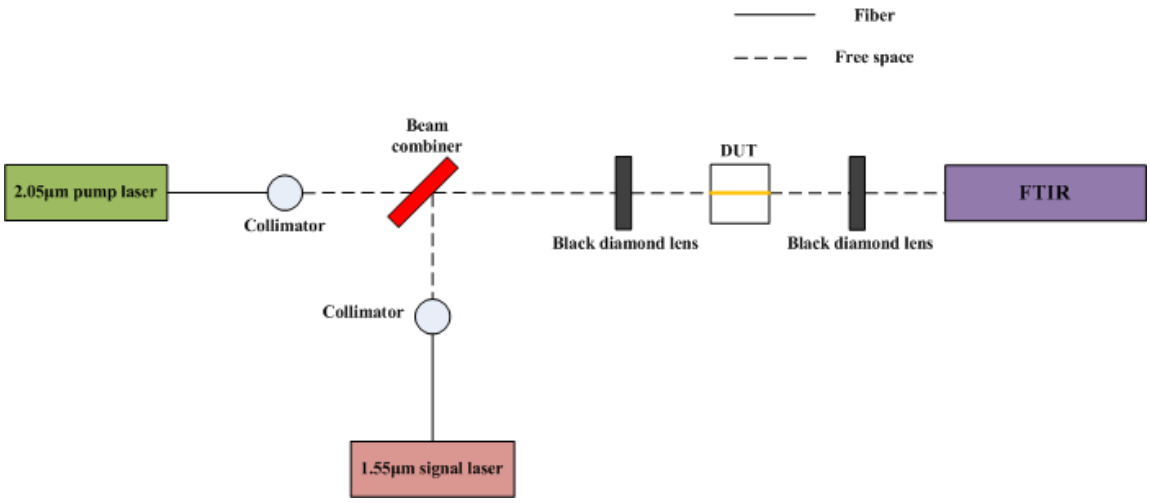

Figure 3.8 FWM measurement setup

3.5.2 Beam-to-waveguide coupling loss

Beam-to-waveguide coupling losses for pump and signal beams are simulated by Zemax. Since pump power coupled into the waveguide is very important, it is necessary to maximize it by optimizing the distance between input BD lens and the waveguide. In our FWM measurement system on an optical table, the total distance between the collimator and BD lens is 203.2 mm. Lens specifications can be found in www.thorlabs.com/thorProduct.cfm?partNumber=C037TME-D. The ray trace before

and after it is shown in Figure 3.9. The optimized back focal length (f_b) by ZEMAX at 2.05 μm is 0.777 mm. The half divergence angle of the input beam is 0.0365°, which makes the green beam away from Z-axis. As the reference, the blue beam is strictly propagating along Z-axis. From the full field spot diagram in Figure 3.10, we can get RMS radius of the focused beam after BD lens, 1.081 μm, which is the key parameter to calculate the beam-to-waveguide coupling loss. On the basis of the mode field dimensions of As_2S_3-on-$LiNbO_3$ waveguide without MgF_2, 1.793 μm×1.708 μm, the beam-to-waveguide coupling loss is 0.2 dB at pump wavelength.

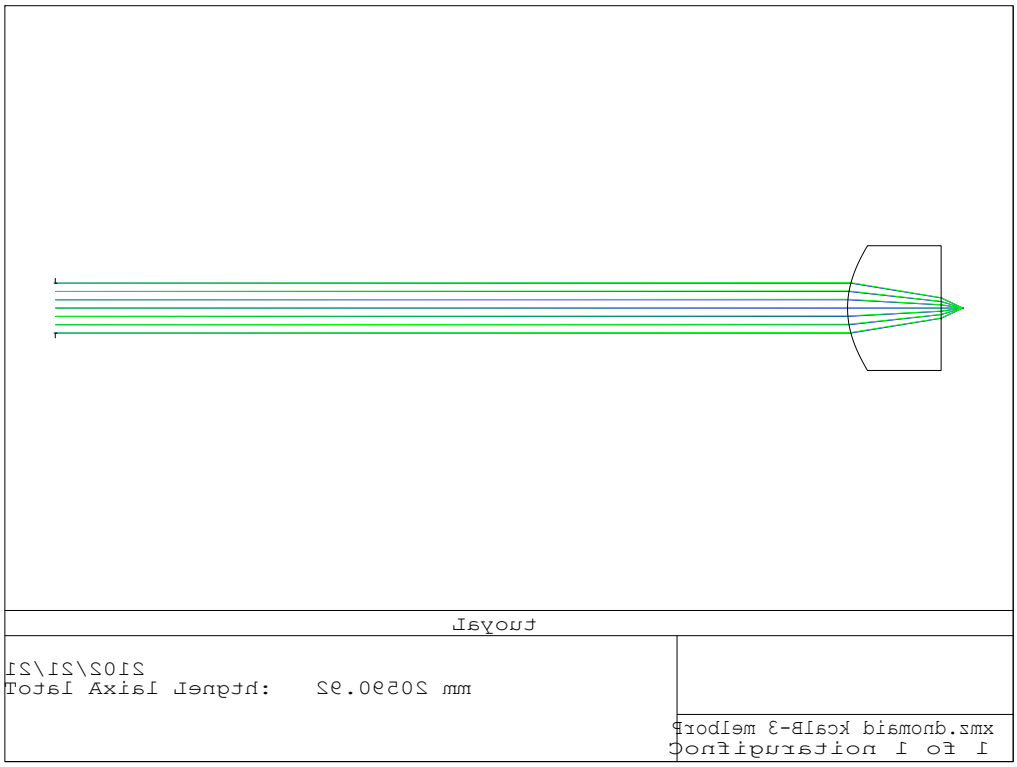

Figure 3.9 Ray trace before and after BD lens at pump wavelength

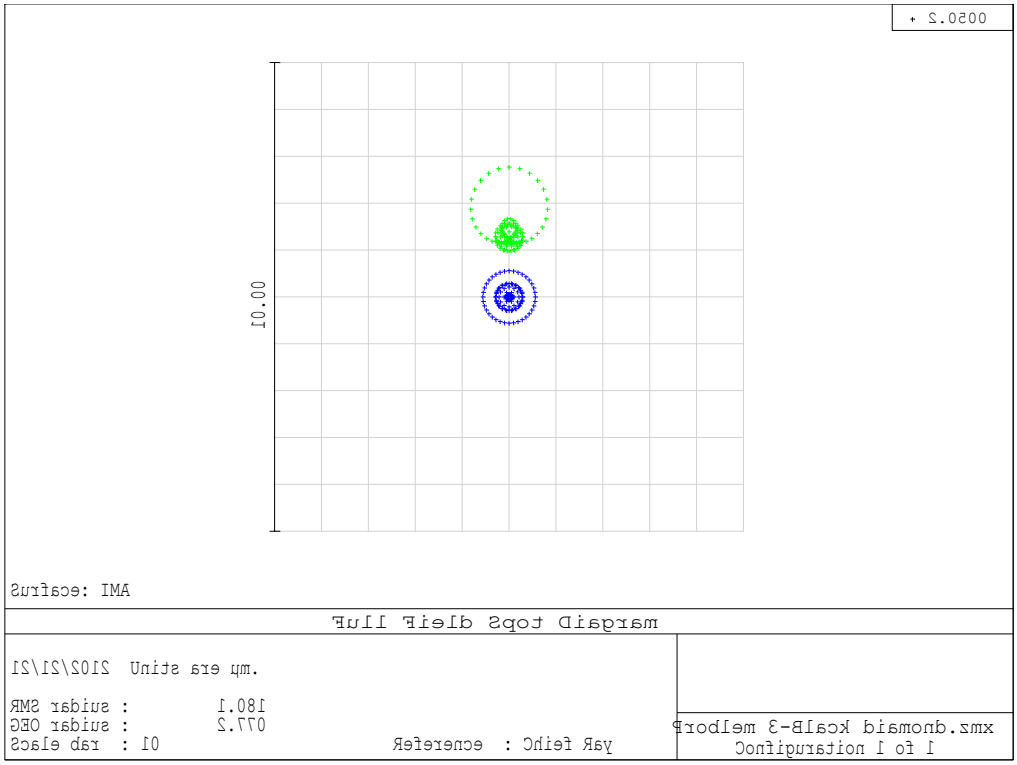

Figure 3.10 Full field spot size diagram

3.5.3 FTIR spectrum

The FTIR spectrum is shown in Figure 3.11, in which pump light at 1.55 μm and signal light at 2.05 μm are detected. However, there is no idler light coming from the output. In the circumstances, we have two hypotheses: phase-matching condition is not met and/or pump power is not large enough. We can simply buy a more powerful pump source to replace the current one. But it is essential to make sure the phase-matching condition is satisfied before that.

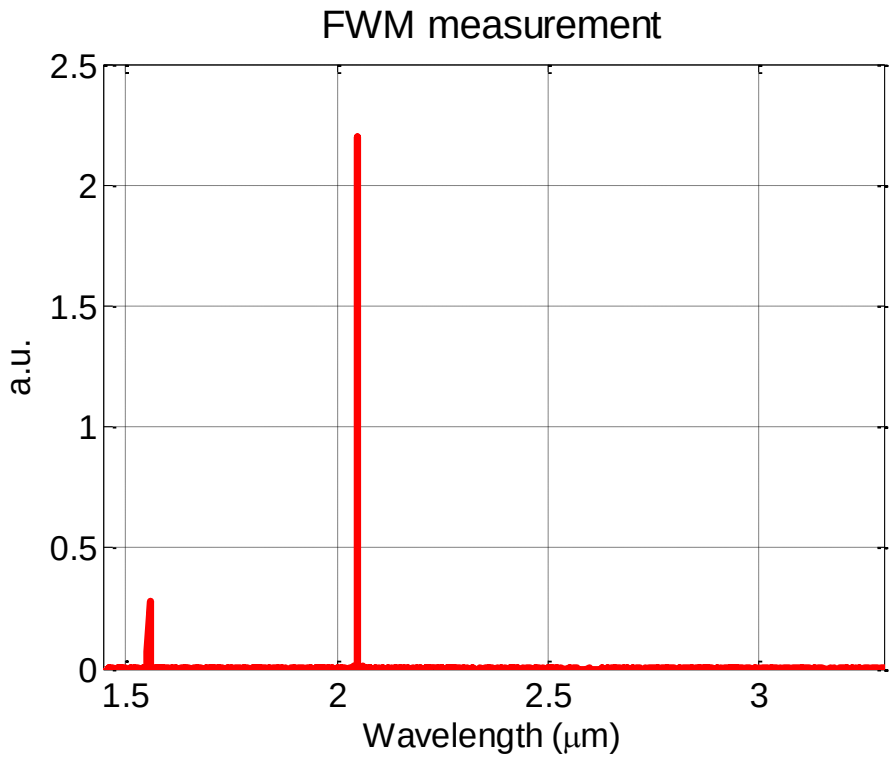

Figure 3.11 FWM measurement result

3.5.4 Parametric conversion efficiency degradation

As the key parameter of FWM, it is necessary to analyze its tolerance and the resulting degradation of parametric conversion efficiency. When pump power intensity is 0.1 GW/cm^2, the parametric conversion efficiency of FWM down-conversion design is -8 dB. The corresponding phase mismatch $\Delta\kappa$ is -2.261×10^{-6} /μm. When $\Delta\kappa$ is -6.784×10^{-5} /μm which is 30 times larger than the original value, the degradation of parametric conversion efficiency is 3 dB. When $\Delta\kappa$ is -9.498×10^{-5} /μm which is 42 times larger than the original value, the degradation of parametric conversion efficiency is 6 dB.

From the results above, it seems that the degradation of parametric conversion efficiency is acceptable. However, the conversion bandwidth can be impacted by small change of phase mismatch. In Figure 3.12, when phase mismatch is doubled or tripled, the 3-dB conversion bandwidth is largely shortened. Under the circumstances, if the center wavelength of signal light is slightly shifted, the parametric conversion efficiency will be decreased dramatically.

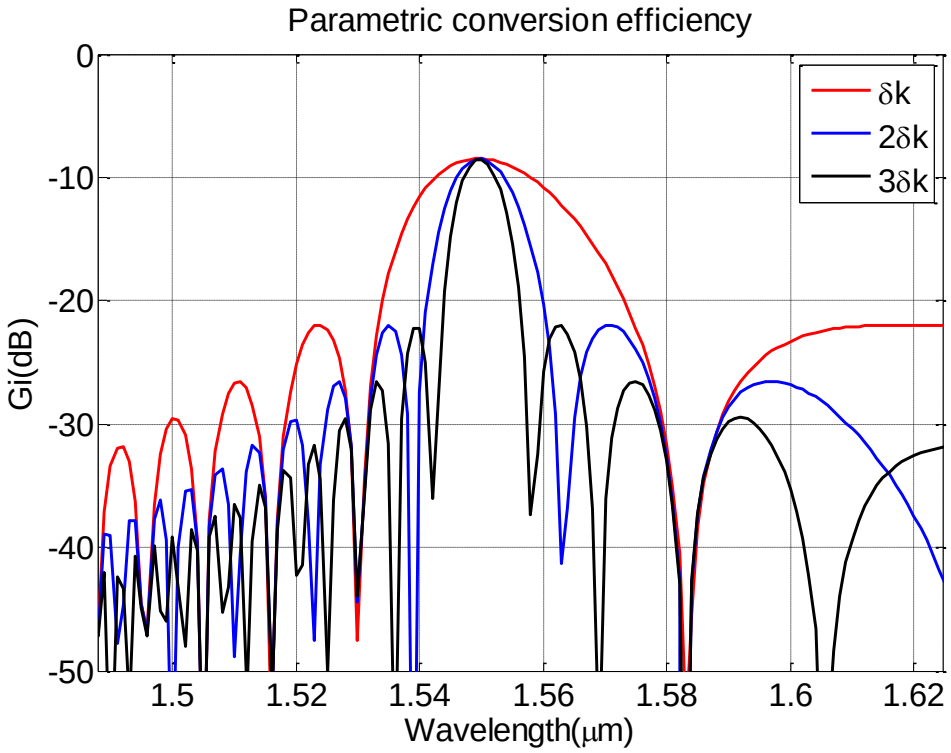

Figure 3.12 3-dB conversion bandwidth change with phase mismatch

Wavelength tuning technique is a good option to solved the problem. For signal wavelength, a broadband source like ASE can be used to overcome the wavelength shift issue. Due to the demanding requirement to pump power intensity, the pump source

must be a laser with a small FWHM. Our pump source is a thulium-doped DFB fiber laser centered at 2.05 μm with a FWHM of 1 nm. Since there are some variations in fabrication, it is desirable to have tunablity of the center wavelength to compensate any uncertainty from fabrication. Thermal tuning is a good option to achieve it. If we can communicate with the thermal electric cooler (TEC) in the laser, we will have ability to control the temperature of the DFB fiber laser. Based on [23], the thermal tuning coefficient is 40 pm/K. Piezoelectric tuning is another option, which has faster tunability than thermal tuning. However, the tuning coefficient is only 0.2 pm/V [23].

3.6 eSNR improvement by indirect detection of mid-IR

There are a wide variety of mid-IR applications in different fields, including environment, medicine and military. Mid-IR detectors are extremely limited in terms of operation condition, noise performance and speed [23]. Since low-noise and high-speed near-IR detectors are available, we can detect mid-IR wavelength by converting it to near-IR using FWM. At this point, our As_2S_3-on-$LiNbO_3$ waveguides can provide an excellent solution with high parametric conversion efficiency. Since detectors at near-IR wavelengths exhibit superior performances in speed, noise and sensitivity, the indirect detection scheme is promising to improve the detection performance [15].

In order to analyze the improvement in indirect detection, we calculate the noise performance in detection of 4.6 μm mid-IR signals by using PbSe and MCT mid-IR detectors and InGaAs photodetector following by an As_2S_3-on-$LiNbO_3$ wavelength converter, which has the same dimensions with the design with MgF_2 cladding on top.

Figure 3.13 illustrates the indirect detection of mid-IR signals converted to near-IR wavelengths by FWM and detected by near-IR detectors.

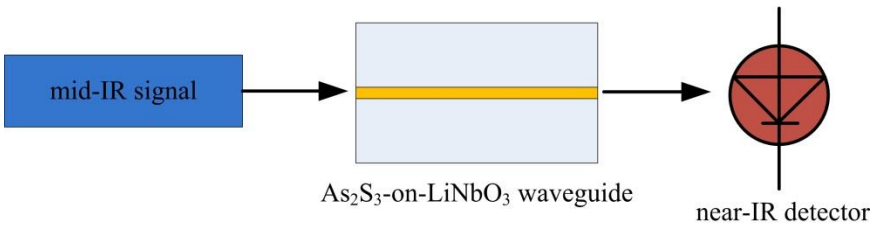

Figure 3.13 Schematic diagram of indirect mid-IR detection

3.6.1 Mid-IR signals up-conversion by FWM

In order to achieve high efficiency FWM, phase-matching condition has be satisfied. Figure 3.14 shows the phase mismatch curve for our As_2S_3-on-$LiNbO_3$ waveguide design, where As2S3 is 1.42 μm wide and 2.7 μm height with 0.089 μm MgF_2 cladding on top. Since the phase-matching condition is met at 1.32 μm, 4.6 μm and the region around the pump wavelength, which means that this design can provide high efficiency FWM process.

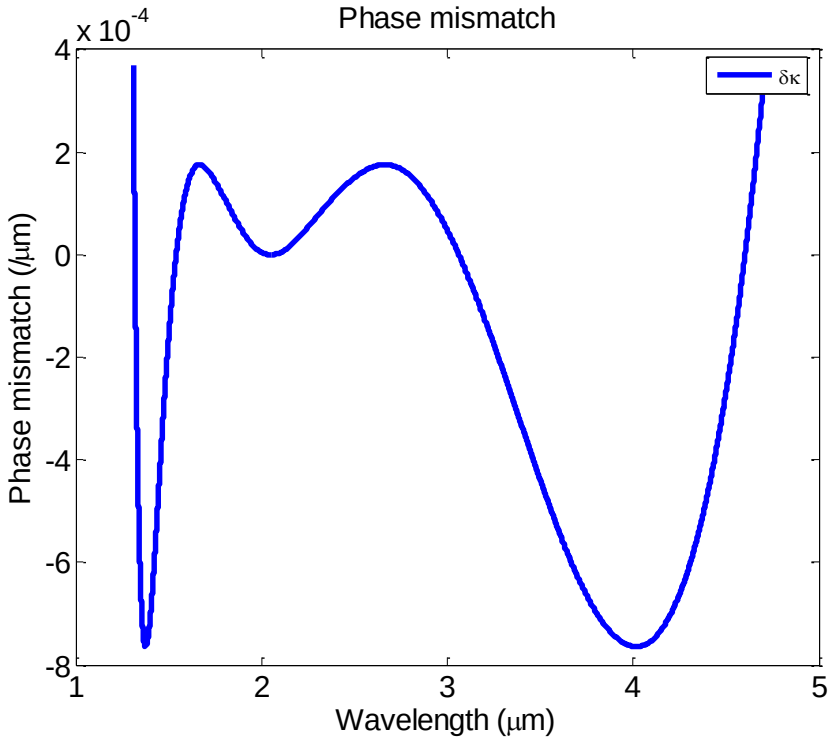

Figure 3.14 Phase mismatch

The parametric conversion efficiency G_i from equation (3.8) is shown in Figure 3.15. When L_{eff} is 4 cm and P_p is 1 GW/cm^2, the parametric conversion efficiency G_i is 16 dB. Since As_2S_3 glass is optically damaged at pump power densities larger than 80 GW/cm^2 [24], 1 GW/cm^2 will not damage our waveguides. The photosensitivity threshold from 0.8 to 1.3 GW/cm^2 [25] should also be mentioned, which may cause refractive index change of As_2S_3 waveguides. However, since our PVD technique can deposit As_2S_3 thin film that have the same molecular composition as bulk material, this photosensitivity is expected to be improved.

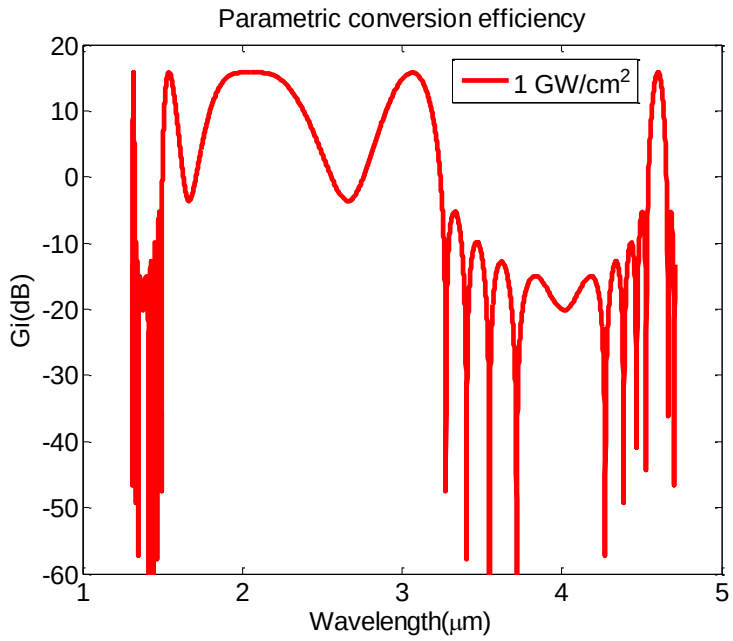

Figure 3.15 Parametric conversion efficiency

3.6.2 Analysis of InGaAs near-IR detector

Basically, there are two major types of noises in indirect detection associated with wavelength conversion, including pump transferred noise and quantum noise. Since the noise transfer from pump is considered to be detrimental for large signal powers [25, 26], it is negligible for weak mid-IR signals in our calculations. However, quantum noise should be considered in a parametric process like FWM and it will be transferred to $InGaA_S$ photodetector as quantum fluctuation, i_{qt}^2, described by equation (3.11) as below

$$\frac{i_{qt}^2}{B_e} = 4R^2 G_i P_{in} \frac{hc}{2\lambda}(2G_i + 1) \tag{3.11}$$

where h is Planck constant and c is speed of light. R is responsivity and B_e is the electrical bandwidth of InGaAs photodetector in the specification sheet. P_{in} is incident mid-IR signal power and G_i is parametric conversion efficiency, the same with equation

(3.8). Since weak mid-IR signal is considered, we use P_{in}=1 μW with 1 GW/cm^2 pump power.

Furthermore, there are some intrinsic noises from the detector itself, including thermal noise and shot noise. Thermal noise results from random thermal motion of electrons in a resistor manifests as a fluctuating current, which is described by equation (3.12)

$$\frac{i^2_{th}}{B_e} = 4(kT / R_L)F_n \tag{3.12}$$

where k is Boltzmann constant, T is operating temperature, R_L is load resistance and F_n is circuitry noise figure. Shot noise is a manifestation of the fact that an electric current consists of a stream of electrons that are generated at random times, shown is equation (3.13)

$$\frac{i^2_{sh}}{B_e} = 2q(RG_iP_{in} + i_d) \tag{3.13}$$

where q is elementary charge and i_d is dark current. Since the noise components are characterized, we can simply calculate the noises for indirect detection of mid-IR signals. The parameters used in our calculation are shown in Table 2, which comes from state-of-the-art commercial near-IR and mid-IR detectors in [23] and [27].

Table 2. Detector specifications

	λ(μm)	T(K)	R	$R_L(\Omega)$	i_d(pA)
InGaAs	1.55	300	0.95A/W	8M	80
PbSe	3.03	300	3×10^3V/W	0.3M	NA
MCT	3.03	300	3×10^3V/W	1.5k	NA

Figure 3.16 demonstrates that the noise from InGaAs photodetector at near-IR by FWM at room temperature with incident power of 1 μW. It is obvious that the eSNR of the detector is limited by shot noise at low pump power intensities. However, when pump power intensity increases over 0.25 GW/cm^2, the parametric conversion efficiency increases and therefore, the quantum noise becomes dominant. At room temperature, thermal noise is little and it can be further improved by cooling of near-IR detector in indirect detection process using TEC.

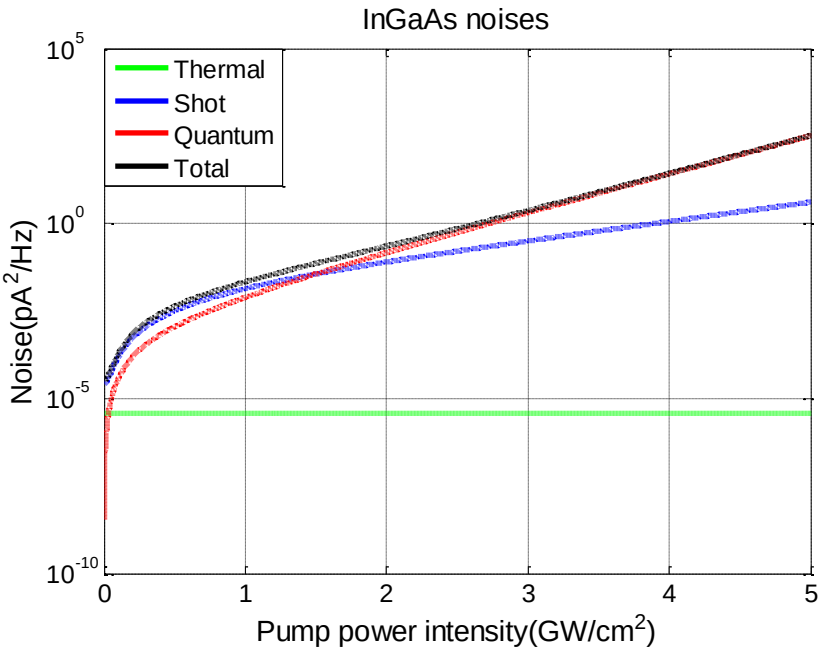

Figure 3.16 InGaAs noise at near-IR for indirect detection

3.6.3 Analysis of PbSe and MCT mid-IR detectors

Since the noise performance of the near-IR detector is well demonstrated, in order to make comparison for eSNR, it is essential to characterize the mid-IR detectors. There are three types of commercial mid-IR detectors: thermal detectors, photovoltaic (PV) and photoconductive (PC) detectors. Thermal detectors are based on the resistance change by incident mid-IR signals. They have low sensitivity and are also too slow for real-time detection. The operational principle of PV detectors is generating current by absorption of photons with energy beyond their bandgap. Due to the narrow bandgap of mid-IR photons, the excess thermal generation during the detection will lead to considerable dark current and then large shot noise. It is necessary to operate them at low temperature (~70K) to reduce dark current. In other words, PV detectors are limited

by its shot noise level at room temperature. Therefore, only PC detectors are characterized here.

In terms of PC detectors, the voltage change is measured, which results from the conductivity change of the medium by photo-induced carriers. The major noise components of PC detectors include thermal noise, background noise, generation-recombination (G-R) noise and flicker noise. Since a low-pass filter can be used in the system to eliminate flicker noise, the total noise will consist of thermal noise, background noise and G-R noise. As above, Thermal noise is described in equation (3.12). Background noise is shown in equation (3.14)

$$\frac{i^2_{bg}}{B_e} = q^2 \eta A E_B \tag{3.14}$$

where η is quantum efficiency and A is active detector area. Photon flux density E_B is described in equation (3.15)

$$E_B = \int_0^{\lambda_c} \varepsilon_\lambda \frac{2\pi c}{\lambda^4} [\frac{1}{e^{hc/\lambda kT} - 1}] d\lambda \tag{3.15}$$

where ε_λ is emissivity for the medium material and λ_c is cut-off wavelength.

G-R noise is denoted in equation (3.16)

$$i^2_{GR} = \frac{2qI_0\Gamma_G}{\pi\tau} \tan^{-1}(2\pi B_e \tau) \tag{3.16}$$

where τ is the average carrier lifetime. I_0 is the total generation current. Γ_G is the current gain.

Currently, there are two kinds of commercial PC detectors: PbSe and MCT detectors. In view of relative slow response of mid-IR detectors, a 0.1MHz electrical

bandwidth is used. Based on the calculations, thermal noise is dominant in PbSe and MCT detectors. For the same 1 μW incident power at mid-IR, the total noise of PbSe and MCT detectors are 0.01pA^2/Hz and 16.73pA^2/Hz, respectively.

3.6.4 eSNR improvement

The eSNR improvement is defined by comparing the eSNR of InGaAs photodetector to those of PbSe and MCT mid-IR photodetectors, as described by equation (3.17)

$$eSNR_{near\text{-}IR} / eSNR_{mid\text{-}IR} \tag{3.17}$$

In order to analyze eSNR enhancement by indirect detection to weak mid-IR signals, we used different input power levels at 0.1 μW, 1 μW and 10 μW in calculations to estimate the detection limit, as presented in Figure 3.17. Under the same incident power level, the eSNR improvement with respect to PbSe detectors is larger than that with respect to MCT detectors. When the input mid-IR power is 0.1 μW, the largest eSNR improvement is achieved with respect to both PbSe and MCT detectors, which are 67 dB and 32 dB, respectively. In addition, compared to different incident power levels, indirect detection is more advantageous at lower input levels.

It is obvious that the eSNR enhancement increases with the increasing pump power intensity until it reaches 1 GW/cm^2, at which eSNR enhancement saturates resulting from the limit of quantum noise to FWM process. The phenomenon indicates that although the parametric conversion efficiency increases with the increasing pump power intensity, it is cancelled out by the increasing quantum noise. Furthermore, if we don't use TEC system, power radiation will increase thermal noise by heating the

medium material. In this case, the pump power is supposed to be controlled in a proper range. Therefore, the maximized eSNR enhancement can be achieved.

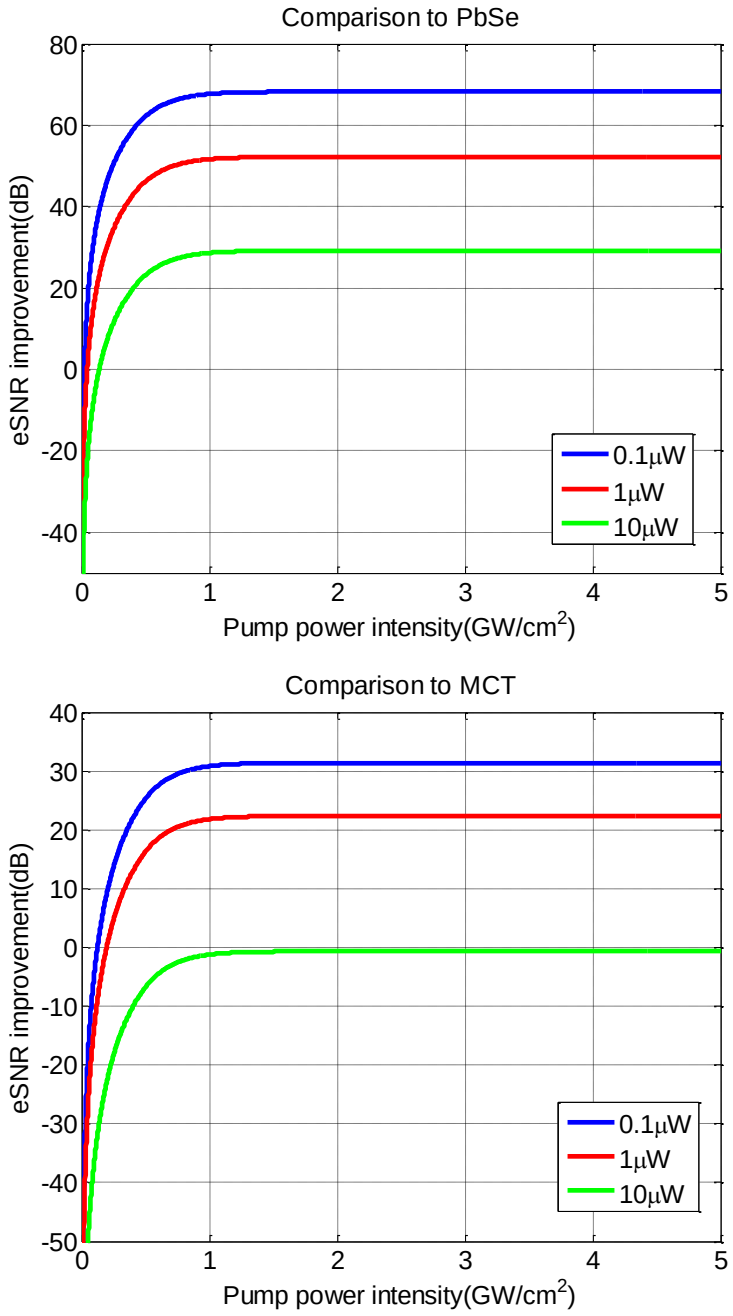

Figure 3.17 eSNR enhancement compared to (a) PbSe; (b) MCT detectors

In summary, in the first part of this chapter, we demonstrate mid-IR FWM simulations for As_2S_3 waveguides, which can generate 3.03 μm mid-IR light by a 1.55 μm near-IR signal source and a strong 2.05 μm pump source. The FWM phase-matching efficiency at 1.55 μm is up to 100 % for the designs with and without MgF_2 cladding on top of As_2S_3 core. For 0.1 GW/cm^2 pump power intensity, the largest parametric conversion efficiency at 3.03 μm is -8 dB, which is 20 dB larger than the result in silicon waveguides in [14]. The largest conversion bandwidth of 1525 nm is achieved when the waveguide length is 1 cm. In addition, we simulated the 100 % FWM phase-matching efficiency shift for diverse fabrication variations.

In the second part, on the contrary, the same FWM process is used to convert mid-IR signal back to near-IR and the eSNR improvement in indirect detection of mid-IR signals in As_2S_3 waveguides is illustrated. Our calculations show that the eSNR enhancement by phase-matched As_2S_3 waveguides is 17 dB larger the result in silicon waveguides in [15]. Please refer to appendices for details.

CHAPTER IV

FABRICATION AND PROCESS DEVELOPMENT

This chapter mainly discusses the fabrication processes of As_2S_3-on-$LiNbO_3$ waveguides as well as new ideas to further improve the waveguide quality by sample bonding, shown in Figure 4.1. The expectations to future semiconductor manufacturing techniques are also summarized.

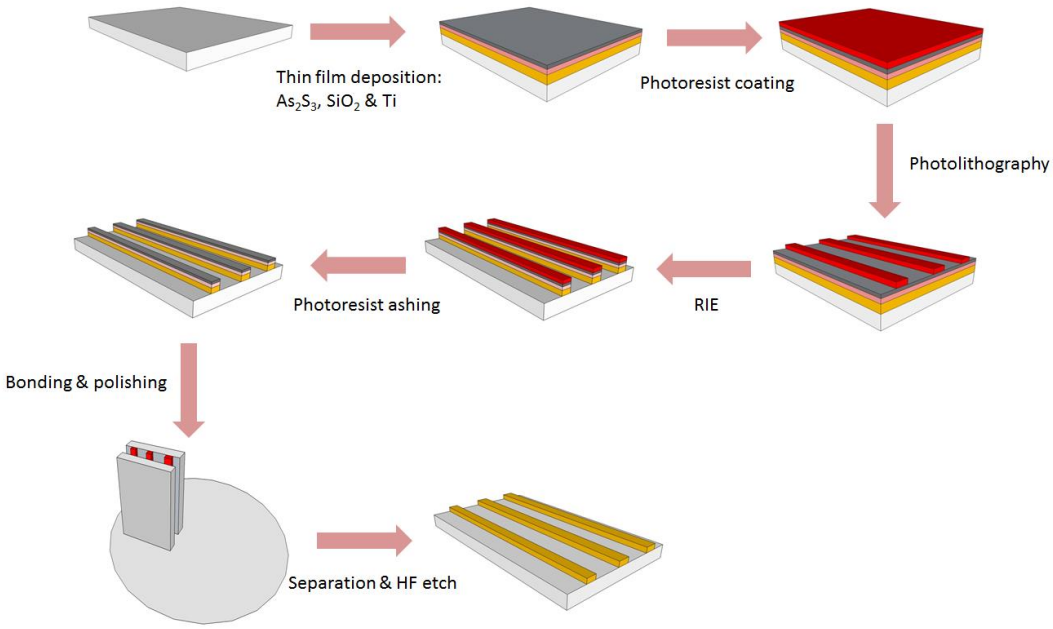

Figure 4.1 Fabrication processes of As_2S_3-on-$LiNbO_3$ waveguides

4.1 Substrate preparation

In the beginning, a 3-inch wide and 1mm thick $LiNbO_3$ wafer is diced into square samples. Based on our demand, the $LiNbO_3$ wafer is in x-cut, y-propagation. It can also be in y-cut, z-propagation for some special devices. Although we call them "square

samples", in order to distinguish the crystal manner in the following fabrication processes, the sample size is 22.5 mm by 20.5 mm.

After dicing, $LiNbO_3$ samples are pre-cleaned consecutively by soapy water, acetone, methanol and isopropyl alcohol (IPA). Soapy water can remove the oil from dicing machine. Acetone is typically used for cleaning purpose in the laboratory. Methanol, a widely-used solvent for cleaning electronic devices, is able to dissolving a large number of non-polar chemical compounds. IPA rinsing is the last step because it can remove methanol.

4.2 Thin film deposition

After pre-cleaning, $LiNbO_3$ samples are loaded into a magnetron sputtering system (ATC 2000 by AJA Intl Inc., shown in Figure 4.2) to deposit As_2S_3 film, silicon dioxide (SiO_2) and titanium (Ti). Since As_2S_3 will be dissolved by our developers MF 312 and MF 319, it is necessary to have SiO_2 and Ti on top of it as the protective layers. Based on the design in last chapter, the As_2S_3 thickness is 1.7 μm. 150 nm SiO_2 and 20 nm Ti are thick enough to protect As_2S_3 from being dissolved by developer. As_2S_3 and SiO_2 are deposited at 1.5 mTorr with 35 sccm Ar flowing and RF power of 35W. As a metal, Ti is deposited with DC power.

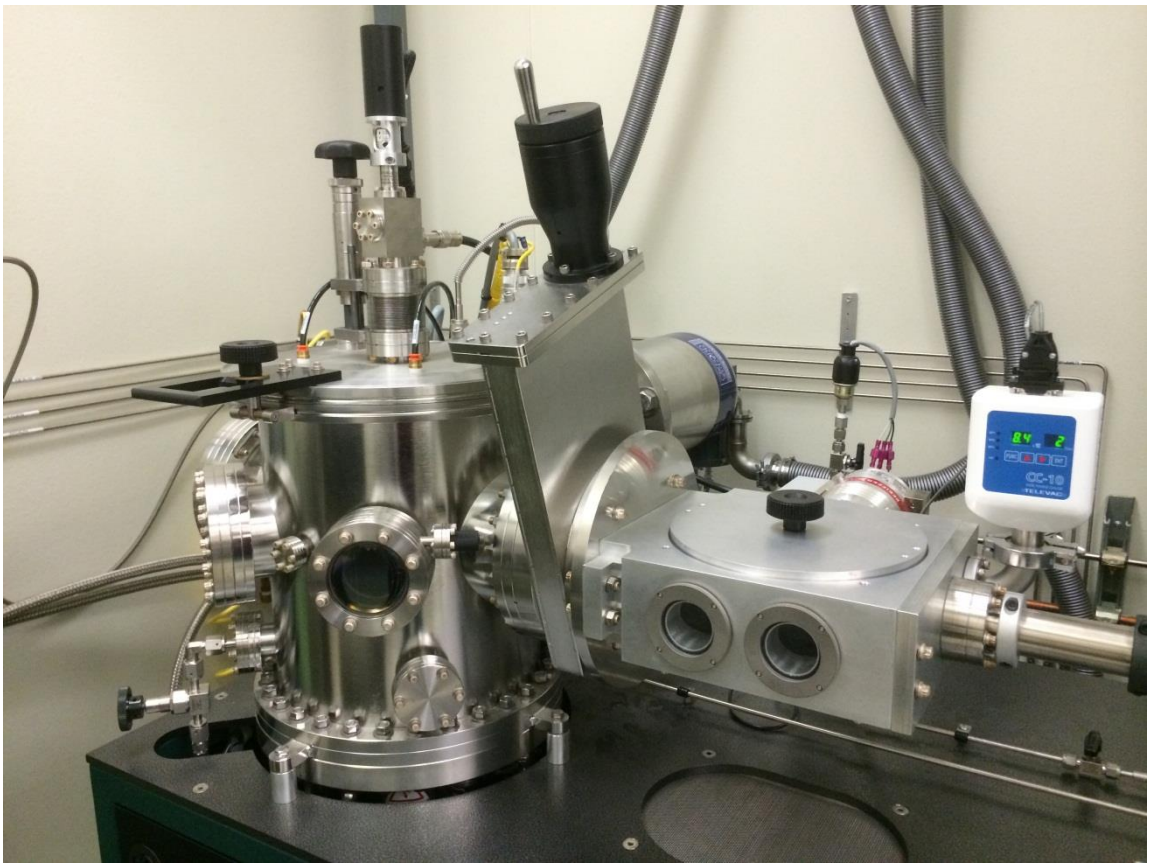

Figure 4.2 AJA magnetron sputtering system

Since the As_2S_3 film is thick, it is important to monitor its thickness by adding some silicon dummies and measure them multiple times during the deposition process. The thickness is measured by Filmetrics F20, a reflective spectroscopic tool with a broadband white light source form 400 nm to 3000 nm. Since birefringence material cannot be easily measured by Filmetrics, it is the reason that we use silicon dummies instead of $LiNbO_3$ dummies for thickness mesurement. In order to get accurate results, it is essential to measure bare Si wafer as the reference prior to As_2S_3 thickness measurement. The principle of Filmetrics is to measure the interferogram generated by the reflected lights from As_2S_3 surface and substrate surface. As_2S_3 thickness, which is

also the optical path length difference, is determined by analyzing the interferogram and comparing to the reference.

4.3 Photolithography

Photolithography is used to transfer patterns from the photo mask to our samples. In preparation, AZ 5214, a widely-used positive photoresist is coated on the sample by spinning coating at 7000 RPM for 40 seconds with 5 seconds acceleration/deceleration. In order to minimize solvent concentration in photoresist, the sample is baked at 125 ℃ for 1 minute on a hotplate immediately after spinning coating. We use MA 6 (Figure 4.3), an I-line contact aligner, to pattern the sample. The exposure window is a 3 inch by 3 inch square area. For the sake of best image contrast, the total dose is supposed to be 95 mJ/cm^2. Since the exposure intensity is slightly vibrating time by time, the exposure time is dependent on the intensity that we measure before exposure. For instance, if the intensity is 5 mJ/cm^2, our exposure time should be 19 seconds. The sample is aligned to the mask by microscope. It is necessary to make waveguides parallel to sample edge. After patterning, the sample is soaked into diluted MF 312 solution (1:1.2) or pure MF 319 to develop for approximate 45 seconds (until the pattern shows up and no more photoresist in the corners). The sample is inspected by microscope under 500x or 1000x magnification. We focus on developing markers and surface contamination to determine if the sample is qualified to next step. If the sample surface is clean and the markers shows that it is well-developed, we bake the sample at 135 ℃ for 30 minutes to harden the photoresist so it will be a mask for etching process later. If not, the photoresist will be removed by acetone and the sample will be patterned again after thorough cleaning.

Figure 4.3 MA 6 I-line contact aligner

4.4 Reactive ion-etching and oxygen ashing

Smooth waveguide surface and vertical sidewalls can be achieved by plasma etching. In our fabrication processes, reactive ion-etching (RIE) is used. As a type of plasma etching, RIE removes materials by chemically reactive plasma and ion bombardment. Our etchants are CHF_3 and Argon (Ar), in which CHF_3 removes materials by chemical reaction and Argon does that by physical ion bombardment. The RIE tool shows in Figure 4.4, in which both RF and inductively coupled plasmas (ICP) power are needed to get high etch rate with slight surface damage. Since volatile species are created by chemical reaction and then ion bombardment dislodges them, CHF_3 and Ar

are a good combination. In addition, during RIE process, a passivation layer is formed on sidewalls to maintain vertical etching. Usually the total etching time is approximate 5 minutes. However, we split it into 2~3 time segments to make sure that the sample is not over-etched.

Figure 4.4 RIE tool from Oxford

It is noticeable that both RIE tool and AJA magnetron sputtering system is load-locked, which means that the chambers are always in low pressure (10^{-7} mTorr or less). When loading or unloading the sample, we only need to vent and evaporate the load lock, which can save a plenty of time for the cycle. If we have to open the chamber and then

load the sample inside of it, usually it takes more than 24 hours to evaporate the chamber to working pressure because the air molecules are diffused into chamber wall.

After RIE, the photoresist is removed by oxygen (O_2) ashing. Since photoresist has been hard-baked by 30 minutes at high temperature, it takes 9 minutes to remove all of it on top of the waveguides by ashing. As O_2 cannot react with $LiNbO_3$ and there is no inert gas in the etchant, substrate damage is not an issue. We only need to make sure that all the photoresist is removed during this process. Furthermore, oxygen ashing can remove the polymer on sidewalls, which is deposited by RIE process.

4.5 Bonding, polishing and wet etching

After RIE and ashing, both end-faces of the sample should be polished to optical quality to minimize the coupling loss for testing. Since As_2S_3 is a brittle material, it is essential to protect the sample surface during polishing process. Previously, two samples were bonded face to face with wax and then were polished together. However, due to the abrasive force between the sample and polishing pad, waveguides on the sample in the front tend to be peeled off largely. Right now, in order to prevent this scenario, the sample is bonded with a bare $LiNbO_3$ sample (as a sacrificial sample) instead of a real sample with waveguides on it. We have three different polishing pads with different roughness. 10 μm pad is used to remove the unpatterned region on the edges. 3 μm one can make the end-faces optical quality. 0.1 μm pad is for fine polishing in last step. Finally, when polishing is finished, the samples are separated and protective layers (SiO_2 and Ti) are removed by hydrogen fluoride (HF) solution (1:30). Figure 4.5 shows pictures of good As_2S_3-on-$LiNbO_3$ waveguides.

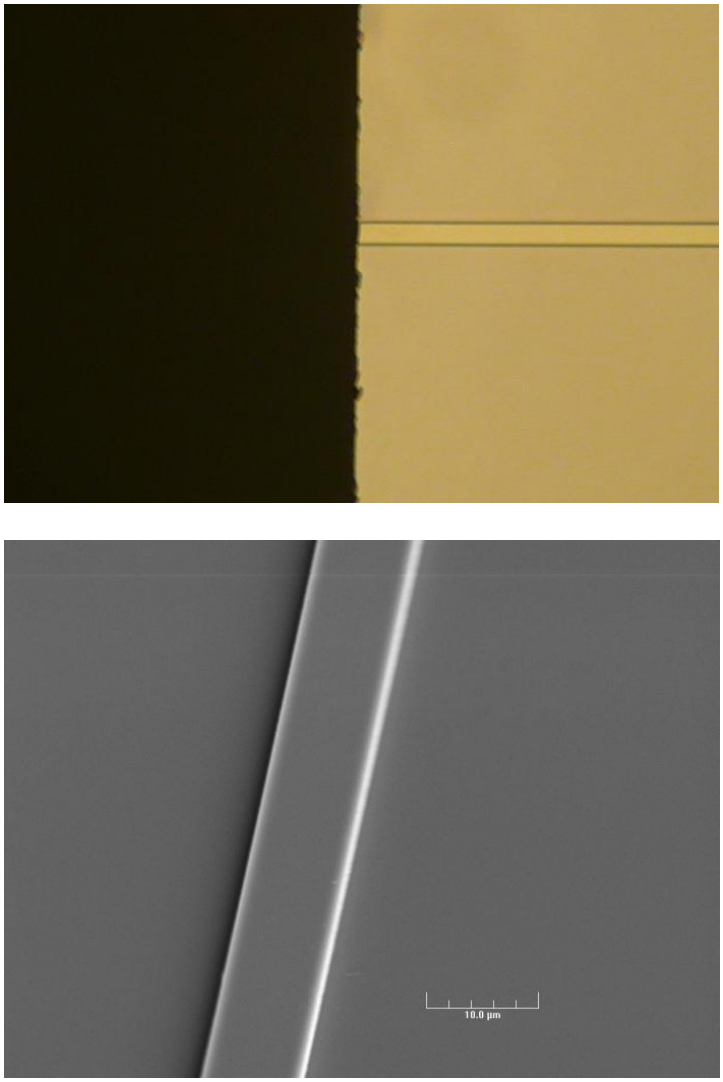

Figure 4.5 (a) Top view; (b) SEM image [17] of As_2S_3-on-$LiNbO_3$ waveguide

CHAPTER V

MEASUREMENTS AND RESULTS

This chapter discusses optical low-coherence interferometry (OLCI), which uses a broadband source and an interferometer to obtain a fringe pattern by varying optical path length difference (OPD) between two paths. When the fringe pattern is Fourier transformed, the spectral density of the source is obtained [28]. As the basic model of OLCI, Michelson interferometer is also included.

5.1 Michelson interferometer

Michelson interferometer, a widely used configuration for optical interferometry, was invented by Albert Abraham Michelson. A fringe pattern is generated by splitting a beam of light into two paths, reflecting the beams by mirrors and recombining them. The OPD creates interference fringes on the detector.

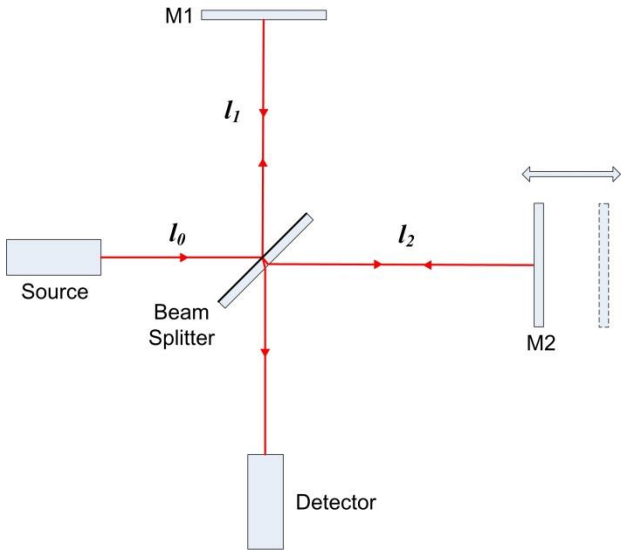

Figure 5.1 Path of light in Michelson interferometer

Figure 5.1 shows path of light in Michelson interferometer. A Gaussian beam of light coming from the source is splitter into two paths by a 50/50 beam splitter, which has semi-reflective coating on the front surface. The vertical beam is undergoing two front-surface reflections at the beam splitter and mirror M1, respectively. The phase change is 2π, shown in equation (5.1). The horizontal beam is undergoing a front-surface reflection at moving mirror M2, and a rear-surface reflection at the beam splitter, respectively. The phase change is 2π, shown in equation (5.2)

$$E_1 = \frac{1}{\sqrt{2}} E_0 e^{j[\omega t - k(l_0 + 2l_1) + \varphi_0 + 2\pi]} \tag{5.1}$$

$$E_2 = \frac{1}{\sqrt{2}} E_0 e^{j[\omega t - k(l_0 + 2l_2) + \varphi_0 + 2\pi]} \tag{5.2}$$

where E_0 is the amplitude. ω is the angular frequency. $k=2\pi n/\lambda$ is the wave vector. r is the position vector. φ_0 is the initial phase. l_0, l_1 and l_2 are physical distances between source and beam splitter, beam splitter and M1, beam splitter and M2, respectively.

Mirror M2 is installed on a motorized translation stage, which can vary the OPD between two beams. In order to generate fringe pattern, the OPD has to be within a coherence length of the source, which demonstrates in equation (5.3)

$$Lc = \frac{0.88\lambda^2}{n\Delta\lambda} \tag{5.3}$$

where n is the refractive index. λ and $\Delta\lambda$ are central wavelength and FWHM of the source, respectively. If the condition is satisfied, the fringe pattern is observed by the detector after the recombination of two beams of light at the rear surface of beam splitter as follows

$$
\begin{aligned}
I &= \left|E_1 + E_2\right|^2 \\
&= \left|\frac{1}{2}E_0 e^{j[\omega t - k(l_0+2l_1)+\varphi_0+2\pi]} + \frac{1}{2}E_0 e^{j[\omega t - k(l_0+2l_2)+\varphi_0+2\pi]}\right|^2 \\
&= \frac{1}{4}{E_0}^2\{2+2\cos[\omega t - k(l_0+2l_1)+\varphi_0+2\pi] - [\omega t - k(l_0+2l_2)+\varphi_0+2\pi]\} \qquad (5.4) \\
&= \frac{1}{2}{E_0}^2[1+\cos(2k\Delta l)] \\
&= \frac{1}{2}{E_0}^2[1+\cos(\frac{4\pi n}{\lambda}\Delta l)]
\end{aligned}
$$

where I is the intensity of the fringe pattern. $\Delta l = l_1 - l_2$.

Broadband source only has a limited coherence length. When using it, the two optical paths must be approximately equal for all output wavelengths. To meet this requirement, both the vertical and horizontal light paths must cross an equal thickness of beam splitter. In Figure 5.2, the vertical beam crosses the beam splitter one time, while the horizontal beam crosses the beam splitter three times. To equalize the optical path lengths, a compensating plate identical to the beam splitter, but without the semi-reflective coating, is inserted into the path of the vertical beam.

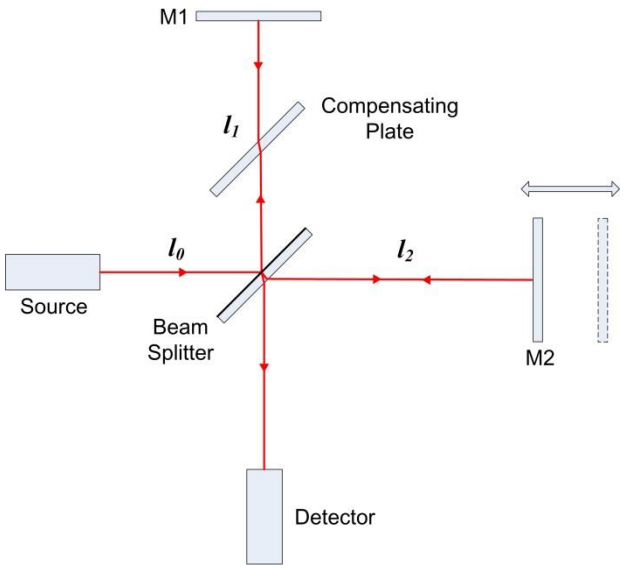

Figure 5.2 Michelson interferometer with compensating plate

5.2 Optical low-coherence interferometry

Optical low-coherence interferometry (OLCI) uses a broadband source and an interferometer to obtain a fringe pattern by varying the OPD between two paths. When the fringe pattern is Fourier transformed, the spectral density of the source is obtained [28]. Based upon Fourier spectroscopy, the frequency response of a DUT can be achieved by placing DUT in one arm of an interferometer. Meanwhile, the phase of DUT can also be extracted, which gives us the ability to get group delay of DUT by differentiation.

The schematic diagram of our OLCI measurement setup is shown in Figure 5.3. In the first place, an amplified spontaneous emission (ASE) with a several-nanometer bandwidth is used as the source, in which the spectrum is from 1520 nm to 1570 nm. It is generated by spontaneous emission by a 980 nm pump laser. An isolator is used to protect ASE source from reflective beam. In the second place, the light is split into two

paths by a 2x2 3-dB optical fiber coupler. In the reference arm (the path without DUT), the beam is coupled from optical fiber to free space by a fixed collimator and then coupled back to optical fiber again by an collimator that sits on a motorized translation stage, which is able to adjust the optical path length of reference arm to match that of DUT arm within the coherence length of ASE source. In the third place, the two beams are recombined by a 2x1 3-dB optical fiber coupler.

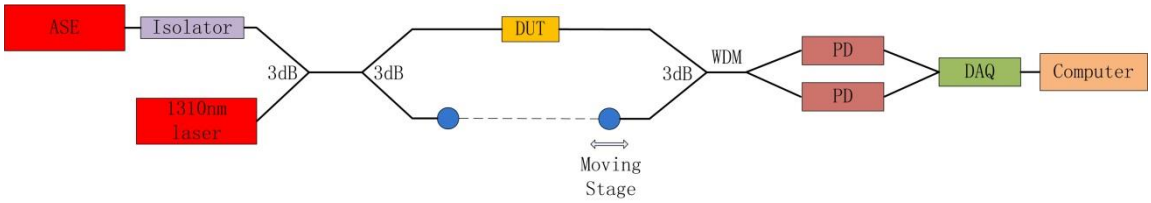

Figure 5.3 Schematic diagram of OLCI measurement setup

The interference of the two beams can be denoted by equation (5.5)

$$I_v(\tau) = \frac{|A(f)|^2}{4}\{1 + |A(f)|^2 + 2A(f)\cos[\varphi(f) - 2\pi f\tau]\} \tag{5.5}$$

where *A(f)* is the spectral density of ASE source. *φ(f)* is the phase response of the DUT. $\tau = x/c$. The fringe pattern can be described by integrating over the frequency content and neglecting "DC" terms.

$$I(\tau) = \frac{1}{2}\int_0^\infty |A(f)|^2 A(f)\cos[\varphi(f) - 2\pi f\tau]df \tag{5.6}$$

Meanwhile, although the motorized translation stage is controlled by software and we can set the motion at a constant speed, the mechanical accuracy is not high enough to get the fringe pattern with equal increment of OPD. As displayed in Figure 5.4, since its speed is not always constant, it is necessary to have a "clock", which is a 1310

nm laser in our measurement system. It is obvious that the fringe pattern of the laser will be generated easily due to its large coherence length. Therefore, if the OPD of two arms is within the coherence of ASE source, we can get fringe patterns for both ASE source and 1310 nm laser by moving the motorized translation stage.

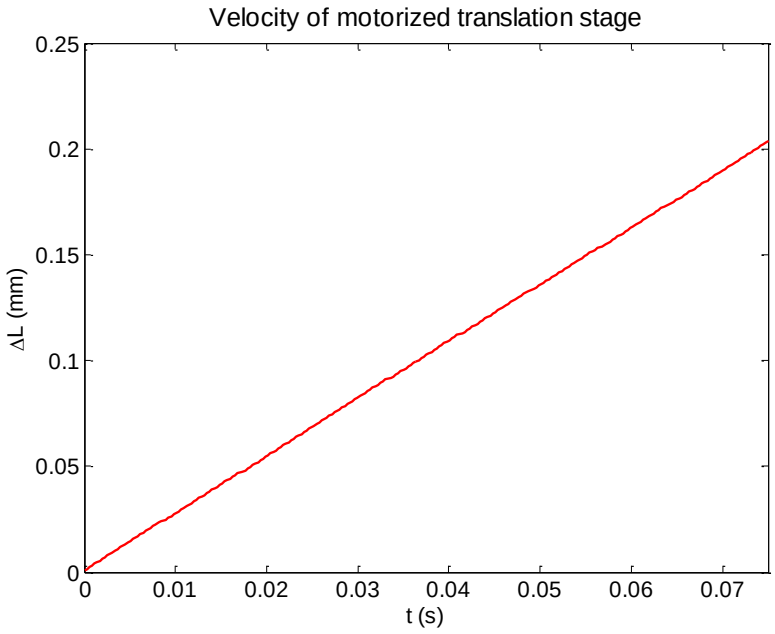

Figure 5.4 OPD change with time

In order to detect the two fringe patterns without crosstalk, a wavelength-division multiplexing (WDM) is connected to the 2x1 3-dB optical fiber coupler, which is able to separate ASE wavelength and laser wavelength and sent them into different photodiodes. An InGaAs photodiode with measurement range from 700nm to 1800nm is used to detect ASE beam. Since its amplification is tunable from 0 to 70 dB, it can largely improve SNR at high amplification levels. A PbSe photodiode with measurement range from 1.5 μm to 4.8 μm is used to detect 1310 nm laser beam. Both photodiodes convert

optical signals to electrical signals for detection and then send electrical signal to a data acquisition (DAQ) board from National Instruments, which can be read by a Labview program in the computer, shown in Figure 5.5.

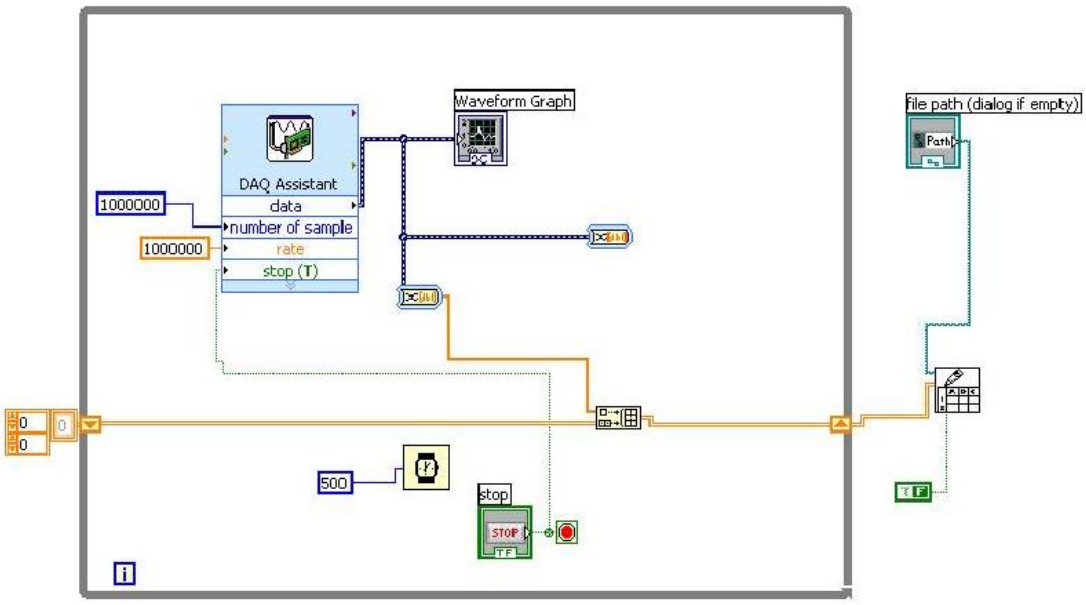

Figure 5.5 Labview program for OLCI measurement

5.2.1 Fourier transform of fringe pattern

The motorized translation stage we use, MTS50-Z8 has a dual set of linear rails with continuously recirculating ball bearings on a moveable carriage. Ideally, the motorized translation stage is supposed to provide linear motion at a constant speed in one dimension. However, since the accuracy of mechanical tool is not high enough to satisfy our requirement, a laser centered at 1310 nm is used as a clock to sample the fringe pattern and then the DUT spectrum can be extracted by fast Fourier transform (FFT).

It is significant to verify the method and the measurement setup before getting started on DUT measurement. Figure 5.6 and Figure 5.7 demonstrate our test setup, in which both two arms are reference arms. Therefore, one fringe pattern measured by Labview is the interferogram of two beams coming from ASE source. The other fringe pattern is from two laser beams. After sampling ASE fringe pattern by laser fringe pattern, new interferogram of ASE source is converted to the spectrum by FFT. The OLCI measurement system can be verified by comparing it to the spectrum measured by high resolution optical spectrum analyzer (OSA).

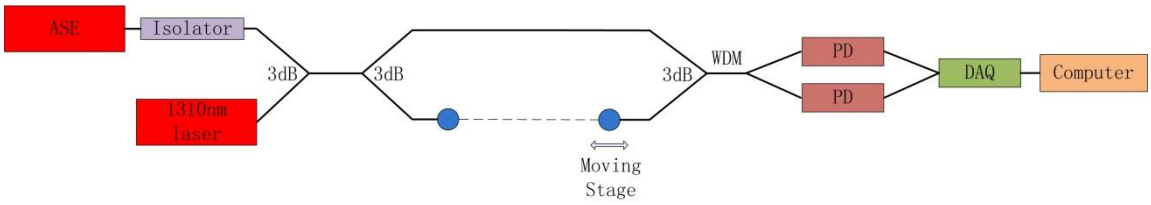

Figure 5.6 Schematic diagram of OLCI test setup

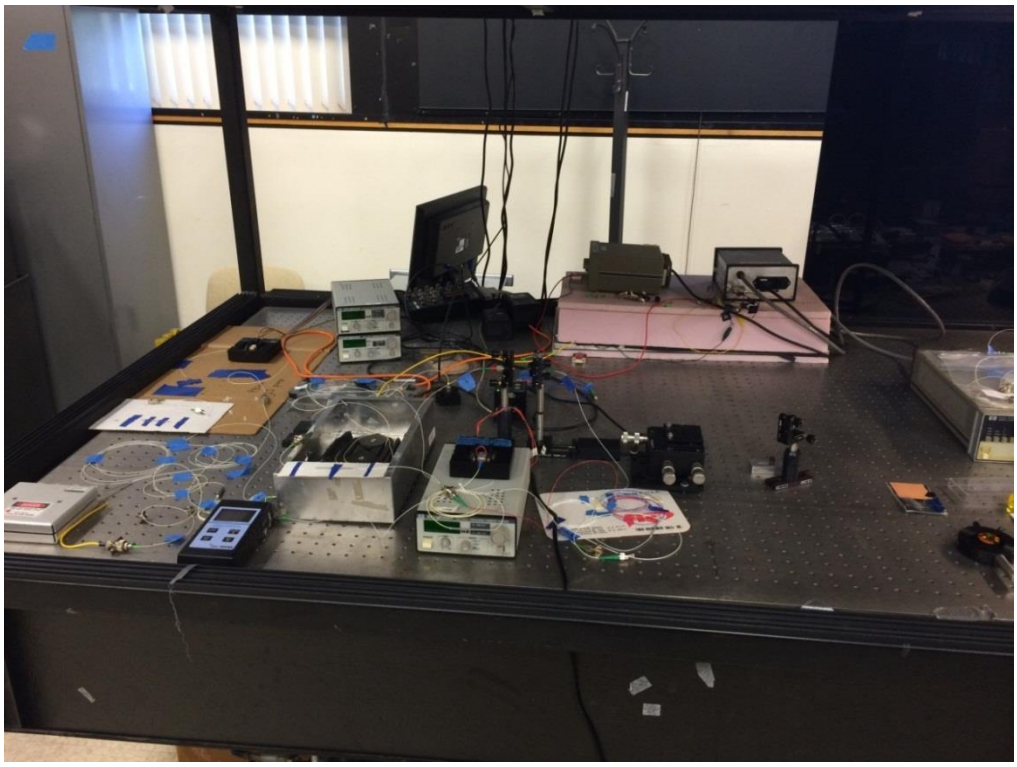

Figure 5.7 OLCI measurement system

The minimum sampling rate has to satisfy Nyquist sampling criterion, which indicates that the largest spatial sampling interval for the fringe pattern is related to the shortest source wavelength as follows

$$\Delta x_{\max} = \frac{\lambda_{\min}}{2n} \tag{5.7}$$

where n=1 is the refractive index of air. Since the minimum wavelength of ASE source is 1520 nm, the largest spatial sampling interval is 760 nm. It is well known from equation (5.4) that OPD between peak and valley values in the fringe pattern is $\lambda/2$, where λ is center wavelength of 1310 nm laser. As a result, our spatial sampling interval is 655 nm, which is smaller than 760 nm. Therefore, Nyquist sampling criterion is met.

The fringe patterns measured by Labview program are shown in Figure 5.7, in which pink curve stands for the fringe pattern of the laser while white curve stands for the fringe pattern of ASE source. All the “DC” terms are filtered out by setting the DAQ board to read “AC” signals. The x-axis is time and y-axis is magnitude. Apparently, the coherence length of the laser is much larger than that of ASE source. After that, it is necessary to convert x-axis of ASE fringe from time to OPD by sampling it using laser fringe pattern. The data processing is done by Matlab.

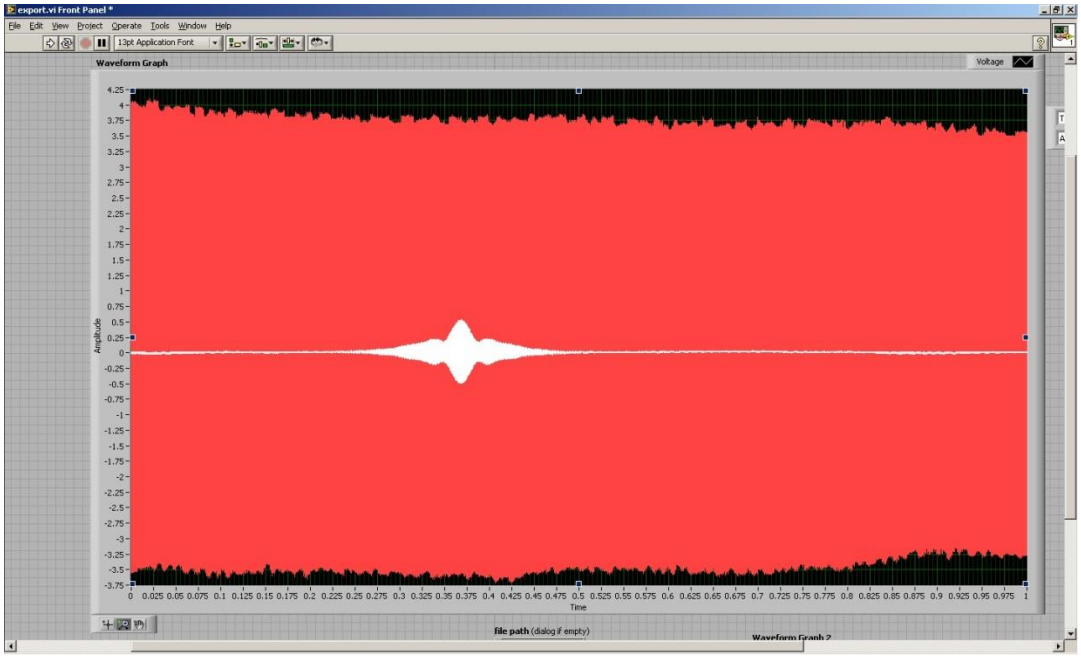

Figure 5.8 Fringe patterns measured by Labview

Since the motion of the motorized translation stage is not always linear and the fringe pattern of the laser is subject to this limit, it is essential to do data processing using a filter. Sgolay filter is used, which can eliminate the distortion of the fringe pattern with minimum change (in Figure 5.9). The normalized fringe pattern with OPD

is shown in Figure 5.10. When OPD is 0, the fringe pattern has the largest amplitude and it decreases with the increasing OPD. The fringe pattern disappears when OPD is larger than coherence length of ASE source.

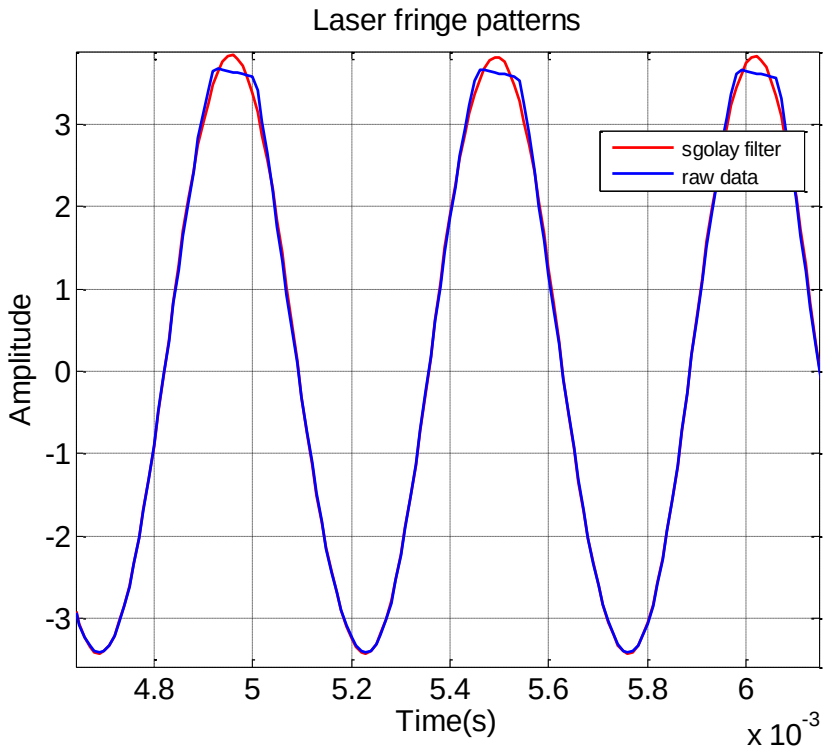

Figure 5.9 Laser fringe patterns with and without sgolay filter

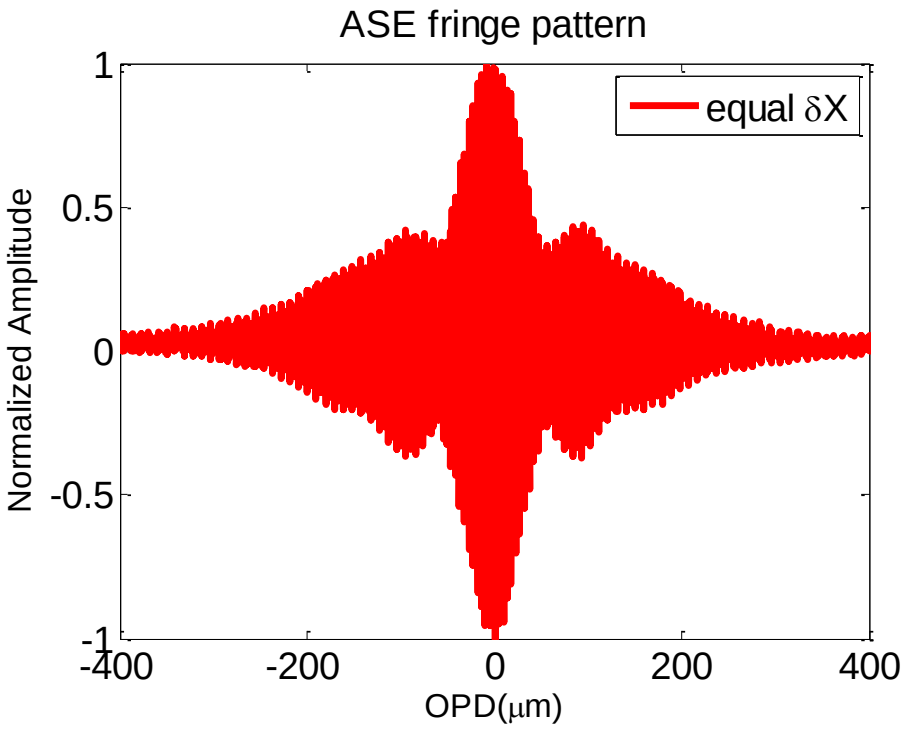

Figure 5.10 Fringe pattern of ASE source after sampling

FFT is also done by Matlab, which is able to convert fringe pattern in time domain to spectrum in frequency domain. Since there is not DUT in the test setup, ideally speaking, the frequency result after FFT is supposed to be the spectrum of ASE source. Therefore, the OLCI measurement system can be verified by comparing its FFT result to the spectrum measured by OSA, which is displayed in Figure 5.11. Both spectra are normalized for the sake of comparison. The blue spectrum is measured by OSA with spectral resolution of 38 pm. The red spectrum is achieved by FFT of ASE fringe pattern with equal OPD increment. It is obvious that FFT result matches OSA spectrum very well, especially at high power region near 1532 nm. Therefore, our OLCI measurement system is successfully verified.

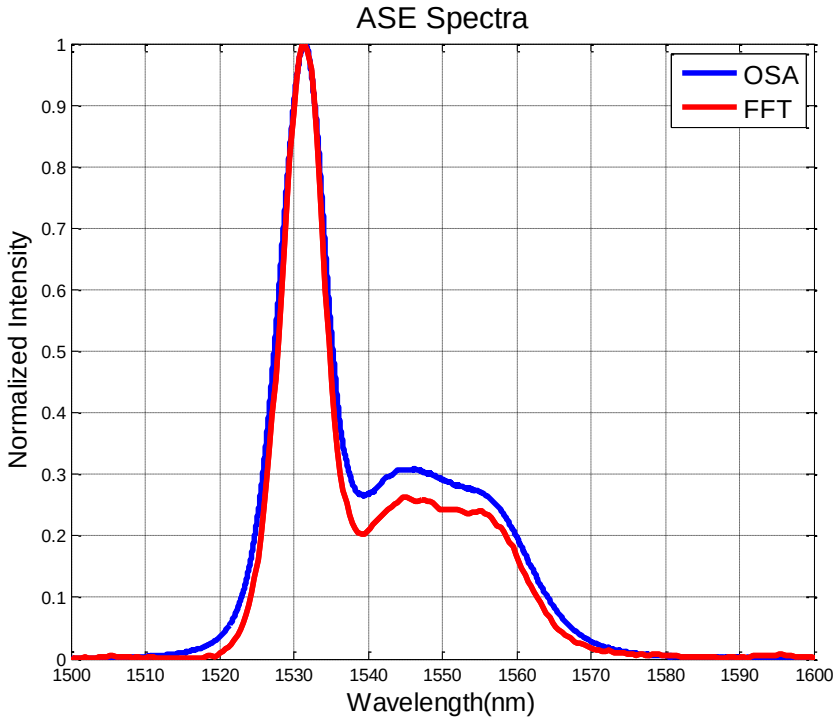

Figure 5.11 ASE spectra from OSA and FFT

The FFT result can be further improved by increasing scan length, which increases N in FFT. In addition, we should decrease the output power of 1310 nm laser to see if it can affect the FFT result. In Figure 5.12, black curve shows the spectrum with double scan length and green curve shows the spectrum with triple scan length. Compared to the original result shown by red curve, the spectrum is optimized by increasing scan length. Since there is almost no difference between black curve and green curve, double scan length can give us the best result, corresponding to scan length of approximate 3 mm. Pink curve displays the result with one-third of the original output of 1310 nm laser. Since there is almost no difference from black curve, the impact of 1310 nm laser can be neglected.

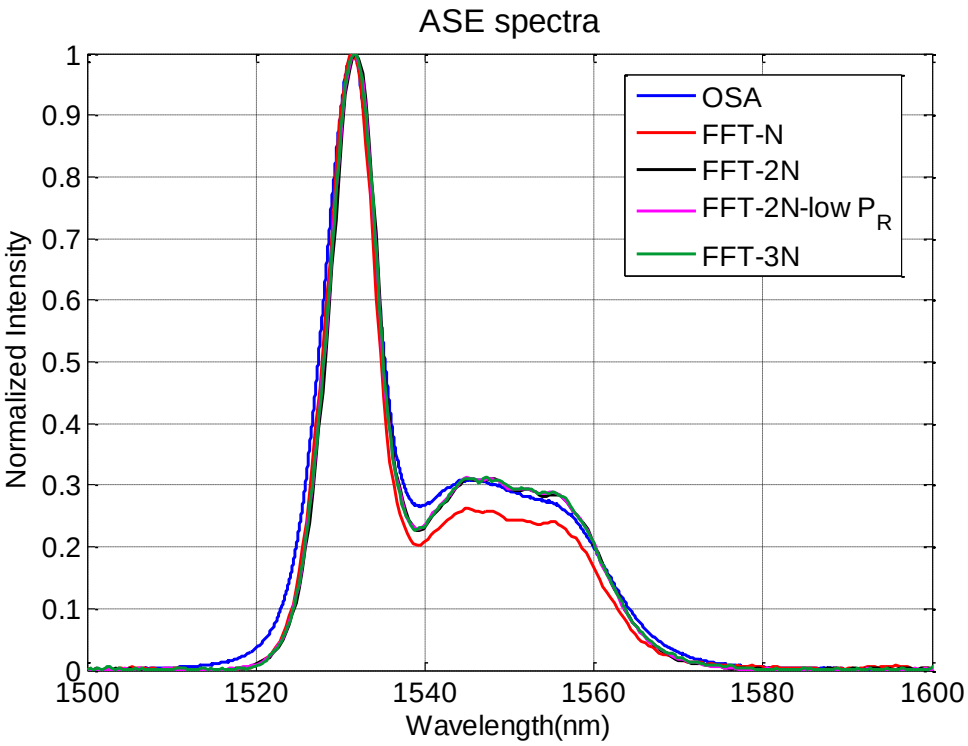

Figure 5.12 Optimized ASE spectra

5.2.2 Ti: $LiNbO_3$ waveguide measurement

After the basic qualification to OLCI measurement system, it is time to characterize its resolution to different modes in waveguide, especially for our As_2S_3-on-$LiNbO_3$ waveguide for FWM down-conversion which has multi-modes at 1.55 μm. In the beginning, Ti: $LiNbO_3$ waveguide, in which light is propagating in fundamental TE and TM modes, is used as the DUT. The fringe patterns are shown in Figure 5.13. Since the effective indices for TE00 and TM00 modes are 2.13 and 2.21, respectively, TE00 mode propagates faster than TM00 mode in the waveguide. Therefore, the first fringe pattern is from TE00 mode and the second fringe pattern is from TM00 mode. Based on the difference of effective indices and the length of the waveguide, the OPD between the

two modes is calculated by equation (5.8), which is 1.44 mm. Since the OPD is much larger than the coherence length of ASE source, OLCI system can recognize fundamental TE mode and TM mode in Ti: $LiNbO_3$ waveguide.

$$OPD = \Delta n \cdot L \tag{5.8}$$

where L is the waveguide length, which is 18 mm.

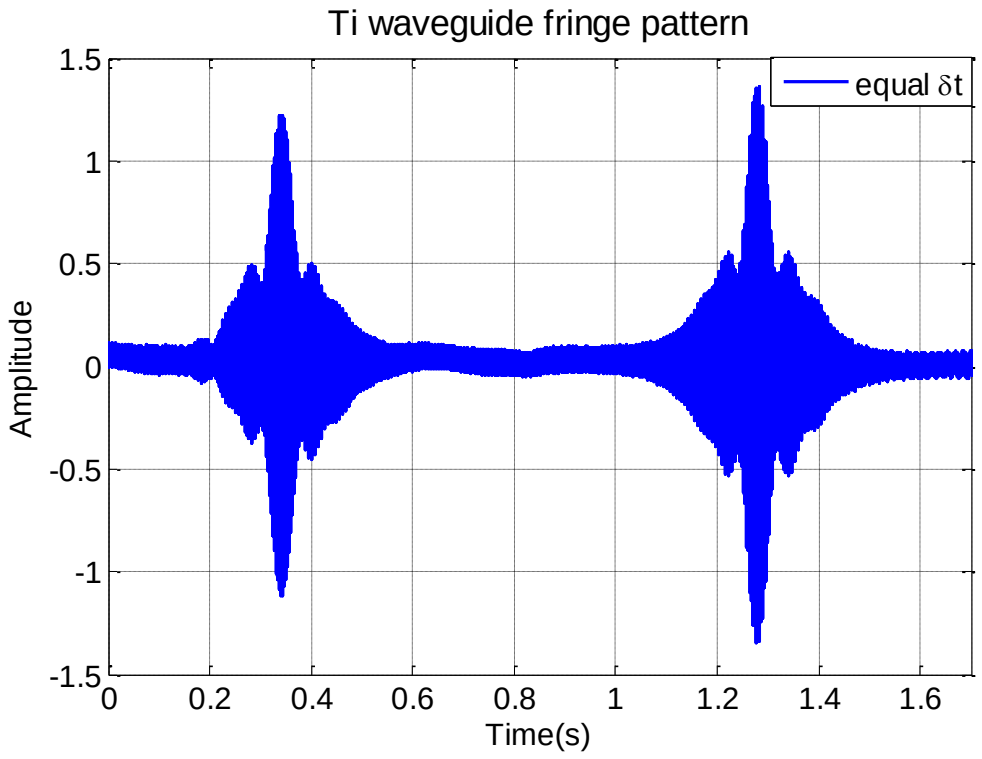

Figure 5.13 Fringe patterns of Ti: $LiNbO_3$ waveguide

Obviously, OLCI measurement system has ability to recognize different modes in Ti: $LiNbO_3$ waveguide. Our next step is to measure As_2S_3-on-$LiNbO_3$ waveguides for FWM down-conversion. From Fimmwave simulation, the effective indice of fundamental TE mode and first higher order TE mode is 2.36 and 2.27, respectively.

Assuming L is still 18 mm, based on equation above, the OPD between the two modes is 1.62 mm, which is also much larger than the coherence length of ASE source. If there is a polarization controller on each arm of the OLCI system, all the light will be propagated by TE mode. The fundamental TE mode and first higher order TE mode of As_2S_3-on-$LiNbO_3$ waveguides can be recognized, which means that two separate fringe patterns will be detected.

5.2.3 Group delay measurement

Since our OLCI measurement method has been verify, the next step is to measure the group delay of a DUT with additional phase. Moreover, it is important to make a comparison to the results measured by commercial detectors. LUNA, a state of the art optical vector analyzer (OVA), has a wavelength range is from 1525 nm to 1605 nm with high spectral resolution of 1.6 pm. The OLCI measurement setup of group delay measurement is shown in Figure 5.14, where a fiber Bragg grating (FBG) is inserted in one arm. Its central wavelength is 1534.4 nm with reflection 3-dB bandwidth of 0.4 nm. Since it is a polarization-independent device, polarization controller is not required in our setup.

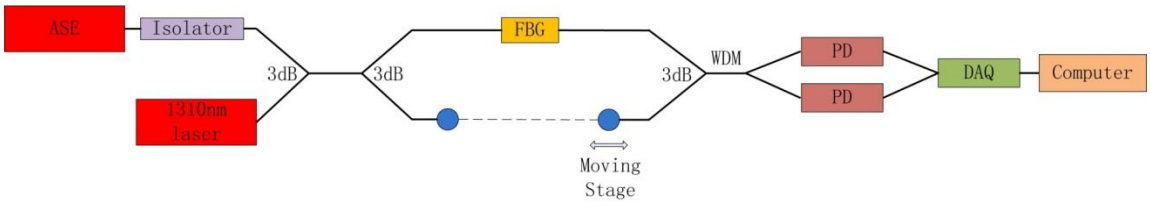

Figure 5.14 OLCI system for group delay measurement

The fiber in FBG arm is re-spliced to make sure that OPD between two arms is within the coherence length of ASE source. The fringe pattern of the FBG is demonstrated in Figure 5.15. After doing FFT to it, the frequency response of the FBG consists of real part and imaginary part, corresponding to the magnitude and the phase responses of FBG.

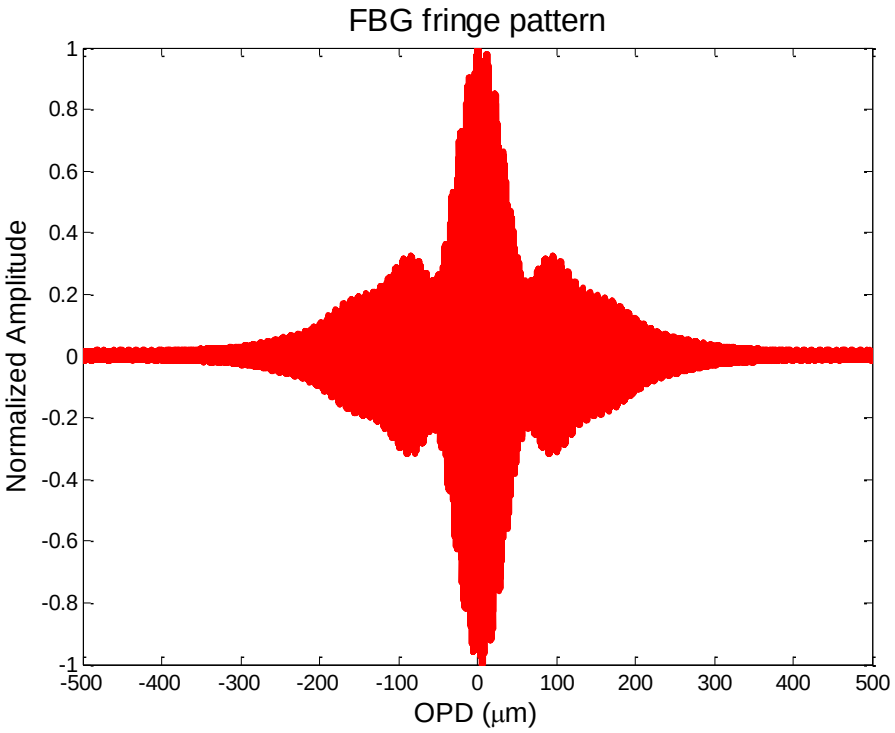

Figure 5.15 Fringe pattern of FBG

The spectrum (Figure 5.16) is the absolute value of both parts and the phase response is the imaginary part. Therefore, the group delay of the FBG is given by equation (5.9) as below

$$GD = -\frac{d\varphi}{d\omega} \tag{5.9}$$

where φ is the phase response of the FBG and ω is the angular frequency.

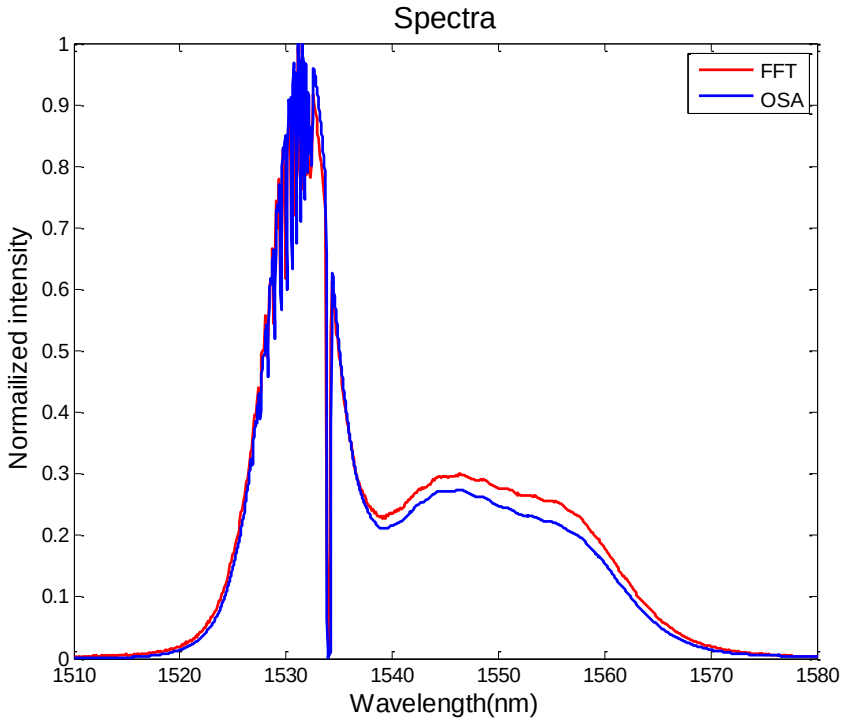

Figure 5.16 FBG spectra comparison

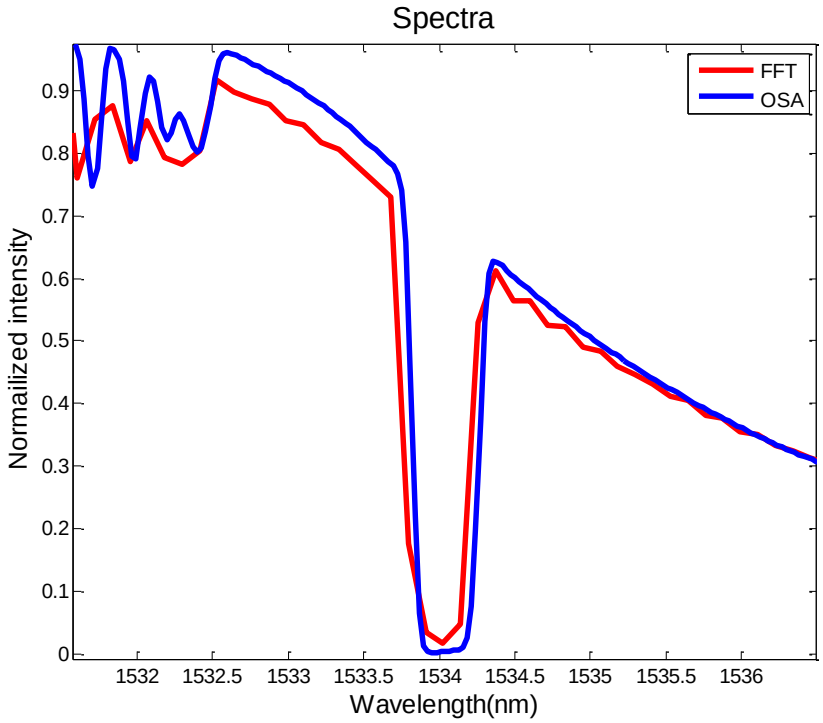

Figure 5.16 Continued

The phase response of FBG is shown in Figure 5.17, in which the slope is changed at 1534 nm, corresponding to its group delay (in Figure 5.18). The blue curve is the group delay of FBG measured by LUNA and the red curve is that measured by OLCI system. Since the OLCI result can match LUNA result very well, its accuracy has been proved. The slight difference results from the difference from spectral resolution. As mention above, the spectral resolution of LUNA is 1.6 pm. However, the spectral resolution of our OLCI system is only 0.21 nm, which is the major limitation of it.

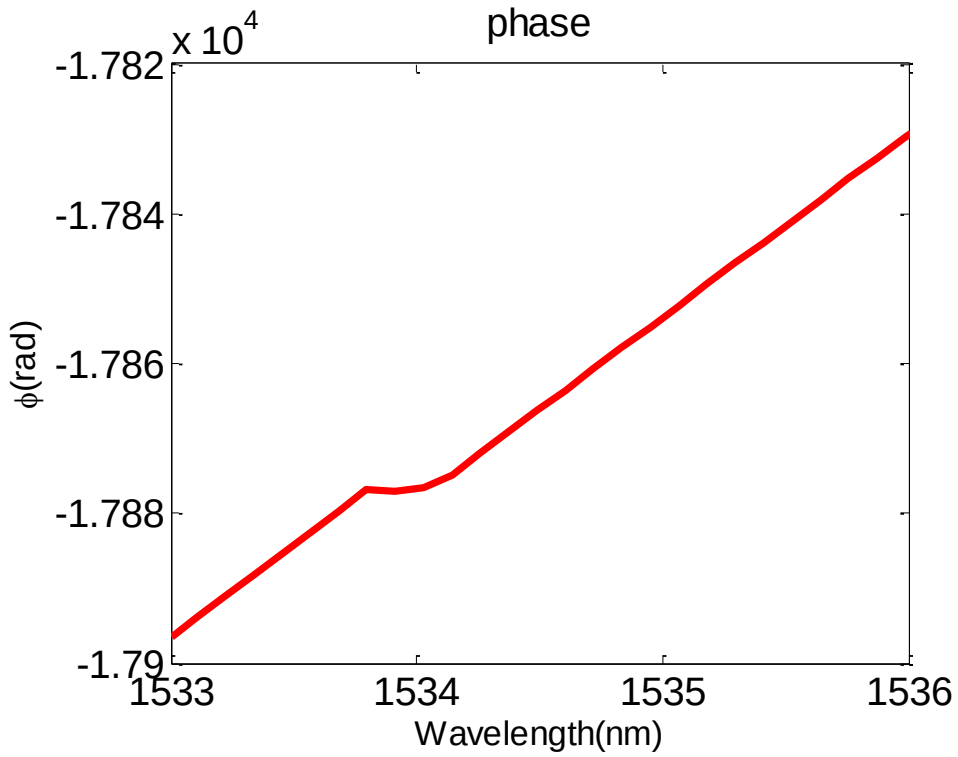

Figure 5.17 Phase response of FBG

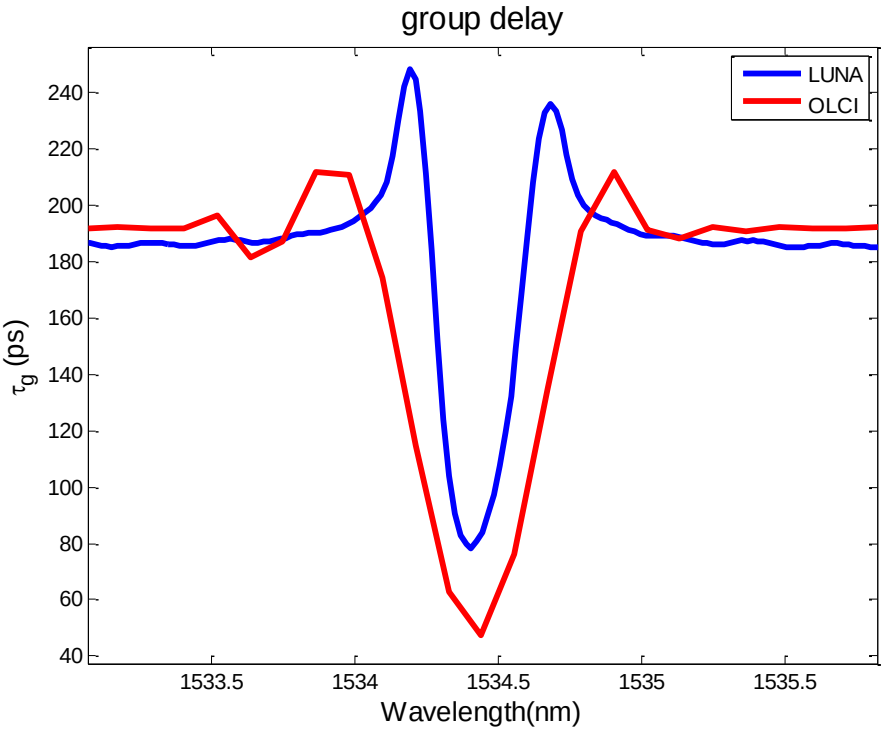

Figure 5.18 Group delay measurement results of FBG

To further improve the OLCI system, it is necessary to increase its spectral resolution. There are several ideas to achieve it. Currently, the largest sampling frequency of DAQ board is 1 MHz. We can increase the sample size of raw data by using an advanced DAQ board with higher sampling frequency. Moreover, a reference laser with smaller wavelength can replace the 1310 nm laser, which can reduce the sampling interval to the raw data. This method requires all the optical components of OLCI setup to propagate the light from the reference laser. The tradeoff should be taken into consideration. In addition, if measure a DUT with long coherence length, we can increase the sampling time in Labview. However, since the maximum travel distance of motorized translation stage is limited, in order to increase sampling time, the speed

should be decreased, which brings another tradeoff. The uncertainty of motion control is large at low speed.

5.2.4 Preparation for OLCI measurement by supercontinuum source

In the future, OLCI measurement system will be utilized to characterize mid-IR optical devices. Supercontinuum (S/C) source, a broadband source with spectrum covers from 450 nm to 2400 nm will replace ASE source. At that time, our measurable range will be largely extended. Since S/C source is a broadband source, it is essential to use a bandpass filter to isolate the wavelength range we are interested, which is around the pump wavelength for FWM designs. The specifications of the filter can be found in www.intorfilters.com/index.php?p=product&id=153. Its center wavelength is 2000 nm with a FWHM of 17 nm. The coherence length calculated by equation (5.3) is 207 μm, which is comparable to that of ASE source. Figure 5.19 shows the OLCI measurement system with S/C source. Broadband light coming from S/C source is filtered by the bandpass filter. After that, ZnSe lens is used to focus the light around 2000 nm and couple it into optical fiber. In addition, there is a polarization controller on each arm to maximize the energy in TE mode. The DUT is As_2S_3-on-$LiNbO_3$ waveguide for FWM down-conversion. Based on previous analysis, although there are multiple TE modes propagating in the waveguide, OLCI measurement system is able to separate fundamental mode and measure it.

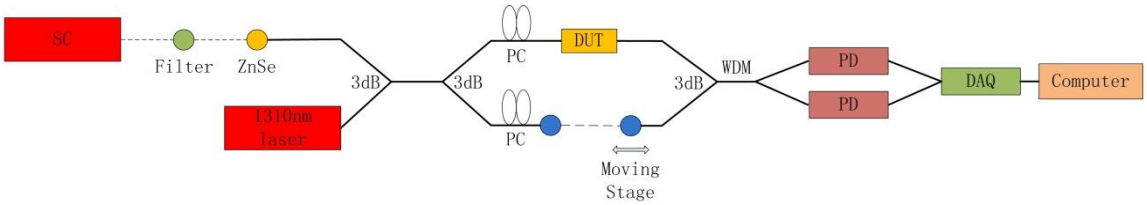

Figure 5.19 OLCI system with S/C source for mid-IR

CHAPTER VI

CONCLUSION

FWM down-conversion design by As_2S_3-on-$LiNbO_3$ waveguides is demonstrated. When phase-matching is satisfied, the parametric conversion efficiency is -8 dB, which is 20 dB higher than the results of silicon waveguides in [29]. Moreover, we illustrate the eSNR improvement by indirect detection to mid-IR signals using FWM up-conversion in As_2S_3-on-$LiNbO_3$ waveguides, which converts mi-IR signals to near-IR wavelengths and then we are able to using state-of-the-art near-IR detectors for detection. Our calculation shows that the eSNR enhancement by phase-matched As_2S_3-on-$LiNbO_3$ waveguides is 17 dB larger the result in silicon waveguides in [30].

OLCI measurement system is built for characterization of optical devices. If the OPD of two arms is within the coherence length of ASE source, a fringe pattern can be achieved. After sampling it by the reference laser, the magnitude and the phase of the DUT is acquired by FFT which converts the result from time domain to frequency domain. The group delay of the DUT is extracted from its frequency response. This OLCI measurement system has the ability to match the existing OSA very well. In the future, it will be transferred to mid-IR by replacing ASE source by S/C source.

REFERENCES

[1] International Technology Roadmap for Semiconductors 2013 Edition Executive Summary, ITRS, http://www.itrs.net, accessed in Apr. 2014.

[2] National Research Council. Implications of Emerging Micro and Nanotechnology. Washington, DC: The National Academies Press, 2002.

[3] Advanced Packaging : 3DIC & 2.5D TSV Interconnect for Advanced Packaging 2014 Business Update, Yole Développement Headquarter, http://www.i-micronews.com/reports/3DIC-2-5D-TSV-Interconnect-Packaging-2014-Business-Update/8/450/, Aug. 2014

[4] F. Tittel, D. Richter, and A. Fried, Mid-Infrared Laser Applications in Spectroscopy, in Solid-State Mid-Infrared Laser Sources, pp. 458-529, 2003.

[5] MIRTHE. Available: www.mirthecenter.org, accessed in Apr, 2014.

[6] H. Nishihara, M. Haruna, and T. Suhara, Eds., Optical Integrated Circuits, McGraw-Hill Optical and Electro-optical Engineering Series. New York: McGraw-Hill Book Company, 1987, p. 374.

[7] A. Zakery and S. R. Elliott, Optical properties and applications of chalcogenide glasses: A review, J. Non-Cryst. Solids., vol. 330, pp. 1-12, 2003.

[8] Solid State division, Hamamatsu Photonics K.K, Characteristics and Use of Infrared Detectors, 2004.

[9] Per Kylemark, Per Olof Hedekvist, Henrik Sunnerud, Magnus Karlsson, and Peter A. Andrekson, "Noise Characteristics of Fiber Optical Parametric Amplifiers," J. Lightwave Technol. 22, 409, 2004.

[10] Wikipedia, Classical electromagnetism, in Wikipedia. Available: http://en.wikipedia.org/wiki/Classical_electrodynamics, accessed in Nov, 2013.

[11] W. S. Rodney, I. H. Malitson, and T. A. King, Refractive index of arsenic trisulfide, J. Opt. Soc. Am., vol. 48, pp. 633-635, 1958.

[12] G. P. Agrawal, Nonlinear Fiber Optics, Chap. 10, 2001.

[13] A. Bohren, M. W. Sigrist, Optical parametric oscillator based difference frequency laser source for photoacoustic trace gas spectroscopy in the 3-µm midIR range, Infrared Phys. Technol. 38, 423–435, 1997.

[14] En-Kuang Tien, Yuewang Huang, Shiming Gao, Qi Song, Feng Qian, Salih K.Kalyoncu, and Ozdal Boyraz, Discrete parametric band conversion in silicon for mid-infrared applications, Optics Express, Vol. 18, Issue 21, pp. 21981-21989, 2010.

[15] Huang, Y. and Tien, E. K. and Gao, S. and Kalyoncu, S. K. and Song, Q. and Qian, F. and Adas, E. and Yildirim, D. and Boyraz, O. , Electrical signal-to-noise ratio improvement in indirect detection of mid-IR signals by wavelength conversion in silicon-on-sapphire waveguides, Applied Physics Letters, 99, 181122, 2011.

[16] T. Vallaitis, S. Bogatscher, L. Alloatti, P. Dumon, R. Baets, M. L. Scimeca, I. Biaggio, F. Diederich, C. Koos, W. Freude, and J. Leuthold, Optical properties of highly nonlinear silicon-organic hybrid (SOH) waveguide ge-ometries, Opt. Express 17(20), 17357–17368, 2009.

[17] Xin Xia, Qi Chen, Candice Tsay, Craig B. Arnold, and Christi K. Madsen, Low-loss chalcogenide waveguides on lithium niobate for the mid-infrared, Opt. Lett. 35, 3228-3230, 2010.

[18] J. Hansryd, P. A. Andrekson, M. Westlund, L. Jie, and P. O. Hedekvist, Fiber-based optical parametric amplifiers and their applications, IEEE J. Sel. Top. Quant. Electron. 8(3), 506–520, 2002.

[19] P. A. Young, Optical properties of vitreous arsenic trisulphide, Journal of Physics C: Solid State Physics, 93, 1971.

[20] M. R. Lamont, B. Luther-Davies, D-Y Choi, S. Madden, X. Gai, and B. J. Eggleton, Net-gain from a parametric amplifier on a chalcogenide optical chip, Opt. Express 16, 20374-20381, 2008.

[21] W.C. Tan, Q. Chen, J.H. Kim, C. Madsen, A Hybrid As2S3 Mach-Zehnder Interferometer Prepared by Mag-netron Sputtering and its Photodarkening Effect, IEEE Journal of Quantum Electronics 48, 0018-9197, 2011.

[22] D. Dimitropoulos, V. Raghunathan, R. Claps, and B. Jalali, Phase-matching and nonlinear optical processes in silicon waveguides, Opt. Express 12(1), 149–160, 2004.

[23] M. Asobe, and K. i. Suzuki, Nonlinear refractive index measurement in chalcogenic-glass fibers by self-phase modulation, Applied Physics Letters 60, 1153, 1992.

[24] Y. Zhou, X. Xia, W. T. Snider, J. Kim, Q. Chen, W. C. Tan, and C. K. Madsen, Two-stage taper enhanced ultrahigh As2S3 ring resonator on $LiNbO_3$, IEEE Photon. Technol. Lett., vol. 23, no. 17, pp. 1195–1197, 2011.

[25] F. Yaman, Q. Lin, Govind P. Agrawal, and S. Radic, Pump-noise transfer in dual-pump fiber-optic parametric amplifiers: walk-off effects, Opt. Lett. 30, 1048-1050, 2005.

[26] Slaven Moro, Ana Peric, Nikola Alic, Bryan Stossel, and Stojan Radic, Phase noise in fiber-optic parametric amplifiers and converters and its impact on sensing and communication systems, Opt. Express 18, 21449-21460, 2010.

[27] Vigo System, Ozarow Mazowiecki, IR Detectors Catalogue, 2006.

[28] Madsen, C. K. and Zhao, J. H., Multi-Stage ARMA Filters in Optical Filter Design and Analysis: A Signal Processing Approach, John Wiley & Sons, Inc., 2001.

[29] Wikipedia, Maxwell's equations, in Wikipedia. Available: http://en.wikipedia.org/wiki/Maxwell's_equations, accessed in Jan, 2011.

[30] Sugimoto, N., Ultrafast Optical Switches and Wavelength Division Multiplexing (WDM) Amplifiers Based on Bismuth Oxide Glasses. Journal of the American Ceramic Society, 85: 1083–1088, 2002.

APPENDIX A

MATLAB CODE FOR FWM SIMULATION

```
%%% FWM simulation for pairs of signal & idler by Qi Chen

clear all;
format long;

M0=load('As2S3_TE_1.5um_1.685um_Dispersion_1.3um_2.05um_Air_Dec_7.txt');

N=1;                        % number of mode
num=size(M0,2);             % number of lines in M0
iter=length(M0)/N;          % number of rows in M0/number of modes
M1=zeros(iter,num);         % zero matrix

for i=1:iter,
   M1(i,:)=M0(N*i,:);          % N=1, M1=M0 rows on 1,4,7,...
%   M1(i,:)=M0(N*i-2,:);      % N=3, M1=M0 rows on 1,4,7,...
%   M2(i,:)=M0(N*i-1,:);      % N=3, M1=M0 rows on 1,4,7,...
end

wv=M1(:,1);
neff=M1(:,3);
Aeff=M1(:,4);

c=300;                      % um/ps
n2=300e-8;                  %n2=3e-18 m^2/W for As2S3, 12e-18 for As2Se3
lmp=2.05;                   % pump wavelength
lmsv=zeros(iter/2,1);
lmiv=zeros(iter/2,1);
nsTE0=zeros(iter/2,1);
niTE0=zeros(iter/2,1);
AeffsTE0=zeros(iter/2,1);
AeffiTE0=zeros(iter/2,1);
gammasTE0=zeros(iter/2,1);
gammaiTE0=zeros(iter/2,1);

for i=1:iter,
   if wv(i)<lmp,
      lmsv(i-iter/2)=wv(i);
      nsTE0(i-iter/2)=neff(i);
      AeffsTE0(i-iter/2)=Aeff(i);
      gammasTE0(i-iter/2)=2*pi*n2/(lmp.*Aeff(i));
```

```
    else
        lmiv(i)=wv(i);
        niTE0(i)=neff(i);
        AeffiTE0(i)=neff(i);
        gammaiTE0(i)=2*pi*n2/(lmp.*Aeff(i));
    end
end

w=1.4, h=1.7 @2.05um 0.18um MgF2
npTE0=2.300947829;
AeffpTE0=1.83998;
gammapTE0=2*pi*n2/(lmp*AeffpTE0);

% w=1.4, h=1.7 @2.05um 0.18um MgF2 1% increase refractive index best
%     npTE0=2.325412354;
%     Aeff=1.802925;
%     gammapTE0=2*pi*n2/(lmp*AeffpTE0);

% w=1.47, h=1.7 @2.05um 0.18um MgF2 5% increase on width
%     npTE0=2.306962974;
%     Aeff=1.965763;

% w=1.456, h=1.7 @2.05um 0.18um MgF2 4% increase on width
%     npTE0=2.305817623;
%     Aeff=1.93786;

% w=1.442, h=1.7 @2.05um 0.18um MgF2 3% increase on width
%     npTE0=2.304644365;
%     Aeff=1.909959;

% w=1.428, h=1.7 @2.05um 0.18um MgF2 2% increase on width
%     npTE0=2.303442285;
%     Aeff=1.883605;

% w=1.414, h=1.7 @2.05um 0.18um MgF2 1% increase on width
%     npTE0=2.302210437;
%     Aeff=1.859992;

% w=1.33, h=1.7 @2.05um 0.18um MgF2 5% decrease on width
%     npTE0=2.294135817;
%     Aeff=1.807195;

% w=1.344, h=1.7 @2.05um 0.18um MgF2 4% decrease on width
%     npTE0=2.29556856;
```

```
%     Aeff=1.804316;

% w=1.358, h=1.7 @2.05um 0.18um MgF2 3% decrease on width
%     npTE0=2.296964941;
%     Aeff=1.806184;

% w=1.372, h=1.7 @2.05um 0.18um MgF2 2% decrease on width
%     npTE0=2.298326177;
%     Aeff=1.812812;

% w=1.386, h=1.7 @2.05um 0.18um MgF2 1% decrease on width
%     npTE0=2.299653434;
%     Aeff=1.824138;

% w=1.54, h=1.7 @2.05um 0.18um MgF2 10% increase on width
%     npTE0=2.312300619;
%     Aeff=2.043087;

% w=1.4, h=1.785 @2.05um 0.18um MgF2 5% increase on As2S3
%     npTE0=2.304512738;
%     Aeff=1.91148;

% w=1.4, h=1.7 @2.05um 0.189um MgF2 5% increase on MgF2
%     npTE0=2.300956884;
%     Aeff=1.840162;

% w=1.5, h=1.685 @2.05um Air best
%     npTE0=2.307998297;
%     AeffpTE0=1.99205;
%     gammapTE0=2*pi*n2/(lmp*AeffpTE0);

% w=1.5, h=1.685 @2.05um Air 1% increase refractive index best
%     npTE0=2.332448275;
%     Aeff=1.963667;

% w=1.42, h=2.7 @2.05um MgF2 0.089um best @4.6 um
% npTE0=2.328336888;
% Aeff=2.688446;

% w=1.42, h=2.6 @2.05um Air test
%       npTE0=2.326669436;
%       Aeff=2.595995;

% w=1.42, h=2.596 @2.05um Air
```

```
%       npTE0=2.32660561;
%       Aeff=2.592794;

gamma=2*pi*n2/(lmp*Aeff);

% 4.6um and 2.05um setup
% Pp=0.9*0.7413 % pump power in W (or more conservatively 100mW)
% Ps=0.36*0.1312 % pump power in W including the loss of MMI

% 1.55um and 2.05um setup
% Pp=0.16*0.8511 % pump power in W including 0.7dB coupling loss
Pp=1.83998;  % 0.1GW/cm2=1.83998W   0.01GW/cm2=0.183998W;
% Pp=0.6457;   % after 1.9dB loss
% Pp=10^(-1.1);   % after 11.6-0.33*1.9=11dB measured coupling loss

Ps=0.001;     % pump power in W

dkpTE0=(2*pi).*(nsTE0./lmsv+niTE0./lmiv-2*npTE0./lmp)
alph0=0.33e-4/(10*log10(exp(1)));  %loss per micron;
L=19e4;  % waveguide length in microns
Leff=(1-exp(-alph0*L))/alph0;
etaTE0=alph0^2./(alph0^2+dkpTE0.^2).*(1+4*exp(-alph0*L)*sin(dkpTE0*L/2).^2/(1-
        exp(-alph0*L))^2); %etaTE0=etaTE0*100 % FWHM efficiency
% Pi=10*log10(exp(-alph0*L).*Ps.*(etaTE0*gammapTE0*Pp*Leff).^2);  % idler
        power in W
g=((gammapTE0*Pp).^2-(dkpTE0/2).^2).^0.5;
Gi=10*log10((gammapTE0*Pp*sinh(g.*L)./g).^2); % equation (7) in Boyraz's OE paper

figure(1);  % Conversion efficiency (dB)
set(gca,'Fontsize',16);
plot(lmsv,Gi,'r','MarkerSize', 2);
hold on;
grid;
legend('0.1 GW/cm^2');
title('\fontsize{16}Parametric conversion efficiency');
xlabel('\fontsize{16}Wavelength(\mum)');
ylabel('\fontsize{16}Gi(dB)');

figure(2);
set(gca,'Fontsize',16);
plot(lmsv,etaTE0,'r','MarkerSize', 2);
hold on;
grid;
legend('\eta^2');
```

```
title('\fontsize{16}FWM phase-matching efficiency');
xlabel('\fontsize{16}Wavelength(\mum)');
ylabel('\eta^2');

figure(3);
set(gca,'Fontsize',16);
plot(lmiv, dkpTE0,'b','MarkerSize', 2);
hold on;
grid;
legend('\delta\kappa');
title('\fontsize{16}Phase mismatch');
xlabel('\fontsize{16}Wavelength(\mum)');
ylabel('\fontsize{16}Phase mismatch(/\mum)');

figure(4);
set(gca,'Fontsize',16);
plot(lmiv, Pi,'g','MarkerSize', 2);
grid;
hold on;
title('\fontsize{16}Output idler power');
xlabel('\fontsize{16}Wavelength(\mum)');
ylabel('\fontsize{16}Output idler power(mW)');


figure(5);
set(gca,'Fontsize',16);
plot(lmsv, (etaTE0*gamma*Pp*Leff).^2,'g','MarkerSize', 2);
grid;
legend('\D');
title('\fontsize{16}test');
xlabel('\fontsize{16}Wavelength(\mum)');
ylabel('\fontsize{16}Dispersion(ps/nm*km)');
```

APPENDIX B

MATLAB CODE FOR eSNR IMPROVEMENT MODELING

```
%%% Noise Calculations for eSNR improvement by Qi Chen

clear all;
format long;

%%% InGaAs detector

k=1.38*10^-23; % Boltzmann constant
T=300; % room temperature in degree K
q=1.6*10^-19; % electron charge
R=0.95; % responsivity of InGaAs detector, A/W
RL=8*10^6; % load resistance in Ω, 8MΩ
NEP=2*10^-15; % noise equivalent power, SNR=1
Pin=0.1*10^-6; % incident power, 0.1uW
id=80*10^-12; % drak current, 80pA
n2=4*10^-18; % nonlinear refractive index in m^2/W
% Aeff=1.3*10^-12; % Si waveguide effective mode area in m^2, 1.3um^2
Aeff=1.99*10^-12; % As2S3 waveguide(air cladding) effective mode area in m^2,
        1.99um^2
lambda=4.6*10^-6; % wavelength in m, 4.6um
P=0:0.001:5;
Pp=P.*(1*10^13).*Aeff;
% Leff=1*10^-2; % Si waveguide effective length in m, 1cm
Leff=4*10^-2; % As2S3 waveguide effective length in m, 4cm
h=6.626*10^-34; % Planck's constant
c=2.998*10^8; % speed of light in m/s

% Thermal noise
Fn=NEP^2*RL*R^2/(4*k*T); % noise figure
I2_th=4*k*T*Fn/RL*10^24.*Pp./Pp; % pA^2/Hz

% Shot noise
gamma=2*pi*n2/(lambda*Aeff);
dkp=6.636*10^-9; % /um
% dkp=0;
g=((gamma.*Pp).^2-(dkp/2)^2).^0.5;
Gi=(gamma.*Pp./g.*sinh(g*Leff)).^2;
Pi=Pin.*Gi;
I2_sh=2*q*(R.*Pi+id)*10^24; % pA^2/Hz
```

```
% Quantum noise
I2_qt=4*R^2.*Pi*h*c/(2*lambda).*(2.*Gi+1)*10^24;
% Total noise
I2=I2_th+I2_sh+I2_qt;

figure(1);  % InGaAs noise
set(gca,'Fontsize',14);
semilogy(P,I2_th,'g',P,I2_sh,'b',P,I2_qt,'r',P,I2,'k','MarkerSize',2,'Linewidth',3);
hold on;
grid;
% legend('0.1 GW/cm^2');
title('\fontsize{16}InGaAs noise');
xlabel('\fontsize{16}Pump power intensity(GW/cm^2)');
ylabel('\fontsize{16}Noise(pA^2/Hz)');

%%% eSNR improvement;

B=0.1*10^6; % bandwidth=0.1MHz
R_PbSe=3*10^3; % responsivity of PbSe detector, V/W
RL_PbSe=0.3*10^6; % resistance of PbSe detector, 0.3MΩ
R_MCT=3*10^3; % responsivity of MCT detector, V/W
RL_MCT=1*10^3; % resistance of PbSe detector, 1KΩ
I2_PbSe=0.1^2; % PbSe noise, pA^2/Hz
I2_MCT=4.09^2; % MCT noise, pA^2/Hz
eSNR_InGaAs=(Pi.*R*10^12).^2./(I2*B); % incident power=0.1uW
eSNR_PbSe=(Pin*R_PbSe/RL_PbSe*10^12)^2/(I2_PbSe*B);
eSNR_MCT=(Pin*R_MCT/RL_MCT*10^12)^2/(I2_MCT*B);
eSNR_impr_PbSe=10.*log(eSNR_InGaAs./eSNR_PbSe);
eSNR_impr_MCT=10.*log(eSNR_InGaAs./eSNR_MCT);

figure(2);  % eSNR improvement
set(gca,'Fontsize',16);
plot(P,eSNR_impr_PbSe,'g',P,eSNR_impr_MCT,'r','MarkerSize',2,'Linewidth',3);
hold on;
grid;
legend('PbSe','MCT');
title('eSNR improvement ');
xlabel('Pump power intensity(GW/cm^2)');
ylabel('eSNR improvement(dB)');
```

APPENDIX C

MATLAB CODE FOR OLCI

```
clear all
format long

t=load('t.txt');
ASE=load('ASE.txt');
L=sgolayfilt(load('L.txt'),5,31);

N=length(t);

figure(1) % equal delta_t fringe pattern
plot(t,ASE,'b','linewidth',2);
hold on;
grid;
set(gca,'Fontsize',14);
legend('equal \deltat')
title('\fontsize{16}Fringe pattern');
xlabel('\fontsize{14}Time(s)');
ylabel('\fontsize{14}Amplitude');

for i=1:N-2
   if abs(L(i+1))>abs(L(i)) && abs(L(i+1))>abs(L(i+2))
      ASE_X=ASE(i);
      save('t_300k_low_X.txt','i','-ASCII','-append')
      save('ASE_300k_low_X.txt','ASE_X','-ASCII','-append')
   end
end

M=load('t_X.txt');
M0=load('ASE_X.txt');

M0=-1+(M0-min(M0))/(max(M0)-min(M0))*2;
N0=length(M);

% [C,I]=max(M0);
% M=M-M(I);

nfft=2*N0;
v=1.5e3; % v=1.5mm/s
X=2*v*M*0.5e-5;
A=fftshift(fft(M0,nfft)); % FFT, nfft=2N0
```

```
% A=(A-min(A))/(max(A)-min(A)); % normalization
% A=A(1:2*N0/2); % FFT is symmetric
c=2.99792458e8; % m/s
dX=1315.5e-9/2; % laser wv/2
fs=c/dX;
n=0:nfft-1;
f=n*fs/nfft-fs/2;
lambda=c./f*1e9;

phi=unwrap(angle(A));
GD=-diff(phi)./diff(2*pi*f')*10^14;

figure(2) % equal delta_X fringe pattern
plot(M,M0,'r','linewidth',3); % shift OPD=0 to center
hold on;
grid;
set(gca,'Fontsize',16);
legend('equal \deltaX')
title('\fontsize{16}ASE fringe pattern');
xlabel('\fontsize{14}OPD(\mum)');
ylabel('\fontsize{14}Normalized Amplitude');
xlim([-400 400]);

figure(3) % FFT
plot(lambda,abs(A),'g','linewidth',3);
hold on;
grid;
set(gca,'Fontsize',14);
title('\fontsize{16}ASE spectrum from FFT');
xlabel('\fontsize{14}Wavelength(nm)');
ylabel('\fontsize{14}Normalized Intensity');
xlim([1500 1600]);

figure(4) % relative phase
plot(lambda,phi','b','linewidth',3);
hold on;
grid;
set(gca,'Fontsize',14);
title('\fontsize{16}Ti waveguide relative phase');
xlabel('\fontsize{14}Wavelength(nm)');
ylabel('\fontsize{20}\phi');
xlim([1520 1570]);
```

```
figure(5) % group delay
plot(lambda,GD,'r' ,'linewidth',3);
hold on;
grid;
set(gca,'Fontsize',14);
title('\fontsize{16}Ti waveguide group delay');
xlabel('\fontsize{14}Wavelength(nm)');
ylabel('\fontsize{14}Group delay (ps)');
xlim([1525 1570]);

% O=load('ASE_OSA.txt'); % ASE spectrum measured by OSA, res:38pm
% O1=O(:,1);
% O2=O(:,2);
% O2=(O2-min(O2))/(max(O2)-min(O2)); % normalized from 0 to 1

% figure(6) % OSA spectrum
% plot(O1,O2,'r','linewidth',3);
% hold on;
% grid;
% set(gca,'Fontsize',14);
% title('\fontsize{16}ASE spectrum from OSA');
% xlabel('\fontsize{14}wavelength(nm)');
% ylabel('\fontsize{14}Amplitude');
% xlim([1500 1600]);
```